Characterization of Fluorescent Nanodiamonds containing Nitrogen-Vacancy and Silicon-Vacancy Color Centers as Produced by Pulsed Laser Ablation in Liquid Confinement

Candidate: Supervisor:
Alessandro Piccoli   Prof. Antonio Miotello

To my family and friends.

Abstract

Nanodiamonds are a promising platform for quantum technologies due to the combinations of their inherent properties and the properties of the fluorescent color centers hosted in diamond. They can be employed as quantum sensing devices with spatial resolution in the range of the nanometer and capable of withstanding harsh conditions while also being biocompatible, allowing applications with sensitive biological systems; but they also find application in quantum computing and photonics fields. For all these applications the central features are the properties of the photoluminescent color centers employed, the color centers on which this thesis is focused are the Nitrogen-Vacancy (NV) and Silicon-Vacancy (SiV) centers of diamond. Both centers are of high interest due to spin dependent properties of their fluorescent emission which can be accessed at room temperature. The development of quantum technologies based on such fluorescent nanodiamonds is stifled by the the lack of production techniques that can be easily scaled to industrial levels. In fact most of the more prominent techniques found in literature exhibit drawbacks both in terms of control of particle properties and of scalability. This thesis focuses on the synthesis of nanodiamonds by Pulsed Laser Ablation in Liquid, with particular interest in the possibility of producing continuously nanodiamonds containing NV and SiV centers. For the NV center the technique of choice have been Pulsed Laser Ablation in liquid nitrogen focusing on the yield of the process as the technique has already been experimentally validated. For the SiV centers the ablation process was performed in water and the graphite precursor have been substituted for a composite graphite and silicon carbide precursor.

Contents

Introduction

The objective of this thesis is to advance the Pulsed Laser Ablation in Liquid (PLAL) technique for the production of fluorescent nanodiamonds (NDs) featuring distinct photoluminescent color centers, in particular focusing on Nitrogen-Vacancy (NV) and Silicon-Vacancy (SiV) centers. Additionally, post-processing procedures for purifying the ablated material will be developed.

These color centers have promising properties for applications in quantum technology, mainly for quantum sensing and quantum computing applications. The study of efficient synthesis techniques for both color centers is an important part in making them a relevant technological platform.

Various established techniques exist for ND production, including detonation synthesis [1], High-Pressure High-Temperature (HPHT) processes [2], and Chemical Vapor Deposition (CVD) based techniques[3]. All these techniques exhibit problematics ranging from the necessity of post-processing milling steps, to high impurity content and even low industrial scalability.

PLAL emerges as a promising alternative, already employed in the production of various nanoparticles[4].

The technique's main advantages lie in cost-effectiveness, ease of use compared to the more established techniques, and the tunability of the process, as well as easier scalability for industrial scale production.

Nanodiamonds have been a subject of extensive research in various fields due to their exceptional properties. The nanoparticles preserve all the characteristics of the bulk material, displaying extreme hardness, high chemical stability, high thermal and low electrical conductivity, biocompatibility, and resilience in harsh environments[1].

The color centers examined in this study are the NV center and the SiV center. The NV center comprises a substitutional nitrogen atom in a diamond lattice site with a neighboring vacancy, while the SiV center consists of an

interstitial silicon atom surrounded by a divacancy, i.e. a vacancy in both adjacent diamond lattice sites.

In recent years, both centers have garnered significant attention for their optical properties, rendering them suitable for quantum applications such as quantum sensing, quantum information processing, and quantum computing.

The NV center exhibits two configurations: a neutral state (NV^0) [5] and a negatively charged state (NV^-) [6]. The NV^- configuration is the focus of this work. References to NV centers in this context will exclusively pertain to the NV^- configuration unless explicitly stated otherwise.

Key features of the NV center include its bright and stable photoluminescence, a zero phonon line (ZPL) at 637 nm, a phonon sideband extending to approximately 800 nm, high photostability with no bleaching at room temperature, and a low relaxation time of around 10 ns [7, 8]. The NV center's central property lies in the strong dependence of its photoluminescence on the spin state [9]: the ground state of the color center is split by spin-spin interactions into $m_S = 0$ an $m_S = \pm 1$ sublevels and the spin state is conserved after optical excitation, the $m_s = 0$ states decay rapidly by emission of a photoluminescence photon, while the states with $m_S = \pm 1$ have a probability of undergoing non-radiative decay by accessing a shelving state. Moreover the initial spin state can be easily manipulated using microwave excitation.

The NV center is influenced by surrounding magnetic moments, the use of extremely pure diamond matrix (with extremely low concentration of ^{13}C or substitutional N atoms) allows to reach coherence times of up to 2 ms [10]. On the other end this can be employed to couple the spin of the electron to nuclear spins of ^{13}C atoms in the lattice to construct quantum registers[11].

The strong coupling of the NV center emission with phonons of the diamond lattice is the main disadvantage for their use in quantum applications. For example, entanglement experiments are performed only taking into consideration ZPL photons, that is only $3 - 5\%$ of the emitted light can be employed leading to extremely low probability for the generation of entangled photons[12].

In the quantum optics field there is very active research in both ways to enhance the ZPL emission of NV centers [13, 14] as well as on different color centers. One of the most promising is the SiV center.

The SiV center is noteworthy for its sharply defined emission spectrum, a characteristic trait of group IV color centers[15]. In a similar manner to the NV center, the SiV center exhibits both a neutral[16] and negatively charged [17] configuration. In this work the focus is on the SiV^- configuration which

displays a ZPL at 738 nm, and, as already stated for the NV center, in this thesis the reference to SiV centers only refers to the negative configuration. The 738 nm ZPL of the SiV center contains approximately 80% of the emitted radiation [18], with minimal phonon coupling. The ZPL can have linewidth lower than 1 nm even at room temperature, while exhibiting single photon emission with rates of $> 10^6$ counts per second, making SiV centers the brightest single-photon source in diamond at room temperature[18].

The optical properties of the SiV center make it an attractive resource for photonics applications requiring single photon emission as well as for quantum computing applications as qubits with the possibility of generating entanglement between distant color centers[19].

Thesis Outline

Chapter 1 will be devoted to an introductory discussion of nanodiamond properties, applications and synthesis technique, based on a selection from the state of the art in literature.

In chapter 2 I will cover the phenomena underlying Pulsed Laser Ablation in Liquid from a theoretical point of view. This will entail a discussion of the interaction between laser and matter, focused on energy deposition mechanisms, followed by a description of Phase Explosion, the underlying phenomenon causing ablation in the experimental conditions of this work. Lastly this will be integrated with a description of the effect of liquid confinement on the process and a discussion of the diamond formation mechanism during ablation.

The following chapter 3 will focus on a description of color centers of diamond, focused on the Nitrogen-Vacancy (NV) and Silicon-Vacancy (SiV) centers. This will consist in a description of the properties of the single color centers from a configurational, optical and electronical point of view, giving special attention to the Hamiltonian terms that describe inherent physical properties of the nanodiamonds and interactions with external fields, which are the basis for their quantum sensing applications.

Chapter 4 and 5 will instead focus on the experimental work performed for the synthesis and characterisation of nanodiamonds containing NV and SiV centers respectively. In both chapters I will cover in detail the synthesis and purification procedure followed by an assessment of the quality of the nanomaterials produced.

Chapter 6 will briefly describe some of the ongoing work for the refinement

of the PLAL technique employed in the previous two experimental chapters, together with a novel approach derived from recent research. The results of this work will then be summarised in the conclusion of this thesis.

Bibliography

[1] Vadym Mochalin, Olga Shenderova, Dean Ho, and Yury Gogotsi. The properties and applications of nanodiamonds. *Nano-enabled medical applications*, pages 313–350, 2020.

[2] Jean-Paul Boudou, Patrick A Curmi, Fedor Jelezko, Joerg Wrachtrup, Pascal Aubert, Mohamed Sennour, Gopalakrischnan Balasubramanian, Rolf Reuter, Alain Thorel, and Eric Gaffet. High yield fabrication of fluorescent nanodiamonds. *Nanotechnology*, 20(23):235602, 2009.

[3] Elke Neu, Carsten Arend, E Gross, F Guldner, Christian Hepp, David Steinmetz, Elisabeth Zscherpel, Slimane Ghodbane, Hadwig Sternschulte, Doris Steinmüller-Nethl, et al. Narrowband fluorescent nanodiamonds produced from chemical vapor deposition films. *Applied Physics Letters*, 98(24), 2011.

[4] Haibo Zeng, Xi-Wen Du, Subhash C Singh, Sergei A Kulinich, Shikuan Yang, Jianping He, and Weiping Cai. Nanomaterials via laser ablation/irradiation in liquid: a review. *Advanced Functional Materials*, 22(7):1333–1353, 2012.

[5] Adam Gali. Theory of the neutral nitrogen-vacancy center in diamond and its application to the realization of a qubit. *Physical Review B*, 79(23):235210, 2009.

[6] Marcus W Doherty, Neil B Manson, Paul Delaney, and Lloyd CL Hollenberg. The negatively charged nitrogen-vacancy centre in diamond: the electronic solution. *New Journal of Physics*, 13(2):025019, 2011.

[7] Lilian Childress and Ronald Hanson. Diamond nv centers for quantum computing and quantum networks. *MRS bulletin*, 38(2):134–138, 2013.

[8] AT Collins, MF Thomaz, and Maria Isabel B Jorge. Luminescence decay time of the 1.945 ev centre in type ib diamond. *Journal of Physics C: Solid State Physics*, 16(11):2177, 1983.

[9] Marcus W Doherty, Neil B Manson, Paul Delaney, Fedor Jelezko, Jörg Wrachtrup, and Lloyd CL Hollenberg. The nitrogen-vacancy colour centre in diamond. *Physics Reports*, 528(1):1–45, 2013.

[10] Gopalakrishnan Balasubramanian, Philipp Neumann, Daniel Twitchen, Matthew Markham, Roman Kolesov, Norikazu Mizuochi, Junichi Isoya, Jocelyn Achard, Johannes Beck, Julia Tissler, et al. Ultralong spin coherence time in isotopically engineered diamond. *Nature materials*, 8(5):383–387, 2009.

[11] Conor E Bradley, Joe Randall, Mohamed H Abobeih, RC Berrevoets, MJ Degen, Michiel A Bakker, Matthew Markham, DJ Twitchen, and Tim H Taminiau. A ten-qubit solid-state spin register with quantum memory up to one minute. *Physical Review X*, 9(3):031045, 2019.

[12] Emre Togan, Yiwen Chu, Alexei S Trifonov, Liang Jiang, Jeronimo Maze, Lilian Childress, MV Gurudev Dutt, Anders Søndberg Sørensen, Phillip R Hemmer, Alexander S Zibrov, et al. Quantum entanglement between an optical photon and a solid-state spin qubit. *Nature*, 466(7307):730–734, 2010.

[13] Igor Aharonovich, Andrew D Greentree, and Steven Prawer. Diamond photonics. *Nature Photonics*, 5(7):397–405, 2011.

[14] AW Schell, J Wolters, T Schröder, and O Benson. Using defect centres in diamonds to build photonic and quantum optical devices. In *Quantum Information Processing with Diamond*, pages 160–194. Elsevier, 2014.

[15] Gergő Thiering and Adam Gali. Ab initio magneto-optical spectrum of group-iv vacancy color centers in diamond. *Physical Review X*, 8(2):021063, 2018.

[16] BL Green, S Mottishaw, BG Breeze, AM Edmonds, UFS D'Haenens-Johansson, MW Doherty, SD Williams, DJ Twitchen, and ME Newton. Neutral silicon-vacancy center in diamond: Spin polarization and lifetimes. *Physical review letters*, 119(9):096402, 2017.

[17] Lachlan J Rogers, Kay D Jahnke, Marcus W Doherty, Andreas Dietrich, Liam P McGuinness, Christoph Müller, Tokuyuki Teraji, Hitoshi Sumiya, Junichi Isoya, Neil B Manson, et al. Electronic structure of the negatively charged silicon-vacancy center in diamond. *Physical Review B*, 89(23):235101, 2014.

[18] Elke Neu, David Steinmetz, Janine Riedrich-Möller, Stefan Gsell, Martin Fischer, Matthias Schreck, and Christoph Becher. Single photon

emission from silicon-vacancy colour centres in chemical vapour deposition nano-diamonds on iridium. *New Journal of Physics*, 13(2):025012, 2011.

[19] Alp Sipahigil, Kay D Jahnke, Lachlan J Rogers, Tokuyuki Teraji, Junichi Isoya, Alexander S Zibrov, Fedor Jelezko, and Mikhail D Lukin. Indistinguishable photons from separated silicon-vacancy centers in diamond. *Physical review letters*, 113(11):113602, 2014.

Chapter 1

Nanodiamond properties and synthesis techniques

Nanodiamonds can be found in nature in conditions of extreme physical processes such as meteoric impacts [1, 2] and as leftovers of stellar formation in asteroids themselves [3, 4]. Synthetic nanodiamonds were first produced during the 20th century by means of detonation of explosives with high carbon concentration [5–7] a technique still in use today and very efficient in terms of amount of powder produced[8–10]. Later, as technology progressed, new avenues of production were identified, mainly static High-Pressure High-Temperature (HPHT) processes[11, 12], Chemical Vapor Deposition techniques[13, 14] and Laser assisted techniques[15–18]. In this chapter I will cover the properties of nanodiamonds and their applications in different field of research and industry.

1.1   Properties of bulk diamond

Diamond is widely known for being the hardest material, it is a crystalline form of Carbon in which C atoms are sp_3 hybridized forming a tetrahedral structure of strong covalent bonds ($711\,\mathrm{kJ/mol}$) with four nearest neighbor atoms at a distance of ($1.53\,\text{Å}$). This structure gives rise to the impressive properties of bulk diamond such as the very high density of the material ($3,145 g/cm^3$) and its mechanical properties (hardest material on both Vickers and Mohs scales, high resistance to compression) [19–21].

The very strong covalent C-C bond gives diamond high chemical stability,

the lattice starts to decompose by oxidation only at temperatures higher than $430°C$ due to metal impurities[22], pure nanodiamonds resist oxidation at temperatures of $575°C$ [23].

Chemical stability is also attested by resistance to acid treatments usually employed to remove impurities from nanodiamonds powders which employ concentrated strong acids (H2SO4, HNO3) at temperatures higher than 150°C [24].

Undoped diamonds have extremely high resistivity $(10^{11} - 10^{18}\Omega/m)$, but have the highest known heat conductivity at room temperature (3300 W/(m K)) thanks to their high phonon mobility[20]. Diamond is a wide bandgap material (5,5 eV)[25] and has also high refractive index in the visible range: from n=2,409 in the red region of the spectrum to n=2.465 for violet[26, 27].
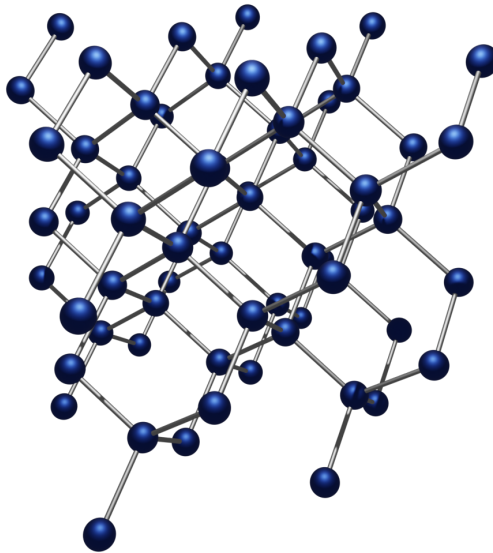
Figure 1.1: Schematic representation of the crystalline structure of diamond

1.2 Properties of nanodiamonds

Nanodiamonds inherit all the properties of bulk diamond, but also show some novel properties intrinsically related to their size. Nanodiamonds are one of the most stable carbon forms in ambient conditions[28].

Surface atoms, which in nanoparticles comprise a non-negligible fraction of the total number of atoms, are characterized by the lack of one of the covalent bonds that form the tetrahedral structure. When compared with other nanocarbons (fullerenes, carbon nanotubes, graphene) nanodiamonds possess a variety of functional groups (fig:1.2) which can be found on their surface, giving them a wide application range[29, 30].
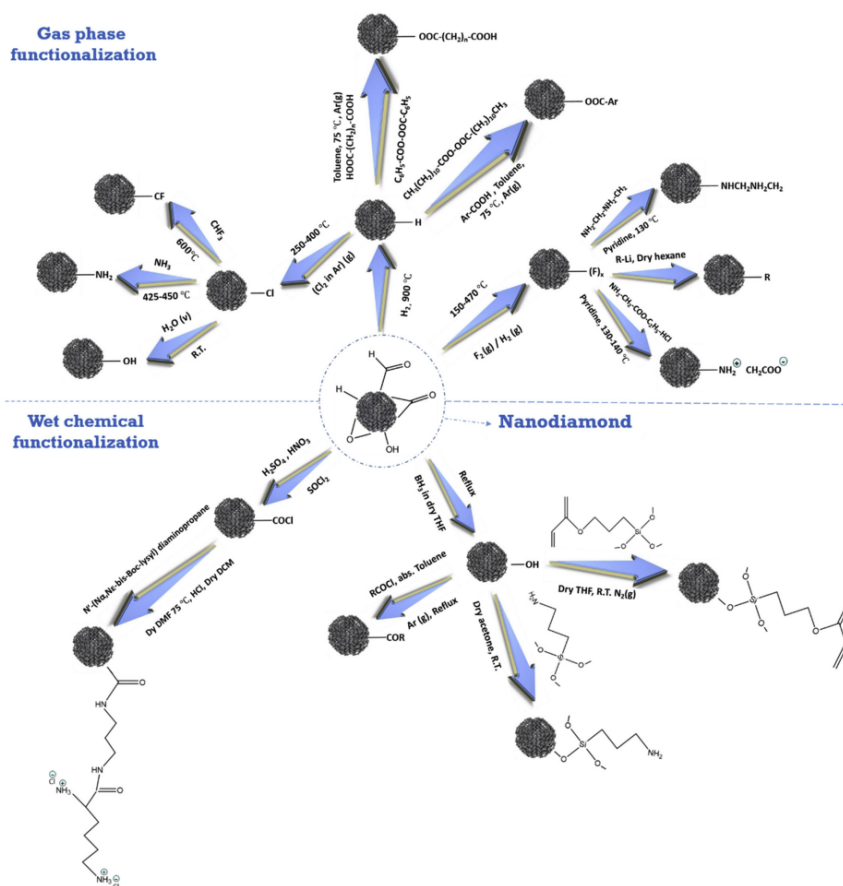
Figure 1.2: A representation of possible surface functionalization of nanodiamonds, reproduced from [30]

NDs are also characterized by good biocompatibility: it has been shown in literature [31, 32] that the presence of nanodiamonds does not influence cell metabolism, growth, differentiation and proliferation.

Another important characteristic of diamond is that it can host various

color centers in the form of impurities of different elements[33–36]:

- Nitrogen
- Boron
- Phosphorous
- Hydrogen
- Nickel

- Cobalt
- Silicon
- Germanium
- Sulphur
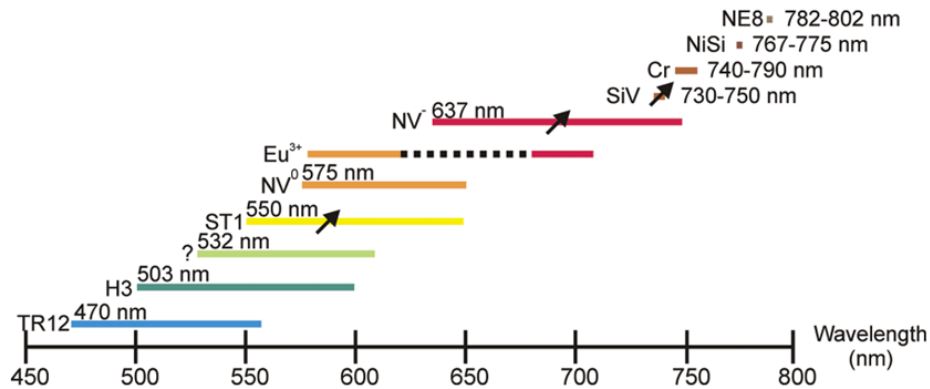
Figure 1.3: Some color centers observed in nanodiamonds, the length of the lines approximately represents the spectral width of the emission spectrum given by phonon sidebands, the value in nm corresponds instead to the zero-phonon line (ZPL) of each center. For the centers emitting in the near infrared region the values in nm show the width of the ZPL of the center. The black arrows indicate centers for which it is possible to manipulate spin values of single color centers. Reproduced from [37].

Nitrogen and Boron color centers are the two most common naturally occurring impurities in bulk- and nano-diamond[33].

Color centers from a single impurity come in different varieties, for example Nitrogen defects can form at least 5 color centers categories (A-,B-,C-,N2,N3) depending on the way the nitrogen atom interacts with the diamond lattice, which all present photoluminescence in different regions of the spectrum[38].

In chapter 3 I will focus more on the description of the color centers studied during my PhD work, the Nitrogen-Vacancy center (NV) and the Silicon-Vacancy (SiV) center.

1.3 Nanodiamond applications

Synthetic diamonds find wide application, from diamond coatings employed for processing of hard materials, to components in high power electrical devices and lens material for high-power high-energy radiation or optics in harsh environment[8].

Nanodiamonds and diamond nanostructures are employed in various fields:

- Energy storage

- Catalysis

- Electroanalysis

- Tribology and lubrication

- Chromatography

- Mass spectroscopy

- Quantum optics

- Quantum sensing

In particular the biocompatibility of nanodiamonds makes them especially well suited for biological and medical applications[39–41].

1.3.1 Nanodiamond composites

Nanodiamonds are used to improve mechanical properties of other materials, mainly polymers [42].

In order to obtain strengthening of the material the components, polymer and reinforcing particles, need to have strong interfacial interaction in order to have optimal load transfer between the components[43, 44], which is achieved either by Van der Waals interaction between the macromolecules and nanoparticles or directly by chemical bonding depending on the application.

The surface of nanodiamonds (accordingly functionalized) enable them to achieve uniform distribution in different matrices and to chemically conjugate with a variety of materials (polymers, biological macromolecules)[45]. It is reported in literature that even a low concentration of NDs leads to a substantial improvement in elastic and strength characteristics of different materials [46, 47].

Moreover NDs can be employed as functional additives that allow for immobilization of particular molecules and as catalysts for processes such as curing and vulcanization of rubbers [32, 48].

1.3.2   Photonics

Nanodiamonds containing different color centers can be employed in photonics applications, in particular Silicon, Chromium, Nickel and Europium centers are promising single photon emitters, capable to be coupled with both waveguides and nanowires [37].

1.3.3   Quantum sensing

Sensing applications rely in particular on their optical and electrochemical properties [37, 40], mainly on the fluorescence of NV and SiV centers.

NDs:NV can be used as probes for magnetic fields, electric field or temperature by exploiting its spin dependent photoluminescence for ODMR measurements [49, 50]. Spin state control via microwaves allows for super resolution microscopy and atomic-scale spin imaging [51, 52]

NDs:SiV can be used as fluorescent tags for biological processes, with resolution comparable to traditional dyes (the size of the smaller nanodiamonds containing SiV center is around 2-5 nm in diameter which is comparable to the size of some dye molecules)[53] and as temperature nanoprobes, with an all optical setup which minimises sample heating by operating at low power and without the need to employ microwaves [54], which, paired to their IR emission, makes them even more interesting for applications in biological systems than NDs:NV.

More details on the properties of Silicon-Vacancy and Nitrogen-Vacancy color center will be covered in the next chapter.

1.3.4   Energy storage applications

Nanodiamonds have been studied as electrodes for poly-electrolyte cells thanks to their scaling electrical resistivity, high chemical stability and resistance to corrosion [55, 56]. Diamond coated silicon nanowires have also been studied for supercapacitor applications[57].

1.3.5 Tribology and lubrication

Nanodiamonds are known to have excellent self-lubricating properties, for this they find applications as additives in lubricating oils and in anti-wear coatings, or in polymers to improve tribological properties. In addition the high thermal conductivity of NDs makes them useful for the dissipation of heat generated in wear conditions [42, 58]

1.4 Nanodiamond Synthesis

1.4.1 Pulsed Laser Ablation in Liquid

Pulsed Laser Ablation in Liquid (PLAL) has been employed for the production of nanoparticles of different materials, particularly metals, but it has also been widely applied to the production of Carbon Nano-Materials (CNMs) [59].

The technique has various merits when compared to other CNM synthesis procedures: it is a facile and effective technique that is relatively simple from a preparation and chemistry standpoint, it entails little to no byproduct formation and generally requires no catalysts. This simplicity makes PLAL operatively safe (with the correct use of the laser) while being a very versatile technique in which slight changes to laser parameters (wavelength, repetition rate, fluence) leads to the formation of a wide range of CNMs[59, 60].
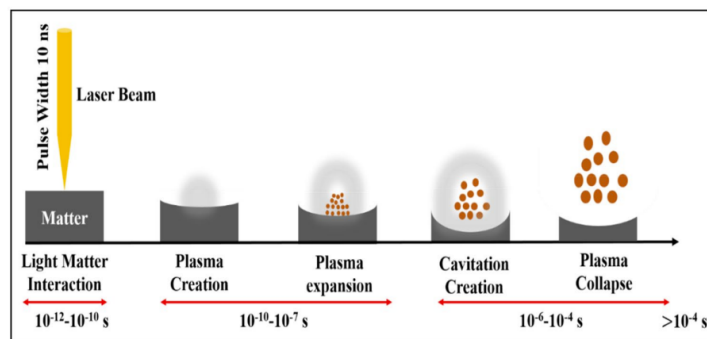
Figure 1.4: Schematics of the ablation caused by nanosecond laser pulses, reproduced from [59], the nanodroplets expelled by phase explosion interact with the plasma plume and the confining medium.

PLAL allows to obtain very pure nanomaterials with very active surfaces without requiring extreme conditions, in fact it can be employed in ambient conditions, while the laser deposits its energy on a very small portion of the target. This, combined by the confining effect of the surrounding liquid, leads to the formation of a region with diameter of the order of the mm [61] where the high energy processes necessary to produce NDs can take place[16, 17, 60].

The usual requirements are just a laser, a carbon source (which in the course of this thesis will be referred to as either precursor or target) and a suitable solvent. In our specific case we used a KrF excimer laser with pulse duration of 20 ns and fluences of the order of tens of J/cm^2.

Some drawbacks of the technique are the low yield ($\sim 5\%$) [62, 63] and the low colloidal stability of the particles, which tend to form conglomerates able to withstand ultrasonic deagglomeration [59].

More detail on PLAL and the underlying processes are discussed in chapter 2.

1.4.2   Detonation Synthesis

Detonation nanodiamonds were first synthesized in 1963 during disintegration of explosives with negative oxygen balance inside sealed vessels. The usual mixture is composed of 60% TNT ($C_6H_2(NO_2)CH_3$) and 40% hexogen ($C_3H_6N_6O_6$). The carbon which will form the nanodiamonds can come either from the explosives themselves or from graphitic precursors put inside the detonation chamber[8, 34].

The detonation chamber requires to be cooled, the usual mediums employed can be inert gasses (nitrogen, argon, CO2) or water (in the form of ice), therefore the two techniques are called dry synthesis and wet synthesis respectively. The cooling medium strongly influences the yield of nanoparticles[64].

In fig:1.5 the process leading to ND formation is schematized: The carbon in the explosive and graphitic precursors dissociates then the temperature and pressure inside the vessel increase to around $3500 - 4000K$ and $20 - 30GPa$, ideal for nanodiamond formation, and lastly the particles settle as temperature and pressure return to ambient values [65, 66]. The resulting nanodiamonds are very fine, with an average size around 5 nm[67], clustered in larger particles as can be seen on the right panel of fig:1.5.

Two main drawbacks of the technique are (i) the low purity of the powder and (ii) the aggregation of the particles.

(a)   (b)
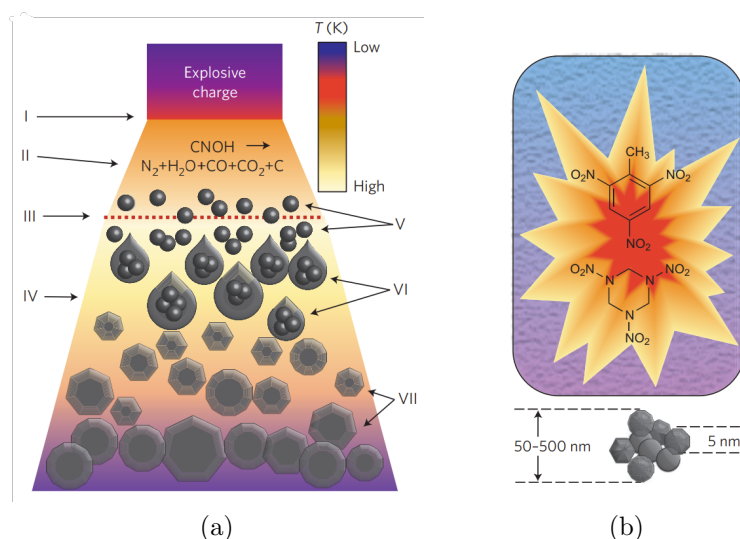
Figure 1.5: Schematization of the process which leads to the formation of NDs: The detonation (I) brings to chemical dissociation of the carbon precursor (II). The dashed line (III) represents the region where pressure required to form diamond phase is reached. The detonation products expand (IV) and the carbon atoms condense and crystallize (V) to form nanoclusters (VI). Finally NDs crystallize starting from carbon nanoclusters, grow and agglomerate (VII). Reproduced from [8]

The process yields powders containing diamond, non-diamond carbon phases and metal impurities from the chamber walls and the ignition devices for the explosives. All the impurities must be removed and the usual procedure requires the use of harsh chemicals like concentrated acids (HNO3, H2SO4)[24, 34].

The agglomeration of the nanodiamonds in large conglomerates requires a subsequent milling step which can introduce impurities from the milling media.

Detonation nanodiamonds are also considered less suitable for quantum sensing applications because they are usually polycrystalline and ultra-nanocrystalline with crystalline domains only a few nanometers wide, which, due to high internal stresses, are regarded as less suitable to host stable color centers such as NV centers than other kinds of NDs [34, 42].

1.4.3   Chemical Vapor Deposition

Chemical vapor deposition is a technique well suited to the production of thin films and it has been employed to produce diamond films. The process consists in the decomposition of very diluted (2% concentration) carbon containing gasses, usually methane, in an hydrogen-rich atmosphere[68, 69].

Gas-phase reactions allow to extract one hydrogen atom from the hydrocarbon precursor, leading to the formation of methyl radicals. The adsorbed methyl radicals can undergo subsequent hydrogen-abstractions reactions, allowing the carbon in the methyl radical to form the C-C bonds necessary for the formation of the diamond lattice.The materials are deposited on surfaces (usually silicon substrates) which are treated by seeding with micro-diamond crystals in order to obtain higher nucleation for the growth of the film[68].

Controlling the properties of the CVD process (temperature, pressure, concentration of precursor) allows to control the grain size of the film which varies from few nanometers to several microns [69].

In fig:1.6 one can see the scheme for a typical CVD apparatus and a schematization of the film formation process.

(a)   (b)
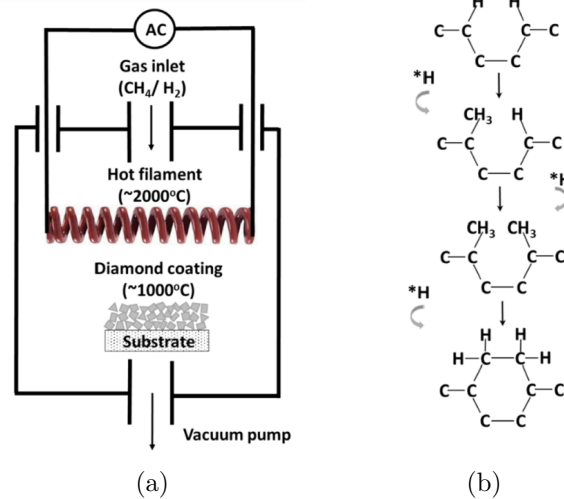
Figure 1.6: A schematic of a hot-filament CVD apparatus (left). On the right a schematic of the process which leads to the growth of the film layer by layer. Reproduced from [70]

Typical drawbacks of the technique are the necessity to perform several

milling steps on the macroscopic film in order to reach dimensions in the order of the tens of nanometers, and the necessity to perform enrichment steps (generally by ion implantation) in order to have efficient formation of fluorescent color centers[8, 71].

1.4.4 High-Pressure High-Temperature synthesis
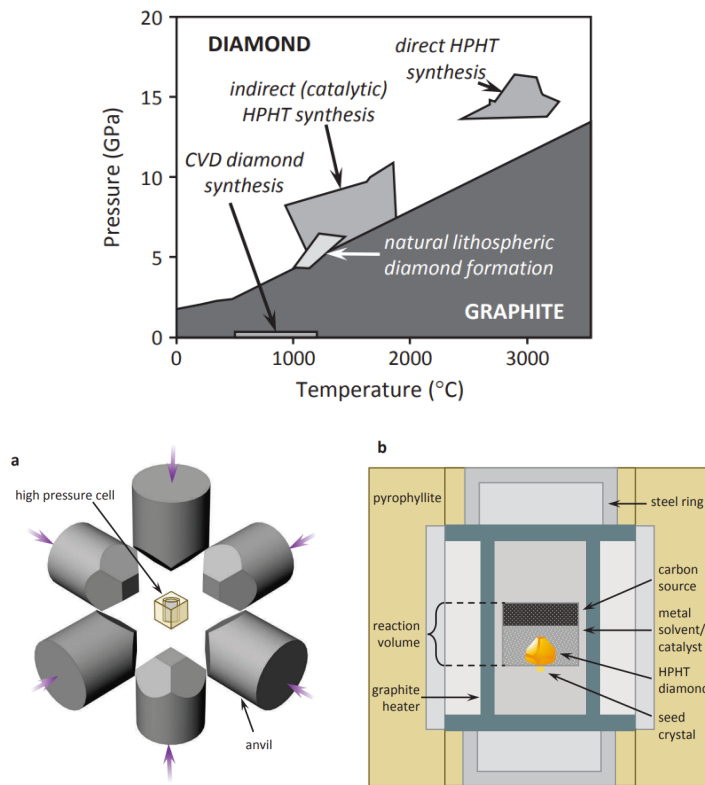
Figure 1.7: Top panel: phase diagram of carbon in the HPHT range, reproduced from [72]. Bottom panel: Standard cubic press pressure transmitting anvil arrangement (a) and detail of the high pressure cell at the center of the apparatus(b), the carbon precursor, kept at a higher temperature than the diamond seeds, dissolves in the molten metal to saturation, recrystallizing in diamond phase upon contact with the seeds. Reproduced from [72]

This technique consists in bringing carbon precursors (usually graphite)

to temperature and pressure conditions similar to those that lead to the formation of diamonds in nature.

In the laboratory, the precursor is brought to temperatures around 2000 °C and pressures of several GPa[11]. In fig:1.7 one can see a schematic of an HPHT apparatus. The procedure allows for the production of micro diamonds, which require additional milling steps in order to obtain nanometric sizes[11].

Bibliography

[1] Ahmed El Goresy, Philippe Gillet, Ming Chen, Friedel Künstler, Günther Graup, and Volker Stähle. In situ discovery of shock-induced graphite-diamond phase transition in gneisses from the ries crater, germany. *American Mineralogist*, 86(5-6):611–621, 2001.

[2] H Jay Melosh. Impact cratering: A geologic process. *New York: Oxford University Press; Oxford: Clarendon Press*, 1989.

[3] Gary R Huss, Alex P Meshik, Julie B Smith, and CM Hohenberg. Presolar diamond, silicon carbide, and graphite in carbonaceous chondrites: Implications for thermal processing in the solar nebula. *Geochimica et Cosmochimica Acta*, 67(24):4823–4848, 2003.

[4] ZR Dai, JP Bradley, DJ Joswiak, DE Brownlee, HGM Hill, and MJ Genge. Possible in situ formation of meteoritic nanodiamonds in the early solar system. *Nature*, 418(6894):157–159, 2002.

[5] Viacheslav Vasilyovich Danilenko. On the history of the discovery of nanodiamond synthesis, 2004.

[6] Paul S DeCarli and John C Jamieson. Formation of diamond by explosive shock. *Science*, 133(3467):1821–1822, 1961.

[7] KV Volkov, VV Danilenko, and VI Elin. Synthesis of diamond from the carbon in the detonation products of explosives. *Combustion, Explosion and shock waves*, 26(3):366–368, 1990.

[8] Vadym Mochalin, Olga Shenderova, Dean Ho, and Yury Gogotsi. The properties and applications of nanodiamonds. *Nano-enabled medical applications*, pages 313–350, 2020.

[9] VF Tatsii, AV Bochko, and GS Oleinik. Structure and properties of dalan detonation diamonds. *Combustion, Explosion, and Shock Waves*, 45:95–103, 2009.

[10] Konosuke Shimazaki, Hiroki Kawaguchi, Hideaki Takashima, Takuya Fabian Segawa, Frederick T-K So, Daiki Terada, Shinobu Onoda, Takeshi Ohshima, Masahiro Shirakawa, and Shigeki Takeuchi. Fabrication of detonation nanodiamonds containing silicon-vacancy

color centers by high temperature annealing. *physica status solidi (a)*, 218(19):2100144, 2021.

[11] Jean-Paul Boudou, Patrick A Curmi, Fedor Jelezko, Joerg Wrachtrup, Pascal Aubert, Mohamed Sennour, Gopalakrischnan Balasubramanian, Rolf Reuter, Alain Thorel, and Eric Gaffet. High yield fabrication of fluorescent nanodiamonds. *Nanotechnology*, 20(23):235602, 2009.

[12] Lin Lai and Amanda S Barnard. Functionalized nanodiamonds for biological and medical applications. *Journal of nanoscience and nanotechnology*, 15(2):989–999, 2015.

[13] MWDJKER Frenklach, W Howard, D Huang, J Yuan, KE Spear, and R Koba. Induced nucleation of diamond powder. *Applied physics letters*, 59(5):546–548, 1991.

[14] C Jany, A Tardieu, A Gicquel, P Bergonzo, and F Foulon. Influence of the growth parameters on the electrical properties of thin polycrystalline cvd diamond films. *Diamond and Related Materials*, 9(3-6):1086–1090, 2000.

[15] Chen-Hon Nee, Ming Chuan Lee, Hun Seng Poh, Seong-Ling Yap, Teck-Yong Tou, and Seong-Shan Yap. Plasma synthesis of nanodiamonds in ethanol. *Composites Part B: Engineering*, 162:162–166, 2019.

[16] Luca Basso, Massimo Cazzanelli, Michele Orlandi, and Antonio Miotello. Nanodiamonds: Synthesis and application in sensing, catalysis, and the possible connection with some processes occurring in space. *Applied Sciences*, 10(12):4094, 2020.

[17] Massimo Cazzanelli, Luca Basso, Claudio Cestari, Nicola Bazzanella, Enrico Moser, Michele Orlandi, Alessandro Piccoli, and Antonio Miotello. Fluorescent nanodiamonds synthesized in one-step by pulsed laser ablation of graphite in liquid-nitrogen. *C*, 7(2):49, 2021.

[18] Guo-Wei Yang, Jin-Bin Wang, and Qui-Xiang Liu. Preparation of nano-crystalline diamonds using pulsed laser induced reactive quenching. *Journal of Physics: Condensed Matter*, 10(35):7923, 1998.

[19] Anke Krueger. The structure and reactivity of nanoscale diamond. *Journal of Materials Chemistry*, 18(13):1485–1492, 2008.

[20] Hugh O Pierson. *Handbook of carbon, graphite, diamonds and fullerenes: processing, properties and applications.* William Andrew, 2012.

[21] Lawrence S Pan and Don R Kania. *Diamond: Electronic Properties and Applications: Electronic Properties and Applications*, volume 294. Springer Science & Business Media, 1994.

[22] Sebastian Osswald, Gleb Yushin, Vadym Mochalin, Sergei O Kucheyev, and Yury Gogotsi. Control of sp2/sp3 carbon ratio and surface chemistry of nanodiamond powders by selective oxidation in air. *Journal of the American Chemical Society*, 128(35):11635–11642, 2006.

[23] Abraham Wolcott, Theanne Schiros, Matthew E Trusheim, Edward H Chen, Dennis Nordlund, Rosa E Diaz, Ophir Gaathon, Dirk Englund, and Jonathan S Owen. Surface structure of aerobically oxidized diamond nanocrystals. *The Journal of Physical Chemistry C*, 118(46):26695–26702, 2014.

[24] Yuto Makino, Tomoaki Mahiko, Ming Liu, Akihiko Tsurui, Taro Yoshikawa, Shinji Nagamachi, Shigeru Tanaka, Kazuyuki Hokamoto, Masaaki Ashida, Masanori Fujiwara, et al. Straightforward synthesis of silicon vacancy (siv) center-containing single-digit nanometer nanodiamonds via detonation process. *Diamond and Related Materials*, 112:108248, 2021.

[25] GS Painter, Donald E Ellis, and AR Lubinsky. Ab initio calculation of the electronic structure and optical properties of diamond using the discrete variational method. *Physical Review B*, 4(10):3610, 1971.

[26] Ioannis Neitzel, Vadym Mochalin, and Yury G Gogotsi. Advances in surface chemistry of nanodiamond and nanodiamond-polymer composites. 2012.

[27] Rich P Mildren et al. Intrinsic optical properties of diamond. *Optical Engineering of Diamond*, 1:1–34, 2013.

[28] P Badziag, WS Verwoerd, WP Ellis, and NR Greiner. Nanometre-sized diamonds are more stable than graphite. *Nature*, 343(6255):244–245, 1990.

[29] E Mironov, A Koretz, and E Petrov. Detonation synthesis ultradispersed diamond structural properties investigation by infrared absorption. *Diamond and related materials*, 11(3-6):872–876, 2002.

[30] Saira Jabeen, Ayesha Kausar, Bakhtiar Muhammad, Sagheer Gul, and Muhammad Farooq. A review on polymeric nanocomposites of nanodiamond, carbon nanotube, and nanobifiller: structure, preparation and properties. *Polymer-Plastics Technology and Engineering*, 54(13):1379–1409, 2015.

[31] Ying Zhu, Jing Li, Wenxin Li, Yu Zhang, Xiafeng Yang, Nan Chen, Yanhong Sun, Yun Zhao, Chunhai Fan, and Qing Huang. The biocompatibility of nanodiamonds and their application in drug delivery systems. *Theranostics*, 2(3):302, 2012.

[32] Qingwei Zhang, Vadym N Mochalin, Ioannis Neitzel, Isabel Y Knoke, Jingjia Han, Christopher A Klug, Jack G Zhou, Peter I Lelkes, and Yury Gogotsi. Fluorescent plla-nanodiamond composites for bone tissue engineering. *Biomaterials*, 32(1):87–94, 2011.

[33] Jean-Charles Arnault. *Nanodiamonds: advanced material analysis, properties and applications*. William Andrew, 2017.

[34] Olga A Shenderova and Dieter M Gruen. *Ultrananocrystalline diamond: synthesis, properties and applications*. William Andrew, 2012.

[35] Stefania Castelletto, Andrew Edmonds, Torsten Gaebel, and James Rabeau. Production of multiple diamond-based single-photon sources. *Ieee Journal of Selected Topics in Quantum Electronics*, 18(6):1792–1798, 2012.

[36] D Gatto Monticone, Paolo Traina, E Moreva, Jacopo Forneris, Paolo Olivero, IP Degiovanni, F Taccetti, L Giuntini, Giorgio Brida, Giampiero Amato, et al. Native nir-emitting single colour centres in cvd diamond. *New Journal of Physics*, 16(5):053005, 2014.

[37] Igor Aharonovich and Elke Neu. Diamond nanophotonics. *Advanced Optical Materials*, 2(10):911–928, 2014.

[38] Hsiao-Chi Lu, Meng-Yeh Lin, Sheng-Lung Chou, Yu-Chain Peng, Jen-Iu Lo, and Bing-Ming Cheng. Identification of nitrogen defects in diamond

with photoluminescence excited in the 160–240 nm region. *Analytical chemistry*, 84(21):9596–9600, 2012.

[39] Chi-Cheng Fu, Hsu-Yang Lee, Kowa Chen, Tsong-Shin Lim, Hsiao-Yun Wu, Po-Keng Lin, Pei-Kuen Wei, Pei-Hsi Tsao, Huan-Cheng Chang, and Wunshain Fann. Characterization and application of single fluorescent nanodiamonds as cellular biomarkers. *Proceedings of the National Academy of Sciences*, 104(3):727–732, 2007.

[40] Giorgio Speranza. Carbon nanomaterials: Synthesis, functionalization and sensing applications. *Nanomaterials*, 11(4):967, 2021.

[41] David M Toyli, Charles F de Las Casas, David J Christle, Viatcheslav V Dobrovitski, and David D Awschalom. Fluorescence thermometry enhanced by the quantum coherence of single spins in diamond. *Proceedings of the National Academy of Sciences*, 110(21):8417–8421, 2013.

[42] Pooria Karami, Samaneh Salkhi Khasraghi, Mohammadjafar Hashemi, Sima Rabiei, and Akbar Shojaei. Polymer/nanodiamond composites-a comprehensive review from synthesis and fabrication to properties and applications. *Advances in colloid and interface science*, 269:122–151, 2019.

[43] Yasir A Haleem, Daobin Liu, Wenxing Chen, Changda Wang, Caihao Hong, Zhen He, Jianwei Liu, Pin Song, Shuhong Yu, and Li Song. Surface functionalization and structure characterizations of nanodiamond and its epoxy based nanocomposites. *Composites Part B: Engineering*, 78:480–487, 2015.

[44] Maryam Alishiri, Akbar Shojaei, and Mohammad Jafar Abdekhodaie. Biodegradable polyurethane acrylate/hema-grafted nanodiamond composites with bone regenerative potential applications: structure, mechanical properties and biocompatibility. *RSC advances*, 6(11):8743–8755, 2016.

[45] Maria Letizia Terranova, Silvia Orlanducci, Marco Rossi, and Emanuela Tamburri. Nanodiamonds for field emission: state of the art. *Nanoscale*, 7(12):5094–5114, 2015.

[46] MR Ayatollahi, E Alishahi, S Doagou-R, and S Shadlou. Tribological and mechanical properties of low content nanodiamond/epoxy nanocomposites. *Composites Part B: Engineering*, 43(8):3425–3430, 2012.

[47] Wei Yu, Huaqing Xie, Yang Li, Lifei Chen, and Qiang Wang. Experimental investigation on the thermal transport properties of ethylene glycol based nanofluids containing low volume concentration diamond nanoparticles. *Colloids and Surfaces A: Physicochemical and Engineering Aspects*, 380(1-3):1–5, 2011.

[48] Kate Fox, Phong A Tran, Desmond WM Lau, Takeshi Ohshima, Andrew D Greentree, and Brant C Gibson. Nanodiamond-polycaprolactone composite: A new material for tissue engineering with sub-dermal imaging capabilities. *Materials Letters*, 185:185–188, 2016.

[49] Florian Dolde, Helmut Fedder, Marcus W Doherty, Tobias Nöbauer, Florian Rempp, Gopalakrishnan Balasubramanian, Thomas Wolf, Friedemann Reinhard, Lloyd CL Hollenberg, Fedor Jelezko, et al. Electric-field sensing using single diamond spins. *Nature Physics*, 7(6):459–463, 2011.

[50] Georg Kucsko, Peter C Maurer, Norman Ying Yao, MICHAEL Kubo, Hyun Jong Noh, Po Kam Lo, Hongkun Park, and Mikhail D Lukin. Nanometre-scale thermometry in a living cell. *Nature*, 500(7460):54–58, 2013.

[51] Ashok Ajoy, Ulf Bissbort, Mikhail D Lukin, Ronald Lee Walsworth, and Paola Cappellaro. Atomic-scale nuclear spin imaging using quantum-assisted sensors in diamond. *Physical Review X*, 5(1):011001, 2015.

[52] Edward H Chen, Ophir Gaathon, Matthew E Trusheim, and Dirk Englund. Wide-field multispectral super-resolution imaging using spin-dependent fluorescence in nanodiamonds. *Nano letters*, 13(5):2073–2077, 2013.

[53] Tobias D Merson, Stefania Castelletto, Igor Aharonovich, Alisa Turbic, Trevor J Kilpatrick, and Ann M Turnley. Nanodiamonds with silicon vacancy defects for nontoxic photostable fluorescent labeling of neural precursor cells. *Optics letters*, 38(20):4170–4173, 2013.

[54] Christian T Nguyen, Ruffin E Evans, Alp Sipahigil, Mihir K Bhaskar, Denis D Sukachev, Viatcheslav N Agafonov, Valery A Davydov, Liudmila F Kulikova, Fedor Jelezko, and Mikhail D Lukin. All-optical nanoscale thermometry with silicon-vacancy centers in diamond. *Applied Physics Letters*, 112(20), 2018.

[55] Min Wei, Li-Guo Sun, Zhuo-Ying Xie, Jin-Fang Zhii, Akira Fujishima, Yasuaki Einaga, De-Gang Fu, Xue-Mei Wang, and Zhong-Ze Gu. Selective determination of dopamine on a boron-doped diamond electrode modified with gold nanoparticle/polyelectrolyte-coated polystyrene colloids. *Advanced Functional Materials*, 18(9):1414–1421, 2008.

[56] Elisabetta Petrucci, Luca Di Palma, Roberto Lavecchia, and Antonio Zuorro. Modeling and optimization of reactive green 19 oxidation on a bdd thin-film electrode. *Journal of the Taiwan Institute of Chemical Engineers*, 51:152–158, 2015.

[57] Fang Gao, Georgia Lewes-Malandrakis, Marco T Wolfer, Wolfgang Müller-Sebert, Pascal Gentile, David Aradilla, Thomas Schubert, and Christoph E Nebel. Diamond-coated silicon wires for supercapacitor applications in ionic liquids. *Diamond and Related Materials*, 51:1–6, 2015.

[58] Pooria Karami and Akbar Shojaei. Improvement of dry sliding tribological properties of polyamide 6 using diamond nanoparticles. *Tribology International*, 115:370–377, 2017.

[59] Gaurav Kumar Yogesh, Shivam Shukla, D Sastikumar, and Pankaj Koinkar. Progress in pulsed laser ablation in liquid (plal) technique for the synthesis of carbon nanomaterials: A review. *Applied Physics A*, 127:1–40, 2021.

[60] Vincenzo Amendola, David Amans, Yoshie Ishikawa, Naoto Koshizaki, Salvatore Scirè, Giuseppe Compagnini, Sven Reichenberger, and Stephan Barcikowski. Room-temperature laser synthesis in liquid of oxide, metal-oxide core-shells, and doped oxide nanoparticles. *Chemistry– A European Journal*, 26(42):9206–9242, 2020.

[61] Kotaro Saito, Kazuhiro Takatani, Tetsuo Sakka, and Yukio H Ogata. Observation of the light emitting region produced by pulsed laser irra-

diation to a solid–liquid interface. *Applied surface science*, 197:56–60, 2002.

[62] L Yang, PW May, L Yin, JA Smith, and KN Rosser. Growth of diamond nanocrystals by pulsed laser ablation of graphite in liquid. *Diamond and related materials*, 16(4-7):725–729, 2007.

[63] Luca Basso, F Gorrini, M Cazzanelli, N Bazzanella, A Bifone, and A Miotello. An all-optical single-step process for production of nanometric-sized fluorescent diamonds. *Nanoscale*, 10(12):5738–5744, 2018.

[64] Valerii Yu Dolmatov. Detonation synthesis ultradispersed diamonds: properties and applications. *Russian Chemical Reviews*, 70(7):607–626, 2001.

[65] AM Staver, NV Gubareva, AI Lyamkin, and EA Petrov. Ultrafine diamond powders made by the use of explosion energy. *Combust., Explos. Shock Waves (Engl. Transl.);(United States)*, 20(6), 1985.

[66] VV Danilenko. Shock-wave sintering of nanodiamonds. *Physics of the Solid State*, 46:711–715, 2004.

[67] AI Lyamkin, EA Petrov, AP Ershov, GV Sakovich, AM Staver, and VM Titov. Production of diamonds from explosives. In *Soviet Physics Doklady*, volume 33, page 705, 1988.

[68] James E Butler and Anirudha V Sumant. The cvd of nanodiamond materials. *Chemical Vapor Deposition*, 14(7-8):145–160, 2008.

[69] Michael Schwander and Knut Partes. A review of diamond synthesis by cvd processes. *Diamond and related materials*, 20(9):1287–1301, 2011.

[70] Chunyan Zhang, Ratnakar D Vispute, Kun Fu, and Chaoying Ni. A review of thermal properties of cvd diamond films. *Journal of Materials Science*, 58(8):3485–3507, 2023.

[71] Eisuke Abe and Kento Sasaki. Tutorial: Magnetic resonance with nitrogen-vacancy centers in diamond—microwave engineering, materials science, and magnetometry. *Journal of Applied Physics*, 123(16), 2018.

[72] Ulrika FS D'Haenens-Johansson, James E Butler, and Andrey N Katrusha. Synthesis of diamonds and their identification. *Reviews in Mineralogy and Geochemistry*, 88(1):689–753, 2022.

Chapter 2

Laser-Matter interaction in Pulsed Laser Ablation

Lasers can be employed to modify and machine materials in a variety of different techniques, from ablation for the production of nanoparticles [1–3], to characterisation and restoration of surfaces of often delicate cultural heritage artifacts [4] to the production of surface features such as Laser Induced Periodic Structures (LISPs)[5, 6] or other nanostructures [7, 8].

In order to understand the processes leading to PLAL one must start by understanding how laser light interacts with a material, in particular the energy deposition mechanism. This interaction strongly depends on the properties of the laser (energy, fluence, pulse duration, wavelength) and the properties of the material, in particular when considering materials of different nature (metals, dielectrics, semiconductors)[9–11].

The relevant materials for this work are graphite and silicon carbide, which are a conductor and semiconductor respectively. I will therefore cover some mechanisms of energy absorption focusing on those categories, avoiding the treatment for large band gap dielectrics.

It is known from literature [8, 11–13] that in the fluence-pulse duration window relative to the experimental conditions of this work the ablation of the material is obtained via Phase Explosion. This is also discussed for the case of confined laser ablation, that is for the case of liquid confinement.

These discussions lead to the description of the conditions realised experimentally which allow for the production of nanodiamonds in our apparatus [3, 14, 15].

2.1 Laser-matter interaction: energy deposition

The interaction between laser and materials depends on both the parameters of the laser itself (wavelength, pulse duration, fluence) and the optical, thermal and mechanical properties of the material[10].

The energy of the laser is deposited by coupling of the laser photons with the electrons in the material, therefore one of the most important material characteristics is the presence of a band gap.
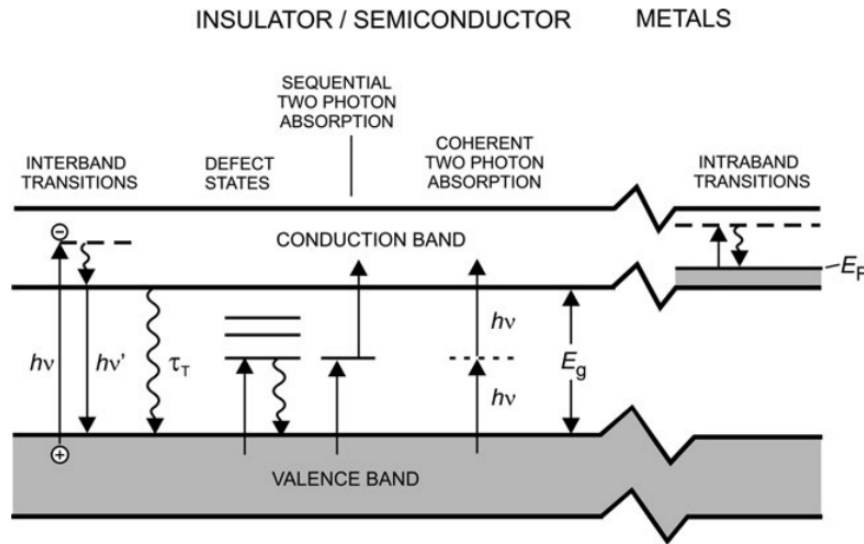
Figure 2.1: Representation of different absorption processes in band gap materials and conductors, reproduced from [9]

Conductive materials are characterised by a Fermi level that lies inside the conduction band, allowing the excitation of electrons to higher energy unoccupied states. This can be described by a two temperature model in which the electron are excited to a new configuration, according to the density of states of the material, and rapidly thermalise to a new equilibrium state (on timescales on the order of tens to hundreds of fs) at a much higher temperature than the lattice[10, 16]. The ions in the lattice, due to the large difference in mass between the them and the electrons, require a longer time to reach thermal equilibrium by electron-phonon collisions, see fig:2.2. The

dependence on the DOS of each material can give rise to different transient effects in the electron phonon non-equilibrium regime[16, 17].

On the other end, electrons in semiconductors can be excited by different phenomena (see fig:2.1). If the laser has photon energy which is higher than the semiconductor band gap the dominant mechanism is single photon absorption[10, 17]. This can be both in terms of excitation of valence band electrons to the conduction band as well as free carrier absorption in the conduction band. The second process increases the absorbance of the material, but does not directly increase the free carrier concentration, although it can promote electron excitation via impact ionisation (electron-electron scattering)[17]. Two-photon excitation remains a relevant process even when the energy of the photon is enough to overcome the band gap in particular for indirect band gap materials.
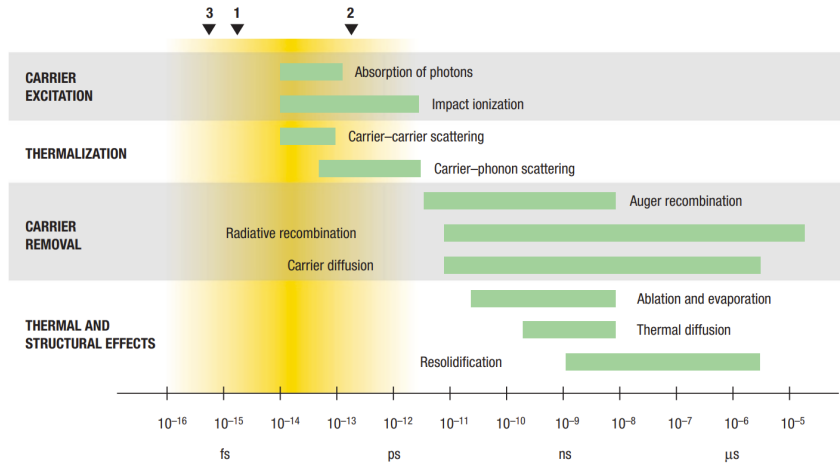
Figure 2.2: Representation of the timescales of different processes related to the absorption of laser light from a material, reproduced from [17]

In this work I focus on graphite and composite graphite-silicon carbide materials.

Graphite is conductive due to the delocalization of the electrons in the crystalline planes of the material, therefore the absorption happens due to intraband transitions in the conduction band.

The other material I work with is a composite of graphite grains interspersed with micro-particles of SiC. SiC is a wide band gap indirect semiconductor ($E_{BG} = 3.26eV$). The laser employed in this work is a KrF excimer

laser with emission at 248 nm, which allows to work with photon energy above the band gap energy, meaning the leading mechanism of absorption is single-photon absorption, with contributions from two-photon absorption and free-carrier excitation, as stated above.

The laser pulse employed in this work has a duration of 20 ns, which is much longer than the timescale of the thermalisation of the lattice due to carrier-phonon scattering. This means that the phenomena observed during the irradiation are of thermal origin [11, 17].

In particular, taking into account the high fluence at the laser spot, the leading ablation mechanism is Phase Explosion, which will be described in the section 2.2.

2.1.1   Two Temperature Model

In the previous section I mentioned the different timescales of the processes happening inside the material when excited by laser pulses. The Two-Temperature Model (TTM) assumes that the absorption-thermalisation timescale is shorter than any other process (heat propagation, material response, pressure change, shockwave formation) happening during excitation and the system can be described by considering the electrons excited by the laser to high temperature and the lattice only indirectly heated by the electrons[18].

In TTM the temperature evolution of the system is described as the evolution of the electron temperature T_e and of the lattice temperature T_l

$$C_e \frac{\partial T_e}{\partial t} = \nabla \cdot (\kappa_e \nabla T_e) - \Gamma (T_e - T_l) + Q(\mathbf{r}, t) \qquad (2.1)$$

$$C_l \frac{\partial T_l}{\partial t} = \nabla \cdot (\kappa_l \nabla T_l) + \Gamma (T_e - T_l) \qquad (2.2)$$

Here C_e and C_l are the heat capacities of electrons and lattice respectively, k_e and k_l the respective heat conductivities, Γ is the coupling coefficient between the two subsystems, and Q is the laser source contribution.

The divergence term in both equations describes the heat diffusion in the electron and lattice subsystems according to Fourier's law[19], while the

coupling term describes the intensity of the heat flow between electrons and lattice.

For ultra-short laser pulses the equations can be used to estimate the maximum temperature of the electron after the laser pulse by neglecting both the coupling and diffusion terms and by taking into account the linear dependence of the electron heat capacity from temperature $C_e = C'_e T_e$, equation 2.1 becomes

$$\frac{1}{2}C'_e\frac{\partial T_e^2}{\partial t} = Q(\mathbf{r}, t) \tag{2.3}$$

This would then allow to describe the evolution of the system ignoring the laser contribution[20, 21].

For longer pulses, e.g. the 20 ns ones employed in this work, this approximation does not hold true because both diffusion and heat transfer happen during the pulse itself[11].

For example the competing effect of energy deposition and heat diffusion in a nanosecond laser pulse can lead to a cascade of thermal effects: first the front of the laser pulse can heat the material to its melting point, here the energy of the pulse is converted to latent heat of fusion by the formation of a melting front which penetrates inside the surface; vaporisation on the surface of the material may follow the melting and if the fluence of the laser is enough it can even give rise to phase explosion when the deposited energy is enough to drive the system to the limit of thermodynamic stability[11].

2.1.2 Expanded Two Temperature Model for Semiconductors

As written above the excitation of semiconductors depends strongly if the photon energy is above or below the band gap of the material.

The relevant case here is the first, therefore the treatment of the excitation requires to take into account single-photon intraband excitation, two-photon absorption (with potential higher order contributions) and single-photon intraband excitations (free-carrier excitations)[10].

This is modeled by an extension of the TTM which considers the free carrier population n_F[22]. In essence the two equations 2.1 and 2.2 of the normal TTM are integrated with the evolution of the free-carrier evolution:

$$\frac{\partial n_F}{\partial t} = \frac{\alpha_{SPA} I}{\hbar \omega} + \frac{\beta_{TPA} I^2}{2 \hbar \omega} + \delta_{II} n_F - \gamma n_F^3 - \nabla \cdot \mathbf{j} \qquad (2.4)$$

The first term describes single-photon absorption, the second, fittingly, describes two-photon absorption, and the third term describes impact ionisation. The two remaining terms represent the loss of free carriers by auger decay and from diffusion with particle current $\mathbf{j}$[23].

The inclusion of carrier density is important because properties like the reflectivity and the free-carrier absorption coefficient are strongly influenced by the it[23, 24].

In the opposite case, a more correct representation of the excitation would be Keldysh Model [25] which requires a regime of strong field excitation, dominated by multi-photon absorption and tunneling excitation. This discussion is not necessary for the conditions relevant to this work.

2.2   Phase Explosion

As previously mentioned and as one can see in fig:2.3, ablation of material from a target can be obtained via different processes.

In the pulse duration - laser fluence region relevant to the experimental work performed in the scope of my thesis (20 ns pulse duration, $\sim 40 - 50 J/cm^2$) the relevant phenomenon is Phase Explosion, also called homogeneous boiling [3, 26].

As introduced at the end of section 2.1.1, the material irradiated with a pulse in the ns range undergoes a cascade of thermal processes:

1. heating of the surface up to the melting point

2. formation of a superficial molten layer

3. heating to the boiling point of the material (with possible evaporation from the surface)

4. overheating of the molten layer to a superheated liquid and to the limits of thermodynamical equilibrium.
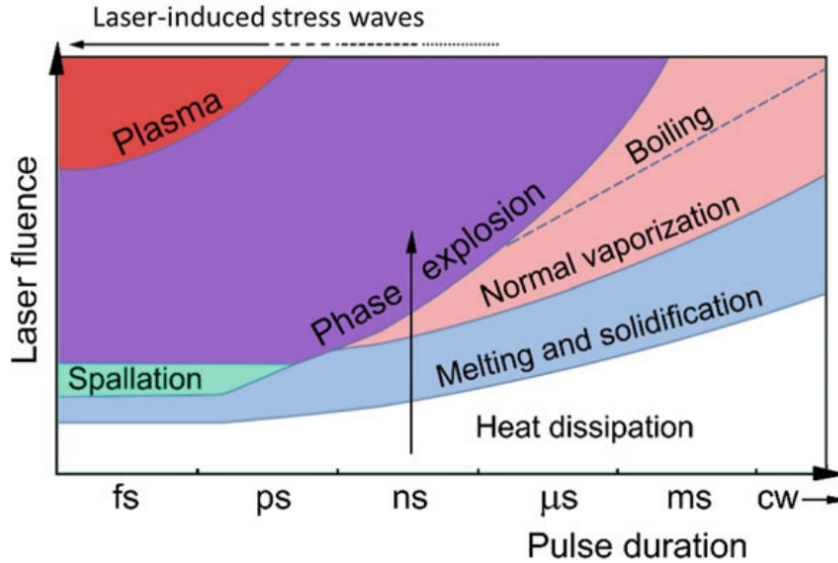
Figure 2.3: Diagram showing typical mechanisms of mass ejection as a function of laser pulse duration. The boundaries for melting, spallation and phase explosion correspond to the onset of the specific mechanisms, while the vaporization and plasma lines are defined qualitatively. Under laser excitation of a given duration the irradiated material is subjected to a cascade of phenomena. Reproduced from [11]

In these conditions processes like normal boiling are thermodynamically suppressed[26] and phase explosion results the most efficient mechanism for the ablation of nanodroplets.

When the heating of a material happens at time scales lower than the typical vapor bubble nucleation time ($\sim 100ns$), the material becomes a superheated liquid [26]. When the laser energy is enough to bring the temperature of the superheated liquid up to $\sim 90\%$ of the critical temperature T_C, thermodynamical fluctuations inside the molten layer can trigger homogeneous nucleation of vapor bubbles [27].

This process is schematised in the phase diagram shown in fig:2.4, the green curve represents the binodal line which is the collection of all P-T values where the liquid phase and vapor phase coexist in thermodynamical equilibrium (normal boiling conditions).

Laser irradiation causes fast heating conditions (red curve), which cause
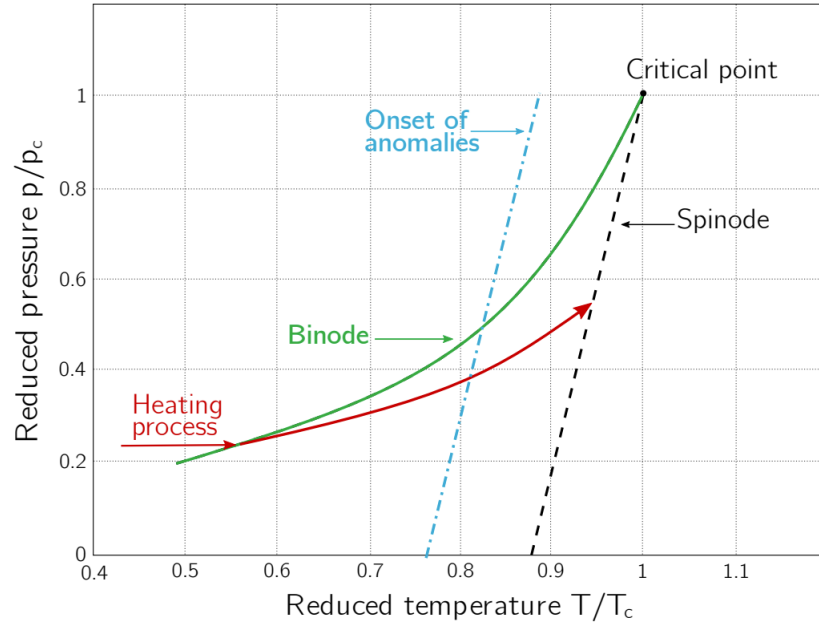
Figure 2.4: Representative phase diagram near the critical temperature.

the liquid to reach the boiling temperature without the formation of vapor bubbles, entering in a metastable superheated liquid state, as stated above. Thermodynamical stability of this state is in principle possible up to the spinodal line (black dashed line), the locus of points on the P-T plane which represent the thermodynamic limit for stability under infinitesimal fluctuations.

In the region ranging from $\sim 0.8 T/T_c$ ("anomaly onset") up to the spinodal line the properties of the metastable superheated liquid (enthalpy, density) undergo strong fluctuation, in particular density fluctuation can push the superheated liquid out of equilibrium by causing homogeneous nucleation of vapor bubbles.

I will cover some aspects of nucleation theory to better elucidate the phenomenon of phase explosion.

As shown in fig:2.5, when the system approaches the critical point the density of the liquid ρ_l and the density of the vapor ρ_v approach the same value ρ_C at the critical temperature. This behaviour is due to the exponential dependence of the rate of homogeneous nucleation of critical vapor bubbles
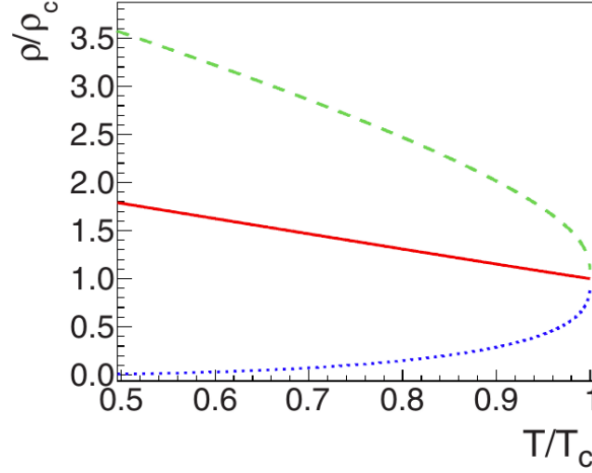
Figure 2.5: reduced liquid density ρ_l/ρ_C (green line), reduced vapor density ρ_v/ρ_C (blue line) and average density (red line). Reproduced from [28].

per unit volume from the temperature as shown in [28]:

$$J_s = n_l \sqrt{\frac{6\sigma}{(3-b)\pi m}} \exp\left(-\frac{\Delta h_v}{RT}\right) \exp\left(-\frac{W_c}{k_B T}\right) \tag{2.5}$$

In equation 2.5 n_l is the number density of the liquid, σ is the surface tension of the material, the coefficient $b = 1 - p_l/p_v$ contains the contributions from the pressure of the liquid p_l and the pressure of the vapor inside the bubbles calculated in equation 2.6[29]; m is the mass of one atom/molecule, Δh_v is the enthalpy of vaporisation and W_c is the energy barrier to reach the critical radius, shown in equation 2.7.

$$p_v = p_s \exp\left((p_l - p_s)\frac{v_l}{k_B T}\right) \tag{2.6}$$

Here p_s is the saturated vapour pressure obtained from the Clausius-Clapeyron equation and v_l is the molar volume of the liquid phase.

In order to become stable a vapor bubble has to reach a critical radius $r_c = 2\sigma/(p_v - p_l)$, vapor bubbles with $r > r_c$ start growing spontaneously, but as written above there is an energy barrier to reach the critical radius:

$$W_c = \frac{4}{3}\pi r_c^2 \sigma = \frac{16\pi\sigma^3}{3\left(p_v - p_l\right)^2} \tag{2.7}$$

Figure 2.6 shows the behaviour of both critical radius r_c and the critical vapor bubble nucleation rate J_s. The sharp decrease in the critical radius coincides with an increased nucleation rate. In particular at $\sim 0.9T_C$ the nucleation rate increases by several orders of magnitude, which leads to a very sharp increase in vapor density.
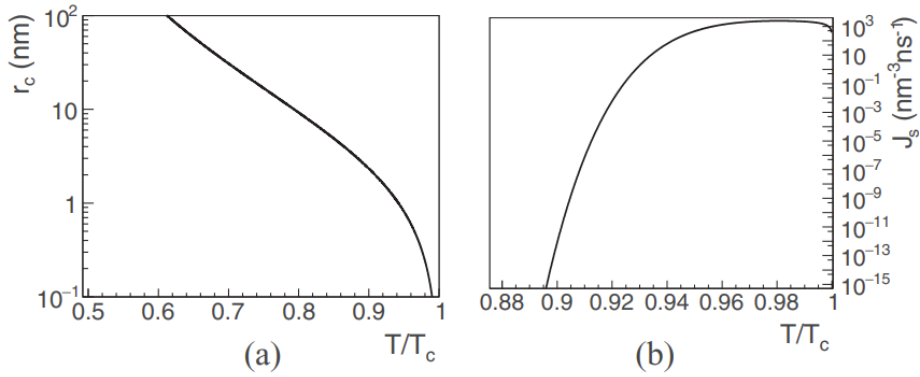
Figure 2.6: (a) critical radius of vapor bubbles as function of the temperature in the metastable fluid and (b) nucleation rate of vapor bubbles calculated for iron. Reproduced from [28].

When the vapor bubbles formed by homogeneous nucleation merge, forming a sort of percolation network, the pressure in the material causes the expulsion of the vapor and the liquid droplets trapped inside the network, as shown in fig:2.7 [28].

Phase explosion, as suggested by fig:2.3, is a threshold process. From literature, many works [30–33] show that the ablation threshold of graphite and silicon-carbide lie around $\sim 1 - 5J/cm^2$. The experiments performed in this work are conducted with laser fluence in the $40 - 50J/cm^2$ range.
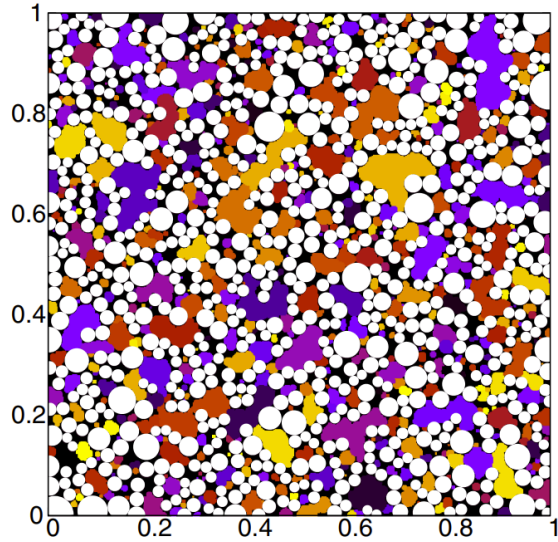
Figure 2.7: 2D simulation of supercritical vapor bubbles (white) with liquid intervolumes (different colors). Reproduced from [28].

2.3 Phase Explosion under confinement

The previous description of phase explosion can be considered complete for ablation performed in low pressure environments (vacuum or gaseous atmosphere).

The presence of a confining layer in front of the target induces two main effects:

- High pressure inside the ablation plume

- High cooling rate of the plume and emitted droplets/particles.

Both phenomena are direct consequence of the strong confinement given by the liquid layer, as can be seen in fig:2.8.

First, the size of the plumes in water is an order of magnitude lower than the size of the plume in air. This reduced size corresponds to increased pressure inside. The pressure is further increased by the emission of a shockwave inside the material[35, 36].

The lower lifetime of the plume in water is related to increased cooling rate when compared with ablation in air. The plume expands in a dense
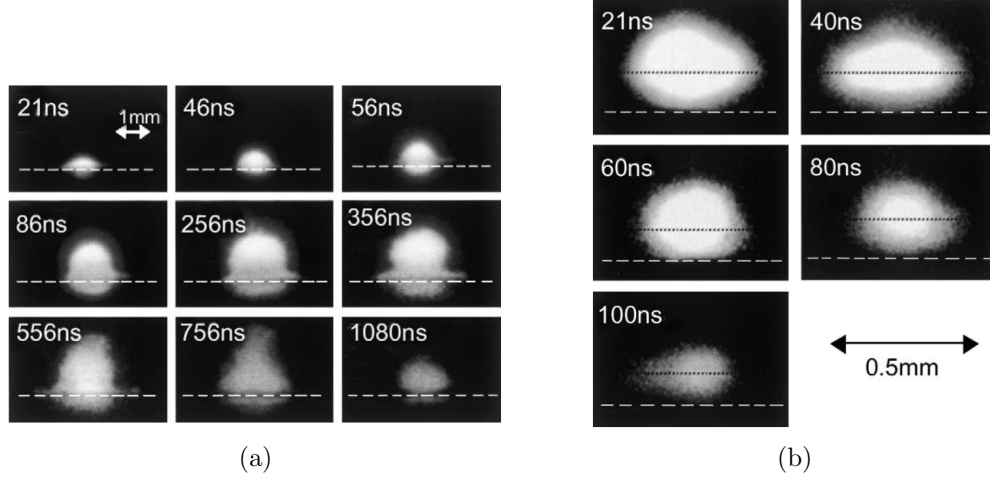
Figure 2.8: Comparison of ablation plumes from laser ablation of graphite in air (left) and water (right), reproduced from [34]

environment allowing for efficient dissipation of thermal energy by collisional cooling, leading to cooling rates of the order of $10^{10} - 10^{11} K/s$[36].

The dense environment allows also for the interaction of the ablation plume with the confining medium, leading to chemical reaction between the species contained in the two subsystems at the boundary between them (this also applies for ablation in controlled atmosphere, although with less efficiency [3, 14, 36]).

If one considers for example the ablation of graphite in water, Gorrini et al. [37] estimate the conditions obtained by PLAL to reach maximum temperature between $4500 - 6000K$ and maximum pressure of $3.17GPa$. Similar pressure values are estimated by Basso et al. [14] at $3.5GPa$ for ablation of graphite in liquid nitrogen.

The estimation of the pressure inside the plume is obtained by employing Fabbro's Model:

$$p = \sqrt{\frac{\alpha}{2\alpha + 3} Z I_0}$$
(2.8)

Where α is the fraction of the internal energy of the plasma generated by thermal energy, which is usually set as $\alpha = 0.25$ as per [38], I_0 is an approximation of the intensity of the laser, set to a constant over the duration

of the laser pulse, and Z is the reduced shock impedance of the system:

$$Z = \frac{2Z_g Z_m}{Z_g + Z_m} \tag{2.9}$$

With Z_g the shock impedance of graphite and Z_m the shock impedance of the medium.

Summarising the main features of PLAL is the formation of extreme conditions (pressure of the order of $10^9 Pa$ and temperature ranging between $5000 - 6000K$) associated with cooling rates in the order of more than $10^{10}K/s$, all confined regions with a maximum extension of few hundreds of μm.

2.4 Thermodynamics of the formation of nanodiamonds
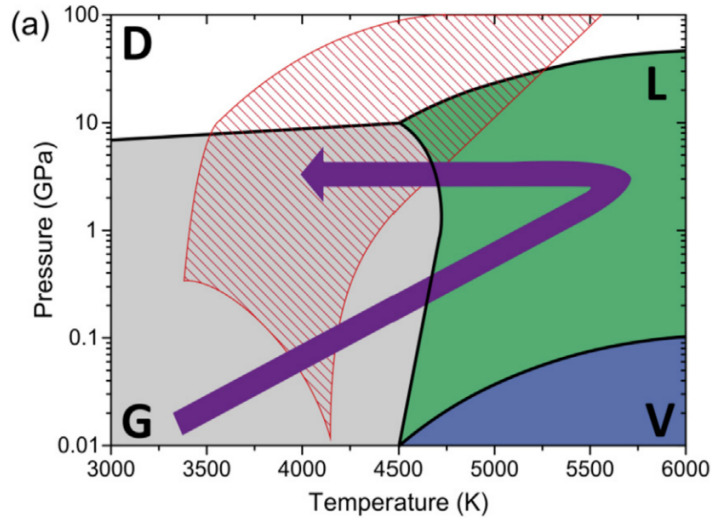
Figure 2.9: Phase diagram of carbon near the melting temperature of graphite. The different quadrants represent different carbon phases: G graphite, L liquid carbon, V vapor, D diamond. The superimposed red lines represent the region where metastable diamond like states can form inside the supercooled nanodroplets. Reproduced from [14]

The results shown at the end of the previous section are summarised by fig:2.9, the purple arrow represents the evolution of the conditions inside the ablation plume.

As can be seen, the process does not reach pressures high enough to produce diamond via HPHT processes[3, 39], which is also supported by an observed shift to higher pressures of the carbon triple point for carbon nanoparticles [40]. Instead the proposed mechanism of formation is based on the quenching of metastable liquid states.

During ablation there is the formation of a molten layer of carbon on the source of the material which undergoes phase explosion, with the emission of nanodroplets of liquid carbon [27, 28]. The presence of liquid carbon inside the ablation plume is necessary because the nucleation of NDs happens in strong undercooling conditions [3, 14, 37].

The diagonal red lines in fig:2.9 indicate a region for metastable diamond nucleation according to Gorrini et al. [37], and defined as the region enclosed by the analytical continuation of diamond-liquid-carbon coexisting lines according to different works [41–43].

This region represents a metastable state which is also called "diamond-like-liquid" carbon [41]. Here the energy barrier for diamond nucleation is lower than that of graphite formation [42], the internal configuration of the liquid carbon is then frozen by the rapid cooling of the system, which prevents further transitions to the stable phase (graphite) [39].

The nucleation of nanodiamonds does require both the high cooling rate and the high-pressure induced by the shockwave. In fact as pressure decreases the nucleation of NDs stops and the remaining liquid carbon forms sp_2 carbon structures around the NDs [39]. The time interval in which these conditions are realised in the system is estimated to be two times the duration of the laser pulse [35, 44].

Bibliography

[1] Jianming Zhang, Mohamed Chaker, and Dongling Ma. Pulsed laser ablation based synthesis of colloidal metal nanoparticles for catalytic applications. *Journal of colloid and interface science*, 489:138–149, 2017.

[2] J Gonzalo, A Perea, D Babonneau, Carmen N Afonso, N Beer, J-P Barnes, Amanda K Petford-Long, DE Hole, and Paul D Townsend. Competing processes during the production of metal nanoparticles by pulsed laser deposition. *Physical Review B*, 71(12):125420, 2005.

[3] Luca Basso, F Gorrini, M Cazzanelli, N Bazzanella, A Bifone, and A Miotello. An all-optical single-step process for production of nanometric-sized fluorescent diamonds. *Nanoscale*, 10(12):5738–5744, 2018.

[4] Paraskevi Pouli, Mohamed Oujja, and Marta Castillejo. Practical issues in laser cleaning of stone and painted artefacts: optimisation procedures and side effects. *Applied Physics A*, 106:447–464, 2012.

[5] Ettore Maggiore, Inam Mirza, David Dellasega, Matteo Tommasini, and Paolo M Ossi. Sliding on snow of aisi 301 stainless steel surfaces treated with ultra-short laser pulses. *Applied Surface Science Advances*, 7:100194, 2022.

[6] Camilo Florian, Sabrina V Kirner, Jörg Krüger, and Jörn Bonse. Surface functionalization by laser-induced periodic surface structures. *Journal of Laser Applications*, 32(2), 2020.

[7] Q Xie, MH Hong, HL Tan, GX Chen, LP Shi, and TC Chong. Fabrication of nanostructures with laser interference lithography. *Journal of alloys and compounds*, 449(1-2):261–264, 2008.

[8] F Ruffino, A Pugliara, E Carria, L Romano, C Bongiorno, G Fisicaro, A La Magna, C Spinella, and MG Grimaldi. Towards a laser fluence dependent nanostructuring of thin au films on si by nanosecond laser irradiation. *Applied surface science*, 258(23):9128–9137, 2012.

[9] Dieter Bäuerle. *Laser processing and chemistry*. Springer Science & Business Media, 2013.

[10] Peter Balling. Laser coupling and relaxation of the absorbed energy: Metals, semiconductors, and dielectrics. *Handbook of Laser Micro-and Nano-Engineering*, pages 1–58, 2020.

[11] Maxim V Shugaev, Miao He, Yoann Levy, Alberto Mazzi, Antonio Miotello, Nadezhda M Bulgakova, and Leonid V Zhigilei. Laser-induced thermal processes: heat transfer, generation of stresses, melting and solidification, vaporization, and phase explosion. In *Handbook of Laser Micro-and Nano-Engineering*, pages 83–163. Springer, 2021.

[12] Xianfan Xu. Phase explosion and its time lag in nanosecond laser ablation. *Applied Surface Science*, 197:61–66, 2002.

[13] Antonio Miotello and Roger Kelly. Critical assessment of thermal models for laser sputtering at high fluences. *Applied Physics Letters*, 67(24):3535–3537, 1995.

[14] Luca Basso, Nicola Bazzanella, Massimo Cazzanelli, and Antonio Miotello. On the route towards a facile fluorescent nanodiamonds laser-synthesis. *Carbon*, 153:148–155, 2019.

[15] Massimo Cazzanelli, Luca Basso, Claudio Cestari, Nicola Bazzanella, Enrico Moser, Michele Orlandi, Alessandro Piccoli, and Antonio Miotello. Fluorescent nanodiamonds synthesized in one-step by pulsed laser ablation of graphite in liquid-nitrogen. *C*, 7(2):49, 2021.

[16] Zhibin Lin, Leonid V Zhigilei, and Vittorio Celli. Electron-phonon coupling and electron heat capacity of metals under conditions of strong electron-phonon nonequilibrium. *Physical Review B*, 77(7):075133, 2008.

[17] SK Sundaram and Eric Mazur. Inducing and probing non-thermal transitions in semiconductors using femtosecond laser pulses. *Nature materials*, 1(4):217–224, 2002.

[18] SI Anisimov, BL Kapeliovich, TL Perelman, et al. Electron emission from metal surfaces exposed to ultrashort laser pulses. *Zh. Eksp. Teor. Fiz*, 66(2):375–377, 1974.

[19] Frederick Reif. Fundamentals of statistical and thermal physics, 1998.

[20] K Vestentoft and P Balling. Formation of an extended nanostructured metal surface by ultra-short laser pulses: single-pulse ablation in the high-fluence limit. *Applied Physics A*, 84:207–213, 2006.

[21] Bjarke Holl Christensen, K Vestentoft, and P Balling. Short-pulse ablation rates and the two-temperature model. *Applied Surface Science*, 253(15):6347–6352, 2007.

[22] Henry M Van Driel. Kinetics of high-density plasmas generated in si by 1.06-and 0.53-μm picosecond laser pulses. *Physical Review B*, 35(15):8166, 1987.

[23] A Rämer, O Osmani, and B Rethfeld. Laser damage in silicon: Energy absorption, relaxation, and transport. *Journal of Applied Physics*, 116(5), 2014.

[24] Anika Rämer, Lasse Haahr-Lillevang, Baerbel Rethfeld, and Peter Balling. Modeling the transient optical parameters in laser-excited band gap materials. *Optical Engineering*, 56(1):011015–011015, 2017.

[25] LV Keldysh et al. Ionization in the field of a strong electromagnetic wave. *Sov. Phys. JETP*, 20(5):1307–1314, 1965.

[26] Antonio Miotello and Roger Kelly. Laser-induced phase explosion: new physical problems when a condensed phase approaches the thermodynamic critical temperature. *Applied Physics A*, 69(Suppl 1):S67–S73, 1999.

[27] Alberto Mazzi and Antonio Miotello. Simulation of phase explosion in the nanosecond laser ablation of aluminum. *Journal of colloid and interface science*, 489:126–130, 2017.

[28] Alberto Mazzi, Federico Gorrini, and Antonio Miotello. Liquid nanodroplet formation through phase explosion mechanism in laser-irradiated metal targets. *Physical Review E*, 92(3):031301, 2015.

[29] Pablo G Debenedetti. Metastable liquids: concepts and principles. 1996.

[30] Sucharita Sinha. Nanosecond laser ablation of graphite: A thermal model based simulation. *Journal of Laser Applications*, 30(1), 2018.

[31] A Semerok, SV Fomichev, J-M Weulersse, F Brygo, P-Y Thro, and Ch Grisolia. Heating and ablation of tokamak graphite by pulsed nanosecond nd-yag lasers. *Journal of Applied Physics*, 101(8), 2007.

[32] Jacek Hoffman. The effect of recoil pressure in the ablation of polycrystalline graphite by a nanosecond laser pulse. *Journal of Physics D: Applied Physics*, 48(23):235201, 2015.

[33] R Reitano and P Baeri. Nanosecond laser-induced thermal evaporation of silicon carbide. *International journal of thermophysics*, 17:1079–1087, 1996.

[34] Kotaro Saito, Kazuhiro Takatani, Tetsuo Sakka, and Yukio H Ogata. Observation of the light emitting region produced by pulsed laser irradiation to a solid–liquid interface. *Applied surface science*, 197:56–60, 2002.

[35] Remy Fabbro, J Fournier, P Ballard, D Devaux, and J Virmont. Physical study of laser-produced plasma in confined geometry. *Journal of applied physics*, 68(2):775–784, 1990.

[36] Zijie Yan and Douglas B Chrisey. Pulsed laser ablation in liquid for micro-/nanostructure generation. *Journal of Photochemistry and Photobiology C: Photochemistry Reviews*, 13(3):204–223, 2012.

[37] Federico Gorrini, Massimo Cazzanelli, Nicola Bazzanella, Raju Edla, M Gemmi, V Cappello, J David, C Dorigoni, A Bifone, and Antonio Miotello. On the thermodynamic path enabling a room-temperature, laser-assisted graphite to nanodiamond transformation. *Scientific reports*, 6(1):35244, 2016.

[38] GW Yang. Laser ablation in liquids: Applications in the synthesis of nanocrystals. *Progress in Materials Science*, 52(4):648–698, 2007.

[39] Luca Basso, Fe Gorrini, N Bazzanella, M Cazzanelli, C Dorigoni, A Bifone, and A Miotello. The modeling and synthesis of nanodiamonds by laser ablation of graphite and diamond-like carbon in liquid-confined ambient. *Applied Physics A*, 124:1–7, 2018.

[40] JA Viecelli, S Bastea, JN Glosli, and FH Ree. Phase transformations of nanometer size carbon particles in shocked hydrocarbons and explosives. *The Journal of Chemical Physics*, 115(6):2730–2736, 2001.

[41] Luca M Ghiringhelli, Jan H Los, Evert Jan Meijer, A Fasolino, and Daan Frenkel. Modeling the phase diagram of carbon. *Physical review letters*, 94(14):145701, 2005.

[42] A Yu Basharin, VS Dozhdikov, AV Kirillin, MA Turchaninov, and LR Fokin. Phase diagram with a region of liquid carbon-diamond metastable states. *Technical Physics Letters*, 36:559–562, 2010.

[43] Jan M Zazula. On graphite transformations at high temperature and pressure induced by absorption of the lhc beam. Technical report, CERN-LHC-Project-Note-78, 1997.

[44] L Berthe, R Fabbro, P Peyre, L Tollier, and E Bartnicki. Shock waves from a water-confined laser-generated plasma. *Journal of Applied Physics*, 82(6):2826–2832, 1997.

Chapter 3

Electronic and Optical Properties of the Nitrogen Vacancy and Silicon Vacancy Centers in Diamond

As shown in Chapter 1, diamond can host a variety of color centers, defects or impurities that can be excited by light to which the host material is transparent and emit light at certain wavelengths which give the host crystal a specific color.

These color centers can be composed of defects like vacancies or disclinations, by atomic impurities in interstitial or substitutional crystallographic sites, or a combination of the two.

Both the color centers I will discuss in my thesis are of the latter configuration, indeed the Nitrogen-Vacancy center is composed of a substitutional nitrogen adjacent to a crystal vacancy, while the Silicon-Vacancy center is composed of an interstitial Silicon atom surrounded by two vacancies in the nearest crystal sites.

The Nitrogen Vacancy (NV) center has been first observed in 1965 [1] and has been studied in the following years associating it to the emission around 640 nm and revealing some of its electronic properties [2]. The interest in NV centers was renewed in 1997 when spin manipulation at room temperature was achieved [3] and owing to the importance of this discovery the number of publications concerning NV centers exponentially increased since.

In the last years NV centers have become prominent as a quantum system

for quantum computing and quantum sensing due to the spin dependent optical properties and luminescence stability. The main disadvantage of NV centers is their emission spectrum which, due to strong coupling between the electronic wave function and the phonons of the crystalline lattice, has a width of about 100 nm with only 3-5% of the emission being in the zero-phonon line (ZPL).

While there is active research in the field of quantum optics to find ways to enhance ZPL emission from NV centers, there are also a variety of alternative color centers that can be studied, particularly from group IV elements.

One of such alternatives is the Silicon-Vacancy (SiV) center, which is composed of an interstitial SiV center surrounded by two vacancies[4]. In contrast to the NV center most of the emission (about 70%) is inside the ZPL at 738 nm, with much lower phonon side band contribution.

While the NV center has been extensively studied in the past three decades, a complete description of the SiV center electronic properties was formulated only in recent years.

In this chapter I will provide an introductory theoretical description of the two fluorescent color centers mentioned above in a way that is conductive to describe the aim of the work and the experiments performed, therefore a complete and exhaustive treatment of the theory behind the physics of the color centers is far beyond the scope of this work.

In section 3.1 I will describe the physical structure of the NV and SiV centers with some brief discussion about the symmetry of the defects. Sections 2.2 and 2.3 will go over the optical and electronic properties of the color centers respectively. Lastly in section 2.4 I will give a brief overview of the spin state Hamiltonian focusing on the terms relevant for sensing measurements.

3.1   Physical structure and symmetry configuration

3.1.1   Nitrogen-Vacancy center structure

As stated above the NV center is a point defect in the diamond structure characterized by a substitutional nitrogen atom located at a diamond lattice site with a carbon-vacancy as its nearest neighbor, see fig:3.1. The NV axis aligns with the [111] crystallographic direction of the diamond lattice.

The center shows C3v symmetry, with six group elements: two C3 rotations ($\pm 2\pi/3$) around the NV axis, three σ_v reflections with respect to the plane containing the NV axis and one carbon atom, and the identity element E.
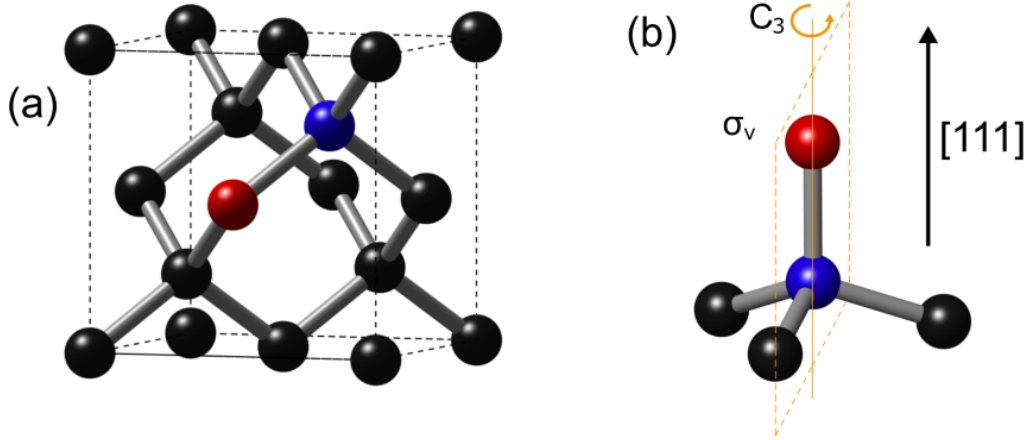
Figure 3.1: Structure of the NV center, the constituent of the NV center are shown in red (Nitrogen), blue (Vacancy) and black. (b) the symmetry operations of the NV center.

The three carbon atoms surrounding the vacancy have dangling bonds which provide three unpaired electrons to the system. Combined with the two outer-shell electrons of nitrogen, these electrons form the five-electron configuration of the neutral nitrogen-vacancy center (NV^0). Although spin manipulation of NV^0 is theoretically possible [5, 6], experimental detection of the ground state ODMR (Optically Detected Magnetic Resonance) signal has not been observed yet.

The negatively charged NV^- center, which forms when the vacancy captures a sixth electron from the surrounding environment is much more interesting for quantum optics applications. Throughout this thesis, when referring to NV, it implicitly pertains to the NV^- center.

In this configuration, the center possesses two unpaired electrons and a ground state with a spin S = 1. As a result, the NV^- center allows for easy manipulation of the sublevels in the ground state and control of each level population is highly sensitive to external fields.

3.1.2   Silicon-Vacancy center structure

The SiV center is a point defect in the diamond structure characterized by a substitutional silicon atom surrounded by a divacancy. In [7], the authors simulated the SiV center using a substitutional Si impurity and an adjacent vacancy, oriented along the $\langle 111 \rangle$ crystal axes. They obtained from their calculations that the Si atom is not stable on its position but rather moves along the [111] axis to an interstitial position, surrounded by two vacancies in the crystal lattice (also referred to as split vacancy configuration) giving the defect a D_{3d} symmetry.
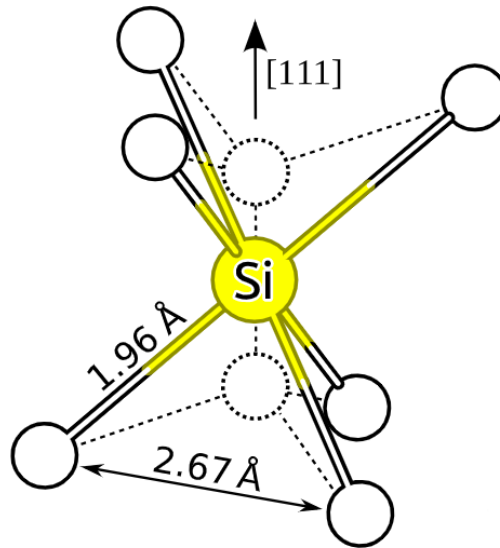
Figure 3.2: Representation of the structure of the SiV center. Reproduced from [4].

The D_{3d} group contains 12 symmetry operations: two rotations around the primary axis, which is the vacancy-silicon-vacancy axis, three rotations, one for each of three secondary axes of rotation perpendicular to the main symmetry axis (as shown in fig:3.3), one inversion for which the silicon position is the center, three reflections with respect to the plains containing the main axis and two carbon atoms, two improper rotations around an axis corresponding to the main symmetry axis, and lastly the identity.

Again the carbons surrounding the vacancy provide electrons to the system, with the difference that now there are six dangling bonds therefore six
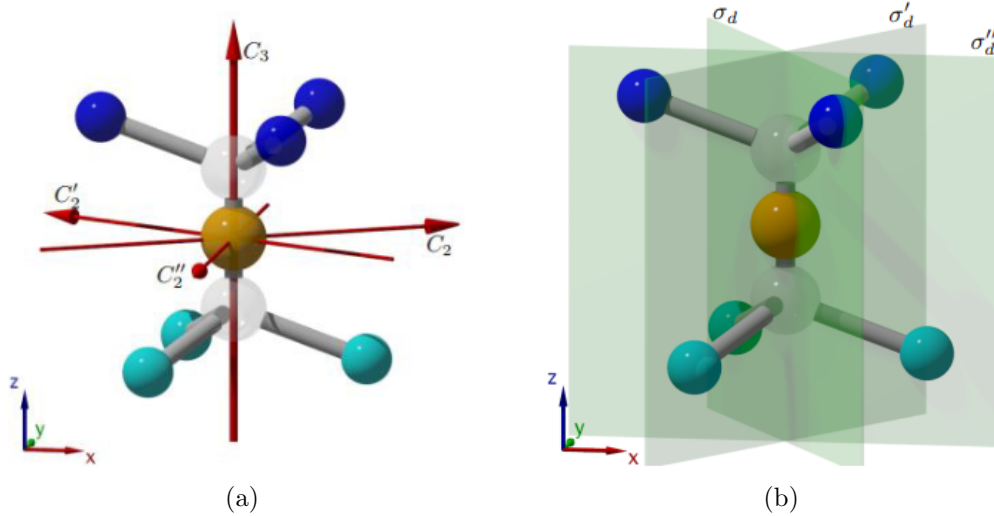
Figure 3.3: Rotation axes and symmetry planes of the SiV center. The silicon atom is represented in yellow at the center, the two transparent spheres represent the vacancies, while the blue and cyan spheres represent the carbon atoms on each side of the defect.

electrons, another four electrons come from the outer shell of the Si impurity. This ten atom configuration represents the neutral SiV^0 configuration which has a very weak emission at around 946 nm. The main focus of this thesis is the SiV^- negative defect which is an eleven-electron configuration, the ten already seen for the neutral state plus one electron from the crystalline lattice. Therefore through this work each use of the terms SiV or silicon-vacancy will refer to the negatively charged defect.

3.2 Optical properties

3.2.1 NV Center photoluminescence

In figure 3.4 one can see the emission spectrum of the NV center. As already specified before, the emission shows a very prominent phonon sideband which extends to photon wavelengths higher than 800 nm due to the strong coupling of the defect with the vibrations of the lattice. The NV center also exhibits two ZPL, one for each charge state of the defect, in particular at 575 nm

for the NV^0 neutral state and at 637 nm for the NV^- negatively charged one. The sharp ZPL indicates that the optical transition is deep within the diamond band gap, far from both the valence and the conduction band[8].
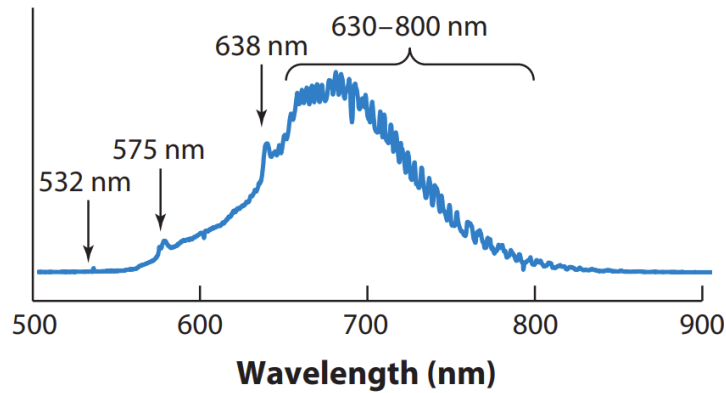
Figure 3.4: Emission of the NV center under 532 nm excitation, the ZPL of the two charge configurations are indicated at 575 nm for the neutral NV^0 defect and at 637 nm for the negatively charged NV^-. The 532 nm arrow indicates the typical nonresonant pump frequency. The 630-800 nm band corresponds to the phonon sideband of the negatively charged center. Reproduced from [9]

A very simple model of this behavior is obtained by treating the ground and excited state as harmonic oscillators with discrete vibrational states (see fig:3.5). At room temperature the electrons of most NV centers can be assumed to occupy the lowest vibrational level of the ground state. Laser excitation causes the electrons to transition from the ground state to the electronic excited state and, according to the Franck-Condon principle [10], the most probable transition occurs between the ground state and the vibronic state of the electronic excited state with wave function that overlap the most. For the NV^- these states correspond to four vibrational levels and the shift is attributed to the significant difference in the spatial distribution of the electronic states.

This behavior is also the reason why spin manipulation experiments are performed with 532 nm lasers and not with resonant 637 nm sources. Under 532 nm excitation the excited electrons rapidly decay non-radiatively to the lowest vibrational state of the excited electronic state irrespective of the specific vibrational state which allow for efficient spin manipulation.
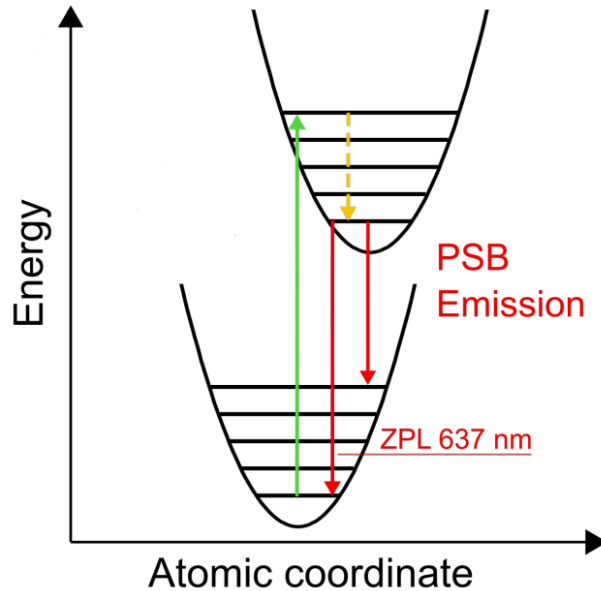
Figure 3.5: Simple representation of the vibrational levels of NV center, the green arrow represents a typical nonresonant optical excitation of the center, the yellow dashed line represents non radiative transitions in the excited state. The two parabolas represent the ground and excited electronic states, which present different equilibrium positions in the system

The phonon sideband (PSB) is instead attributed to the cumulative effect of all the possible decay transitions between different vibrational states in the two electronic levels.

3.2.2   SiV Center photoluminescence

The room temperature emission spectrum of the SiV center is reported in fig. 3.6. The dominant feature of the spectrum is the ZPL centered at 738 nm [11] with a small PSB extending in the near infrared region. The emission of single SiV centers results particularly sharp with line width lower than 1 nm [12–14] so the same conclusion as with the NV center can be reached, the defect optical transition occupies energy levels deep within the diamond band gap. For single SiV center it is also observed that the peak position can deviate from the 738 nm position [12–14] and the superposition of different narrow lines gives the typical behavior of the ensemble emission. The narrow

emission and weak PSB make the SiV center and interesting candidate for room temperature single-photon emission.
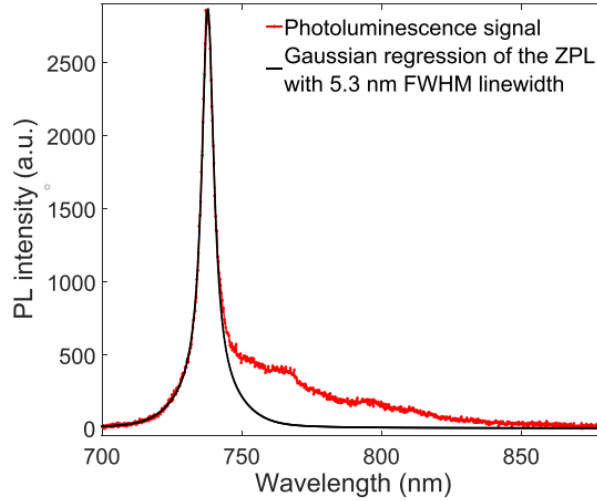
Figure 3.6: Room temperature photoluminescence emission of SiV centers under 542 nm excitation. Reproduced from [15]

Again one can model the ground and excited states as harmonic oscillators on which one can find the discrete energy levels of the vibrational states, analogously to the NV center case described by fig:3.5. As above the Franck-Condon principles guides the behavior of the system, the phonon sideband strength depends on the spatial displacement (the atomic coordinate of figure 3.5) between the charge distribution in the ground and excited state [16]. From [12, 17, 18] the linear component of the electron-phonon coupling potential represents this displacement, the small magnitude of the displacement means that one can assume that the electron density spatial distribution in the ground and excited states does not change much. The small electron-phonon coupling thus means that the ZPL the most probable transition.

In this work we focus on the detection of photoluminescence of SiV ensembles, the ideal configuration is for this purpose to use non-resonant excitation. It has been shown in literature [19] that SiV centers can be excited in a wide optical range, and so to avoid excitation of different defects it is best to excite with low energy photons. In this work we excite off resonance with both 633

nm and 532 nm lasers.

3.3 Electronic properties

To better understand the observed properties of NV centers and SiV centers, this paragraph provides a brief review of the electronic properties of the two color centers [20, 21].

3.3.1 NV center electronic properties

The NV- center has four atomic orbitals: one sp3 hybridized nitrogen orbital (σ_N) and the other three come from the three carbon atoms surrounding the vacancy, all sp3 hybridized (σ_i, i = 1, 2, 3).
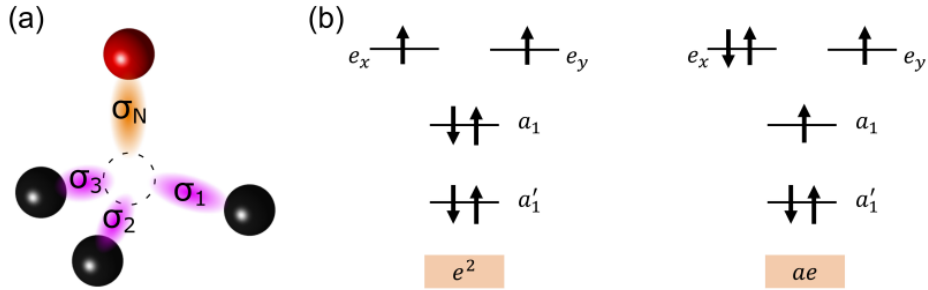
Figure 3.7: (a) representation of the atomic orbitals surrounding the vacancy. (b) representation of the molecular orbitals in the ground and excited states.

The molecular orbitals of the defect can therefore be determined by applying linear combination of the atomic orbitals, through projection operator, and imposing that the resulting combinations transform according to C3v group.

$$a_1 = \frac{\beta}{3}(\sigma_1 + \sigma_2 + \sigma_3) + \alpha\sigma_N \tag{3.1}$$

$$a_1' = \frac{\alpha}{3}(\sigma_1 + \sigma_2 + \sigma_3) + \beta\sigma_N \tag{3.2}$$

$$e_x = \frac{1}{\sqrt{6}}(2\sigma_1 + \sigma_2 + \sigma_3) \tag{3.3}$$

Configuration	State	State label	m_s
$e^2(T)$	$\lvert e_x e_y - e_y e_x \rangle \otimes \lvert \uparrow\uparrow \rangle$	${}^3A_2$	+1
	$\lvert e_x e_y - e_y e_x \rangle \otimes \lvert \downarrow\downarrow \rangle$		-1
	$\lvert e_x e_y - e_y e_x \rangle \otimes \lvert \uparrow\downarrow + \downarrow\uparrow \rangle$		0
$e^2(S)$	$\lvert e_x e_x - e_y e_y \rangle \otimes \lvert \uparrow\downarrow - \downarrow\uparrow \rangle$	$\}{}^1E$	0
	$\lvert e_x e_y + e_y e_x \rangle \otimes \lvert \uparrow\downarrow - \downarrow\uparrow \rangle$		0
	$\lvert e_x e_x - e_y e_y \rangle \otimes \lvert \uparrow\downarrow - \downarrow\uparrow \rangle$	${}^1A_1$	0
ae(T)	$\lvert a_1 e_x \rangle \otimes \lvert \uparrow\uparrow \rangle$	${}^3E$	+1
	$\lvert a_1 e_x \rangle \otimes \lvert \downarrow\downarrow \rangle$		-1
	$\lvert a_1 e_y \rangle \otimes \lvert \uparrow\uparrow \rangle$		+1
	$\lvert a_1 e_y \rangle \otimes \lvert \downarrow\downarrow \rangle$		-1
	$\lvert a_1 e_x + e_x a_1 \rangle \otimes \lvert \uparrow\downarrow + \downarrow\uparrow \rangle$		0
	$\lvert a_1 e_y + e_y a_1 \rangle \otimes \lvert \uparrow\downarrow + \downarrow\uparrow \rangle$		0
ae(s)	$\lvert a_1 e_x + e_x a_1 \rangle \otimes \lvert \uparrow\downarrow + \downarrow\uparrow \rangle$	${}^1E$	0
	$\lvert a_1 e_y + e_y a_1 \rangle \otimes \lvert \uparrow\downarrow + \downarrow\uparrow \rangle$		0

Table 3.1: NV center ground state wave functions (e^2) and excited state wave functions (ae). Triplet states are labeled T and singlet states with S. The state label comes from group theory. The last column gives the spin-projection along the NV axis of the state total spin. Adapted from [20]. The results shown here are obtained in hole notations, which is equivalent to the 6-electron notation

$$e_y = \frac{1}{\sqrt{2}} \left(\sigma_2 - \sigma_3 \right) \qquad (3.4)$$

Here, the parameters α and β are associated with the Coulomb interaction energy between electrons [20].

The six electrons of the center populate the 4 molecular orbitals following Pauli exclusion principle and Hund's rules, which say that the most stable electron configuration is the one that maximizes the spin multiplicity. Therefore the two lower levels, a0 and a1, are occupied each by two electrons. To maximize spin multiplicity the two remaining electrons occupy one the ex and the other the ey orbitals. The resulting configuration is a triplet state with S=1. In fig. 3.7 one can see both the ground state e2 and the first excited configuration ae.

The total electronic wave function is built by combination of the orbital

states with the spin states following appropriate symmetry constraints. The electronic wave functions of the NV center are detailed in Table 3.1. The labels A and E are derived from group theory and indicate how the states transform under the symmetry operations of the C3v group (A and E represent C3v irreducible representations).

The apex denotes the spin level state, either singlet or triplet. For example, the ground state is a symmetric spin triplet with an antisymmetric orbital wave function A2, therefore denoted as 3A2. The excited state 3E is more complex, encompassing six states. Notably, singlet states, although not accessible through electric dipole transitions that conserve spin from the ground state, are connected to the excited states through non-radiative transitions. This feature allows to perform electron spin manipulation and ODMR measurements.

3.3.2 SiV center electronic properties

For the SiV center the atomic orbitals involved in the molecular orbitals are more complicated than for the NV center. For each of the two vacancies we have three sp3 orbitals, one from each surrounding carbon atom and $(\sigma_i, \sigma_i',$ i=1,2,3), regarding the silicon atom there are four valence electrons which can populate the 3s, 3px, 3py and 3pz orbitals.

The molecular orbitals of the defect can be constructed in terms of the orbitals of the carbon atoms mixed with the atomic orbitals of the Si atom. By imposing the transformations of the D_{3d} group to the linear combination of the C atomic orbitals one obtains a representation called Symmetry Adjusted Linear Combination (SALC) in the form

$$a_{1g} = \frac{1}{\sqrt{6}} \left(\sigma_1 + \sigma_2 + \sigma_3 + \sigma_1' + \sigma_2' + \sigma_3' \right) \tag{3.5}$$

$$a_{2u} = \frac{1}{\sqrt{6}} \left(\sigma_1 + \sigma_2 + \sigma_3 - \sigma_1' - \sigma_2' - \sigma_3' \right) \tag{3.6}$$

$$e_{gx} = \frac{1}{\sqrt{12}} \left(2\sigma_1 - \sigma_2 - \sigma_3 + 2\sigma_1' - \sigma_2' - \sigma_3' \right) \tag{3.7}$$

$$e_{gy} = \frac{1}{2} \left(\sigma_2 - \sigma_3 + \sigma_2' - \sigma_3' \right) \tag{3.8}$$

(a) side view   (b) top view
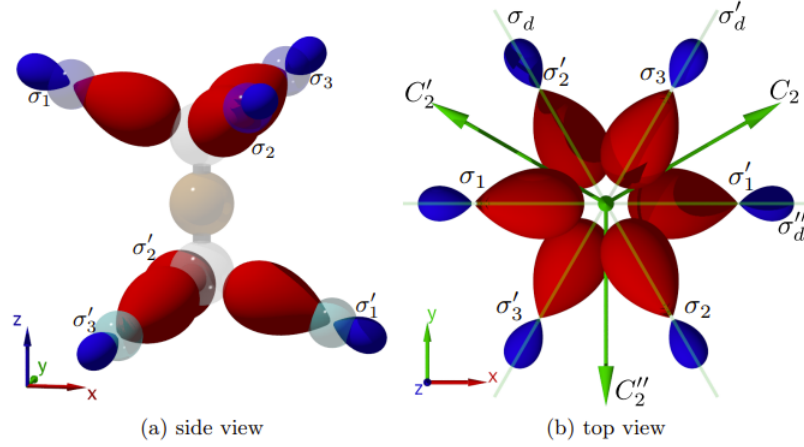
Figure 3.8: On the left the N atom is represented by the transparent orange sphere, the C atoms by the transparent blue spheres and the transparent white spheres represent the vacancies. In both figures the red lobes represent the atomic orbitals corresponding to the dangling bonds of the carbon atoms surrounding the divacancy.

$$e_{ux} = \frac{1}{\sqrt{12}} \left(2\sigma_1 - \sigma_2 - \sigma_3 - 2\sigma_1' + \sigma_2' + \sigma_3' \right) \tag{3.9}$$

$$e_{uy} = \frac{1}{2} \left(\sigma_2 - \sigma_3 - \sigma_2' + \sigma_3' \right) \tag{3.10}$$

To mix this representation with the Si orbitals one has to express the Si atomic orbitals in terms of the transformations of the symmetry group. The 3s orbital is spherical and transforms as A_{1g}, $3p_x, 3p_y$ can be expressed in terms of the E_u representation and lastly the $3p_z$ belongs to A_{2u}.

The orbitals from the Si atom and the carbon-related SALCs mix via Coulomb interaction. These direct products under Coulomb interaction are non-zero only when the Si orbitals belong to the same irreducible configuration as the SALC.

These levels can now be filled with the electrons present for the negatively charged SiV defect. As shown above the center hosts a total number of eleven electrons: six are contributed by the dangling bonds, four originate from the Si-atom and an one electron is trapped from the crystalline lattice [22].

Taking into account this spin degeneracy, the a states host two electrons of opposite spin projection, and the e states accommodate four electrons as shown in fig: 3.9.
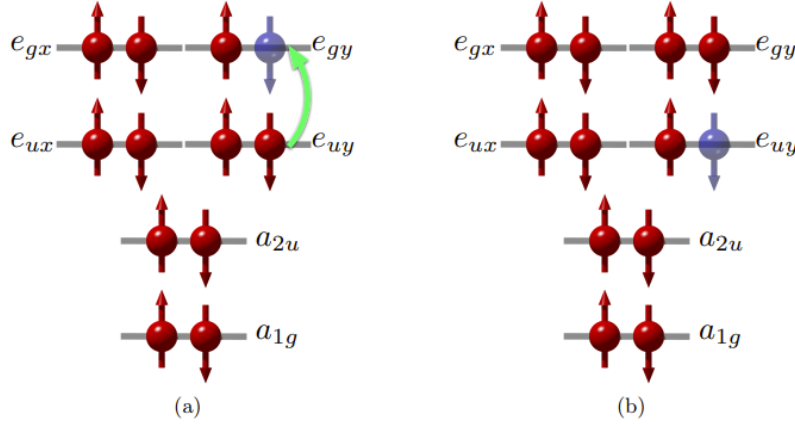
Figure 3.9: (a) ground state and (b) excited state of the SiV center. The red spheres are the electrons and the blue spheres electron holes, with the corresponding spin. The optical transition (green arrow) brings one electron from the e_{uy} state to the e_{gy}.

The ground state configuration is $a_{1g}^2 a_{2u}^2 e_u^4 e_g^3$, there is one electron hole in either the e_{gx} or e_{gy} state. This hole can be treated analogously to a single electron [20]. The total spin of the defect in this ground state configuration is equal to S = 1/2. We abbreviate this configuration in spectroscopic notation as the ^2E_g ground state. Analogously the excited states will be $a_{1g}^2 a_{2u}^2 e_u^3 e_g^4$ which will be denoted ^2E_u.

3.4 Spin Hamiltonian

This section will focus on the description of the Hamiltonians of the ground states of the two color centers.

The coupling between the spin Hamiltonian components and external perturbations such as electromagnetic fields, lattice strain and temperature variations is what allows the color centers to be employed in quantum sensing applications.

3.4.1 NV Center Hamiltonian

The basic form for the Hamiltonian of the ground state is [23]:

$$H_{GS} = H_{SS} + H_{SO} + H_{ext} \tag{3.11}$$

Where H_{SS} is the spin-spin interaction, H_{SO} is the spin-orbit term, and H_{ext} is the term that describes external interactions, which will be described in the following sections case by case. Additional terms, such as the hyperfine structure term [24] arising from the interaction between NV electrons and nuclear spins of surrounding ^{14}N or ^{13}C, are neglected because they fall outside the scope of this theoretical introduction.

Spin-spin interaction

This term arises from the dipolar coupling between the two unpaired electrons of the NV ground state. The interaction between the two magnetic dipole moments is given by [25]:

$$H_{SS} = \frac{\mu_0}{4\pi} g^2 \mu_B^2 \left(\frac{\hat{S}_1 \cdot \hat{S}_2}{r^3} - \frac{3 \left(\hat{S}_1 \cdot \hat{r} \right) \left(\hat{S}_2 \cdot \hat{r} \right)}{r^5} \right) \tag{3.12}$$

Where μ_0 is the vacuum permeability, μ_B is the Bohr magneton and $g = 2.003$ is the electron g-factor. $\hat{r}$ is the distance between the two electrons, while $\hat{S}_1$ and $\hat{S}_2$ are the associated spin operators. This equation can be rewritten more clearly as:

$$H_{SS} = D_{gs} \left(S_z^2 - \frac{\hat{S}^2}{3} \right) + E \left(S_x^2 - S_y^2 \right) \tag{3.13}$$

Here $D_{gs} = \frac{3}{2} D_z$ and $E = \frac{D_x - D_y}{2}$, from $\hat{D} = \frac{\mu_0}{8\pi} g^2 \mu_B^2 \left(\frac{r^2 \delta_{\alpha\beta} - 3\alpha\beta}{r^5} \right)$, $\alpha, \beta = x, y, z$.

The spin-spin interaction removes the degeneracy between the states with $m_S = 0$ and $m_S = \mp 1$ inside the ground state causing a longitudinal zero-field splitting $D_{GS} = 2.87 GHz$.

The transverse zero-field splitting E depends on the local strain field of the diamond lattice surrounding the defect, it is therefore sample dependent. In particular E ranges to values around 100 kHz for CVD diamond to few

MHz for nanodiamonds which naturally exhibit stronger strain than bulk diamond[26].

Spin-orbit interaction

The spin-orbit interaction term is:

$$H_{SO} = L \cdot S \lambda_z L_z S_z + \lambda_\perp \left(L_x S_x + L_y S_y \right) \tag{3.14}$$

Where λ_z is the axial strength of the spin-orbit interaction (the z axis is defined as the axis of the NV center) and $\lambda_\perp$ is the non-axial component [20]. The spin-orbit interaction removes the degeneracy of the non-zero spin states, but since this is a second order correction this effect is negligible [27]. More importantly the two terms link different states, while λ_z connects states with $m_S = 0$ with other states in the same electronic configuration and spin projections, the $\lambda_\perp$ term can be rewritten in terms of the ladder operators as $\lambda_\perp \left(L_+ S_- + L_- S_+ \right)$ and it is readily apparent that it links states with $m_S = \pm 1$ to singlet states with $m_S = 0$ in different electronic configurations. The mixing of this states is a central property of the NV center which allows optical spin initialization and read out.

Magnetic field - Zeeman splitting

An external magnetic field applied to an NV center interacts with the system modifying the ground state Hamiltonian by adding a new term which describes the Zeeman interaction:

$$H_Z = \gamma \hat{B} \cdot \hat{S} \tag{3.15}$$

where $\gamma = 2.8 MHz G^{-1}$ is the NV gyromagnetic ratio. The total Hamiltonian (neglecting spin-orbit) becomes:

$$H_{NV} = D_{gs} \left(S_z^2 - \frac{\hat{S}^2}{3} \right) + E \left(S_x^2 - S_y^2 \right) + g \mu_B \vec{B} \cdot \vec{S} \tag{3.16}$$

Here only the magnetic field component parallel to the NV axis is considered and after diagonalization of the matrix, one can find the eigenvalues $\nu_\pm$ for the Hamiltonian eigenstates $|+\rangle$ and $|-\rangle$:

$$\nu_\pm = D_{gs} \pm \sqrt{(\gamma B_z)^2 + E^2} \tag{3.17}$$

The external magnetic field removes the degeneracy between the $m_S = \pm 1$ states. By performing ODMR measurements one can thus optically measure the eigenvalues of the Hamiltonian and therefore the applied magnetic field, making the NV center an attractive nanomagnetometry probe. In fact, observing figure 3.10 one can see that the sublevels of the excited field present different coupling to the singlet shelving state via non radiative decay. When a microwave field is applied to the NV center with resonant frequency $D = 2.87MHz$ the ground state goes in the $m_S = \pm 1$ sublevels and after optical excitation the photoluminescence is reduced.

When considering NV centers with different orientations (e.g. an ensemble of randomly oriented NV center in bulk diamond or single NV centers in differently oriented crystal grains/nanodiamonds) the corresponding Zeeman splitting will be different.
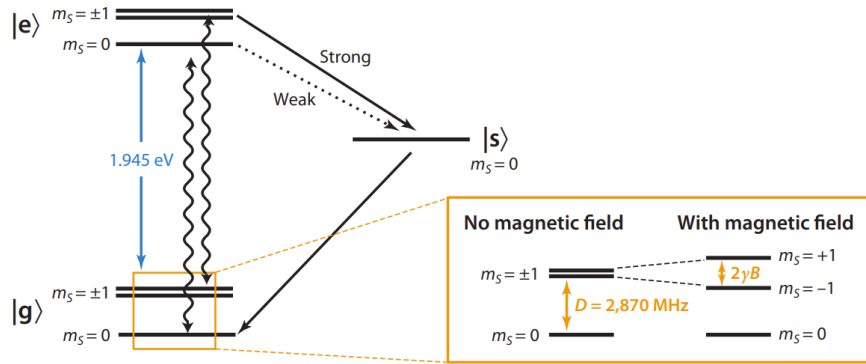
Figure 3.10: Schematic description of the action of an external magnetic field on the NV center. For zero external field, the $m_S = 0$ and $m_S = \pm 1$ sublevels are separated due to spin-spin interactions. In the presence of an external field the Zeeman effect removes the degeneracy between the $m_S = +1$ and $m_S = -1$ sublevels. Reproduced from [9]

The transverse component $B_\perp$ can be considered as a small perturbation of the Hamiltonian in the form $\frac{\gamma^2 B_\perp^2}{D}$. Since in the $< 1kHz$ regime, which is the usual experimental condition, $D \gg \gamma^2 B_\perp^2$, this corrections are usually negligible. Instead when $B_\perp \gg B_z$ the electron spin states are mixed and the spin projection is no longer a good quantum number, making magnetic field measurements difficult.

Electric/strain fields

The effects of electric fields and strain fields applied to NV centers can be described by the same term of the Hamiltonian. In fact, starting with the electric field, one can see that the effect of the axial component ϵ_z is to increase the energy separation between the $m_s = 0$ and $m_s = \pm 1$, while the transverse component $\epsilon_\perp$ removes the degeneracy from the $m_s = \pm 1$ states.

Similarly a strain field induces changes in the relative distance between the atoms of the diamond lattice. The local charge environment around the NV center is modified from that of the equilibrium case, which induces a different electric field on the defect, with the same effect as above.

The Hamiltonian of these interaction is :

$$H_E = d_{gs}^{\parallel}\epsilon_z \left(S_z^2 - \frac{\overrightarrow{S}^2}{3} \right) + d_{gs}^{\perp}\epsilon_x \left(S_y^2 - S_x^2 \right) + d_{gs}^{\perp}\epsilon_y \left(S_x S_y - S_y S_x \right) \quad (3.18)$$

Where $d_{gs}^{\parallel} = 0.35 Hz \left(\frac{V}{cm} \right)^{-1}$ and $d_{gs}^{\perp} = 17 Hz \left(\frac{V}{cm} \right)^{-1}$ are respectively the axial and non-axial components of the electric field coupling constant, ϵ_i with i=(x,y,z) are the components of the electric field, remembering that the NV axis represents the z direction.

Supposing E=0 for simplicity and already written in the $|0\rangle, |+1\rangle, |-1\rangle$ basis as defined in the spin-spin section. Defining $\epsilon_\perp = \sqrt{\epsilon_x^2 + \epsilon_y^2}$ and diagonalizing the matrix one obtains the eigenvalues for the $m_s = \pm 1$ states:

$$\nu_\pm = D_{gs} + d_{gs}^{\parallel}\epsilon_z \pm d_{gs}^{\perp}\epsilon_\perp \quad (3.19)$$

The difference between the electric and strain fields is the magnitude and units of the coupling constants, which for the strain field become $d_{gs}^{\parallel} = 5.46 GHz$ and $d_{gs}^{\perp} = 19.63 GHz$.

Temperature and Pressure

Temperature fluctuations causes the crystal lattice to expand or to contract [28], therefore thermal fluctuations cause a shift of the zero-field splitting D_{gs} by a factor of $-78.6 \frac{kHz}{K}$ [29].

$$\frac{1}{D_{gs}} \frac{dD_{gs}}{dT} = \frac{1}{D_{gs}} \frac{d\left\langle \left(r_{12}^2 - 3z_{12}^2 \right) / r_{12}^2 \right\rangle}{dR} \frac{dR}{dT} \quad (3.20)$$

R is the distance between two carbon atoms in diamond lattice,r_{12} is the displacement between two spins andz_{12} is the component along NV axis of r_{12}.

Analogously pressure brings to a linear shift of the ground-state splitting D_{gs} by a factor $-14.58\frac{MHz}{GPa}$ [30].

In particular, pressure increases the electronic density in the vacancy site, while increasing temperature increases the separation between the atoms and therefore reduces the electronic density. Another consequence is the shift of the ZPL line emission toward lower wavelength

3.4.2   SiV Center Hamiltonian

The basis states obtained in section 3.3 are energetically degenerate, but if one observes the emission of the SiV center at low temperature (fig 3.11) the actual level splitting becomes apparent from the spectral fine structure exhibited.
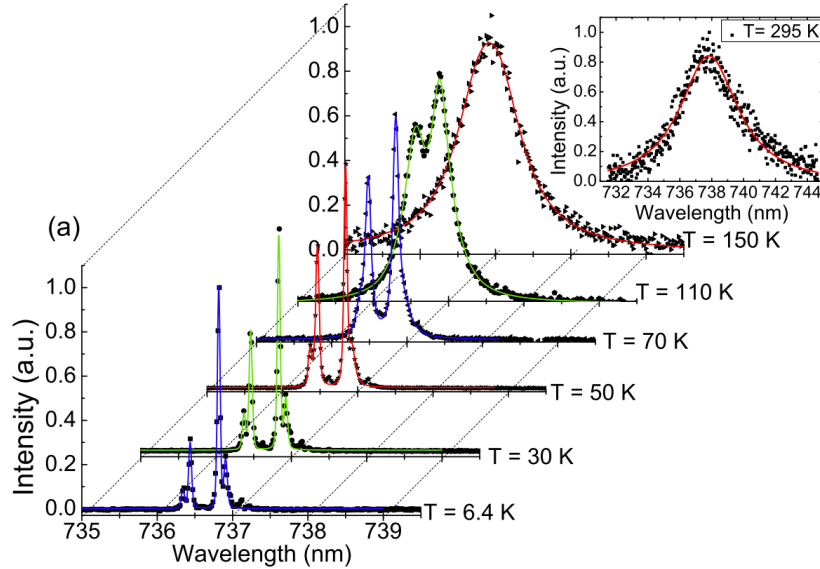

Figure 3.11: Fine structure of the emission of the SiV center observed at different temperatures. At temperature lower than 110 K the observation of four major emission peaks suggests the presence of dine structure transitions. In the inset the emission observed at room temperature. Reproduced from [31]

The level degeneracy can be described by considering perturbation terms coming from spin-orbit coupling ($H_{g,e}^{SO}$) and Jahn-Teller interaction($H_{g,e}^{JT}$). The total Hamiltonian of the electron system can be described by considering the interaction terms from strain (H^{strain}) and magnetic fields (Zeeman terms $H_{g,e}^{Z,L}, H_{g,e}^{Z,S}$), thus giving us a final Hamiltonian given by:

$$H_{g,e} = H_{g,e}^0 + H_{g,e}^{SO} + H_{g,e}^{JT} + H_{g,e}^{Z,L} + H_{g,e}^{Z,S} + H^{strain} \tag{3.21}$$

Which takes into account all the relevant terms together with the non-perturbed term $H_{g,e}^0$. Usually in low strain environments the strain Hamiltonian is negligible, in emitters like nanodiamonds, which are naturally highly strained, it cannot be neglected.

Spin-orbit coupling

This term arises from the relativistic interaction of a single electron with its own motion inside the potential generated by the nucleus. The interaction is in the form:

$$H^{SO} = \frac{\hbar}{4c^2 m}(\widehat{\nabla} V \times \hat{p}) \cdot \frac{\hat{S}}{\hbar} \tag{3.22}$$

where $V = e\varphi$ is the potential energy of the electron in the magnetic field created by the nucleus, m is the mass of the electron and $\hat{p}$ is the momentum of the electron. The spin operator $\hat{S}$ is expressed in terms of Pauli matrices for $S = \frac{1}{2}$:

One eventually finds that $\widehat{\nabla} V \times \hat{p}$ can be described in terms of the orbital angular momentum and that the x,y components of the orbital angular momentum operator vanish leading to the final form of the spin-orbit Hamiltonian:

$$H_{SO} = -\frac{\lambda_{g,e}}{2} \hat{L}_z \hat{S}_z \tag{3.23}$$

The application of the H_{SO} perturbation allows to find two two-fold degenerate eigenvalues which are also schematized in fig. 3.12.

$$+\lambda \longrightarrow \begin{cases} e_+ \uparrow\rangle = \frac{1}{\sqrt{2}}\left(|e_x \uparrow\rangle + i|e_y \uparrow\rangle\right) \\ |e_- \downarrow\rangle = \frac{1}{\sqrt{2}}\left(|e_x \downarrow\rangle - i|e_y \downarrow\rangle\right) \end{cases} \tag{3.24}$$
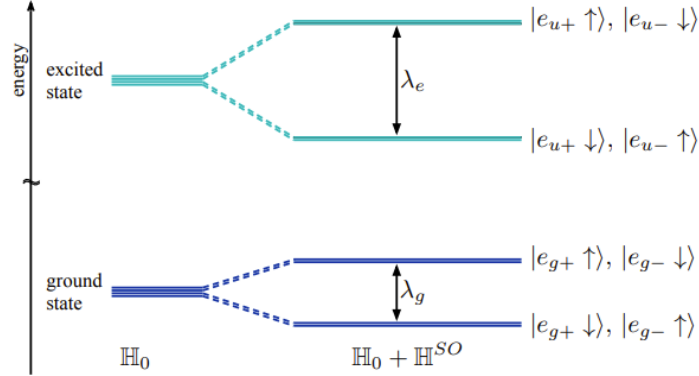
Figure 3.12: Energy separation of the sublevels due to spin-orbit coupling. The fourfold degeneracy of the ground and excited states is reduced to a twofold degeneracy.

$$-\lambda \longrightarrow \begin{cases} |e_+ \downarrow\rangle = \frac{1}{\sqrt{2}}\left(|e_x \downarrow\rangle + i\,|e_y \downarrow\rangle\right) \\ |e_- \uparrow\rangle = \frac{1}{\sqrt{2}}\left(|e_x \uparrow\rangle - i\,|e_y \uparrow\rangle\right) \end{cases} \tag{3.25}$$

Jahn-Teller interaction

The spin-orbit interaction discussed in the previous section partially lifts the degeneracy between the states composing the ground and excited state of the unperturbed Hamiltonian. Another intrinsic interaction acting on the electrons of the SiV center is the Jahn-Teller interaction.

The JT effect comes from the coupling of electronic states with vibration modes of the nuclear configuration, the interaction causes spontaneous symmetry breaking following the unstable spatial distribution of the electronic states.

Without going to much into detail of the nuclear dynamics of the system, the discussion will be based on the main results of works from literature [32, 33].

Systems which exhibit JT coupling are usually treated by employing the Born-Oppenheimer or adiabatic approximation: the electrons are considered to follow the motion of the nuclei adiabatically by virtue of their considerably smaller mass.

Therefore the Born-Oppenheimer approximation assumes that the full state function can be expressed as the product of electronic and nuclear wave function. The nuclei generate an effective potential, which can be called the adiabatic potential energy surface. In which the electrons move.

The Jahn-Teller effect couples the electrons and the modes of the nuclei as follows:

$$
H^{JT} = \frac{1}{2} K \left(Q_x^2 + Q_y^2 \right) + F \begin{bmatrix} Q_x & Q_y \\ Q_y & -Q_x \end{bmatrix} + G \begin{bmatrix} \left(Q_x^2 - Q_y^2 \right) & 2 Q_x Q_y \\ 2 Q_x Q_y & -\left(Q_x^2 - Q_y^2 \right) \end{bmatrix}
\tag{3.26}
$$

Here K is an elastic force constant, F the linear vibronic coupling coefficient and G the quadratic coefficient and $Q_{x,y}$ are the normal coordinates of the vibration modes of the nuclei. By introducing the polar coordinates $\rho = \sqrt{Q_x^2 + Q_y^2}$ and $\phi = arctan \left(\frac{Q_y}{Q_x} \right)$ one obtains:

$$
E\left(\rho, \phi \right) = \frac{1}{2} K \rho^2 \pm \rho \left[F^2 + G^2 \rho^2 + 2FG\rho \cos \left(3\phi \right) \right]^{\frac{1}{2}}
\tag{3.27}
$$

Usually the quadratic term G can be considered negligible, while the elastic term K is a global shift in energy for all energy states,therefore this Hamiltonian applied to the ground and excited states gives the following eigenvalues:

$$
+\Upsilon \longrightarrow \left\{ \begin{array}{l} \left| \cos \left(\frac{\phi}{2} \right) e_x + sin \left(\frac{\phi}{2} \right) e_y \right\rangle \left| \uparrow \right\rangle \\ \left| \cos \left(\frac{\phi}{2} \right) e_x + sin \left(\frac{\phi}{2} \right) e_y \right\rangle \left| \downarrow \right\rangle \end{array} \right.
\tag{3.28}
$$

$$
-\Upsilon \longrightarrow \left\{ \begin{array}{l} \left| \cos \left(\frac{\phi}{2} \right) e_x - sin \left(\frac{\phi}{2} \right) e_y \right\rangle \left| \uparrow \right\rangle \\ \left| \cos \left(\frac{\phi}{2} \right) e_x - sin \left(\frac{\phi}{2} \right) e_y \right\rangle \left| \downarrow \right\rangle \end{array} \right.
\tag{3.29}
$$

JT effect and spin-orbit interaction

The sum of the two components of the Hamiltonian gives rise to the fine structure observed at low temperature in the emission spectrum. With an overall ground and excited state splitting given by:

$$
\Delta E_{g,e} = \sqrt{\lambda_{g,e}^2 + 4\Upsilon_{g,e}^2}
\tag{3.30}
$$

Expressed in terms of the eigenvalues of the two interactions, as shown in the previous sections.
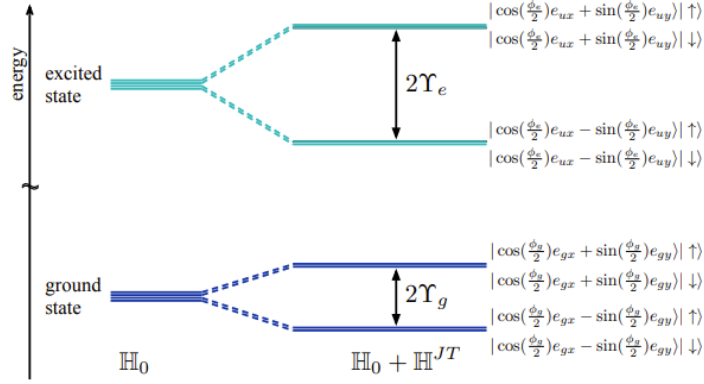
Figure 3.13: Analogously to the spin-orbit case the Jahn-Teller effect reduces the four-fold degeneracy to a two-fold degeneracy both in excited and ground states.

Strain fields

While the previous sections described intrinsic terms of the Hamiltonian of the SiV center, the effect of strain fields is sample dependent and can vary noticeably from environments with low crystal strain like monocrystalline bulk diamond to extremely strained materials like nanodiamonds. Strain can also be applied externally for specific purposes, for example the application of uniaxial stress is a technique widely employed in the determination of the symmetry of defects[2].

Strain can act on SiV centers in two ways. When considering an ensemble of SiV centers inside a diamond lattice there is, in principle, no constrain on the orientation of these defects which would have equivalent electronic configurations, thus one could define an orientational degeneracy between the different sub-ensembles containing SiV centers with the various possible orientations. When the crystal is under a strain field these ensembles are affected differently and the degeneracy is lifted [34].

$$
H_\pm^{\text{strain}} = \begin{bmatrix} 0 & 0 & -(\alpha + i\beta) & 0 \\ 0 & 0 & 0 & -(\alpha + i\beta) \\ -(\alpha - i\beta) & 0 & 0 & 0 \\ 0 & -(\alpha - i\beta) & 0 & 0 \end{bmatrix} \tag{3.31}
$$

When considering single SiV centers the strain field can also lift the orbital

degeneracy. Without going into too much detail when one applies the strain
Hamiltonian to the states in the spin-orbit basis described in the previous
section there is once again a reduction of the initial four-fold degeneracy to
a two-fold degeneracy.
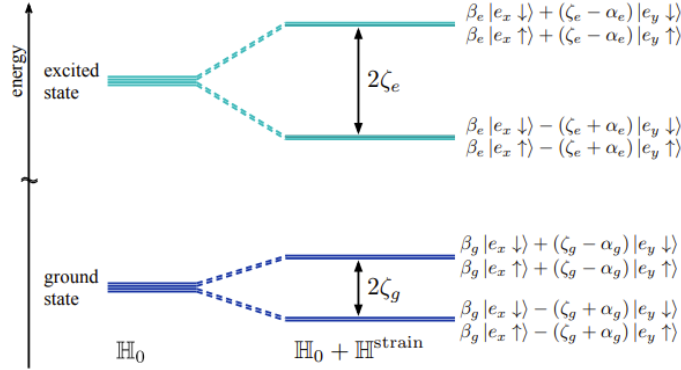
Figure 3.14: Energy level splitting due to the strain fields in the material.
Again the degeneracy of the energy levels is reduced as in the previous cases.

$$+\zeta \rightarrow \begin{cases} \frac{1}{\zeta - \alpha} [\beta \, |e_x \downarrow\rangle + (\zeta - \alpha) \, |e_y \downarrow\rangle] = |u_+ \downarrow\rangle \\ \frac{1}{\zeta - \alpha} [\beta \, |e_x \uparrow\rangle + (\zeta - \alpha) \, |e_y \uparrow\rangle] = |u_+ \uparrow\rangle \end{cases} \qquad (3.32)$$

$$-\zeta \rightarrow \begin{cases} -\frac{1}{\zeta + \alpha} [\beta \, |e_x \downarrow\rangle - (\zeta + \alpha) \, |e_y \downarrow\rangle] = |u_- \downarrow\rangle \\ -\frac{1}{\zeta + \alpha} [\beta \, |e_x \uparrow\rangle - (\zeta + \alpha) \, |e_y \uparrow\rangle] = |u_- \uparrow\rangle \end{cases} \qquad (3.33)$$

The optical transitions not only split but also shift in frequency due to the
applied strain. Analogously to the NV case strain and electric fields affect
the defect in the same way, one could therefore use electric fields to tune the
transition frequencies of selected defects, for more details on this aspect one
can find a rich variety of works in literature [35–37].

In strongly stressed materials like nanodiamonds the strain field becomes
more relevant than spin-orbit interaction, and lead to shits in the transitions
which are different in the ground and excited states and the intensity of the
optical transitions also are affected by the strain effects as shown in fig. 3.15.
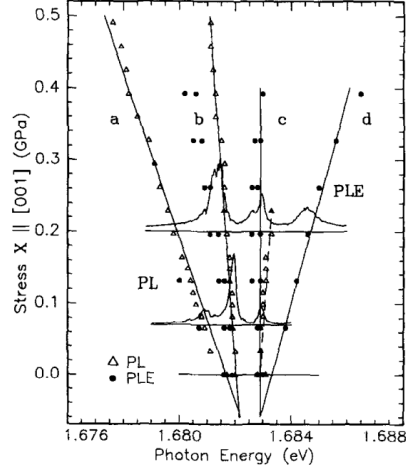
Figure 3.15: Behaviour of the PL fine structure observed at cryogenic temperatures under different stress values. Reproduced from [38]

Magnetic fields – Zeeman effect

Of the interactions observed in previous sections none lifts the magnetic sublevel degeneracy. The SiV center has two components to the magnetic moment, one comes from the orbital angular momentum L and the other from the spin S. Thus the perturbation Hamiltonian related to interaction with magnetic fields is in the form:

$$H_{g,e}^{Z} = H_{g,e}^{Z,L} + H_{g,e}^{Z,S} = \gamma_L \hat{L} \cdot \hat{B} + \gamma_S \hat{S} \cdot \hat{B} = q\gamma_L L_z B_z + \gamma_S \hat{S} \cdot \hat{B} \quad (3.34)$$

With $\gamma_L = \frac{\mu_B}{\hbar}$, $\gamma_S = \frac{2\mu_B}{\hbar}$ are the orbital and electron gyromagnetic ratios respectively, μ_B is again the Bohr magneton, $\hat{B} = (B_x, B_y, B_z)$ is the magnetic field expressed in terms of the coordinates previously introduced for the SiV center, $\hat{S} = \frac{\hbar}{2}(\sigma_x, \sigma_y, \sigma_z)$ is the spin operator expressed in terms of the Pauli matrices and $\hat{L} = (0, 0, L_z)$, as observed in the spin-orbit section. The factor q is a quenching factor that is introduced by the Jahn-Teller effect.

If the magnetic field is oriented along the z axis, which corresponds to the main axis of symmetry of the defect, there is no spin mixing. Otherwise the off-diagonal x,y terms of the magnetic field cause the mixing of the $|\uparrow\rangle, |\downarrow\rangle$ states.

The eigenvalues of this Hamiltonian term are:

$$E^Z = \pm q\gamma_L B_z \pm \gamma_S\sqrt{B_x^2 + B_y^2 + B_z^2} \tag{3.35}$$

Introducing a split in all the magnetic sublevels linearly dependent on B. When the Zeeman effect is taken into account together with the SO and JT interaction the behaviour of the fine structure transitions is shown in fig. 3.16.
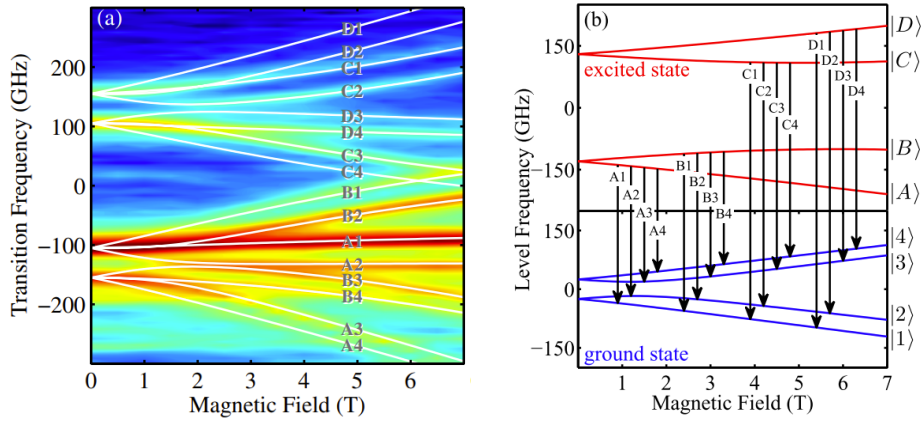
Figure 3.16: Panel (a): Spectral fine structure splitting of a SiV ensemble (contour plot, color coding indicates peak intensity in logarithmic a.u.) vs applied magnetic field [in the (001) direction]. The white lines represent transitions calculated by adding spin-orbit, JT effect and Zeeman effect contributions. Panel (b): Calculated splitting of electronic levels considering spin-orbit, JT effect and Zeeman effect contributions, the black arrows represent all possible transitions and correspond to the transitions observed in panel (a). Reproduced from [21].

Bibliography

[1] CD Clark and CA Norris. Photoluminescence associated with the 1.673, 1.944 and 2.498 ev centres in diamond. *Journal of Physics C: Solid State Physics*, 4(14):2223, 1971.

[2] Gordon Davies and MF Hamer. Optical studies of the 1.945 ev vibronic band in diamond. *Proceedings of the Royal Society of London. A. Mathematical and Physical Sciences*, 348(1653):285–298, 1976.

[3] A Gruber, A Drabenstedt, C Tietz, L Fleury, J Wrachtrup, and C von Borczyskowski. Scanning confocal optical microscopy and magnetic resonance on single defect centers. *Science*, 276(5321):2012–2014, 1997.

[4] Gergő Thiering and Adam Gali. Ab initio magneto-optical spectrum of group-iv vacancy color centers in diamond. *Physical Review X*, 8(2):021063, 2018.

[5] Solveig Felton, AM Edmonds, Mark E Newton, PM Martineau, D Fisher, and DJ Twitchen. Electron paramagnetic resonance studies of the neutral nitrogen vacancy in diamond. *Physical Review B*, 77(8):081201, 2008.

[6] Adam Gali. Theory of the neutral nitrogen-vacancy center in diamond and its application to the realization of a qubit. *Physical Review B*, 79(23):235210, 2009.

[7] JP Goss, R Jones, SJ Breuer, PR Briddon, and Sven Öberg. The twelve-line 1.682 ev luminescence center in diamond and the vacancy-silicon complex. *Physical review letters*, 77(14):3041, 1996.

[8] J HN Loubser and JA Van Wyk. Optical spin-polarisation in a triplet state in irradiated and annealed type 1b diamonds. *DIN-Mitt.;(United Kingdom)*, 1977.

[9] Romana Schirhagl, Kevin Chang, Michael Loretz, and Christian L Degen. Nitrogen-vacancy centers in diamond: nanoscale sensors for physics and biology. *Annual review of physical chemistry*, 65:83–105, 2014.

[10] Edward U Condon. Nuclear motions associated with electron transitions in diatomic molecules. *Physical Review*, 32(6):858, 1928.

[11] SW Brown and Stephen C Rand. Site symmetry analysis of the 738 nm defect in diamond. *Journal of applied physics*, 78(6):4069–4075, 1995.

[12] Elke Neu, David Steinmetz, Janine Riedrich-Möller, Stefan Gsell, Martin Fischer, Matthias Schreck, and Christoph Becher. Single photon emission from silicon-vacancy colour centres in chemical vapour deposition nano-diamonds on iridium. *New Journal of Physics*, 13(2):025012, 2011.

[13] Elke Neu, Martin Fischer, Stefan Gsell, Matthias Schreck, and Christoph Becher. Fluorescence and polarization spectroscopy of single silicon vacancy centers in heteroepitaxial nanodiamonds on iridium. *Physical Review B*, 84(20):205211, 2011.

[14] Elke Neu, Carsten Arend, E Gross, F Guldner, Christian Hepp, David Steinmetz, Elisabeth Zscherpel, Slimane Ghodbane, Hadwig Sternschulte, Doris Steinmüller-Nethl, et al. Narrowband fluorescent nanodiamonds produced from chemical vapor deposition films. *Applied Physics Letters*, 98(24), 2011.

[15] Stefan Häußler, Gergő Thiering, Andreas Dietrich, Niklas Waasem, Tokuyuki Teraji, Junichi Isoya, Takayuki Iwasaki, Mutsuko Hatano, Fedor Jelezko, Adam Gali, et al. Photoluminescence excitation spectroscopy of siv- and gev- color center in diamond. *New Journal of Physics*, 19(6):063036, 2017.

[16] Gordon Davies. The jahn-teller effect and vibronic coupling at deep levels in diamond. *Reports on Progress in Physics*, 44(7):787, 1981.

[17] AA Gorokhovsky, AV Turukhin, RR Alfano, and W Phillips. Photoluminescence vibrational structure of si center in chemical-vapor deposited diamond. *Applied physics letters*, 66(1):43–45, 1995.

[18] Alan T Collins, Lars Allers, Christopher JH Wort, and Geoffrey A Scarsbrook. The annealing of radiation damage in de beers colourless cvd diamond. *Diamond and Related Materials*, 3(4-6):932–935, 1994.

[19] Konstantin Iakoubovskii and GJ Adriaenssens. Optical detection of defect centers in cvd diamond. *Diamond and related materials*, 9(7):1349–1356, 2000.

[20] Jeronimo R Maze, Adam Gali, Emre Togan, Yiwen Chu, Alexei Trifonov, Efthimios Kaxiras, and Mikhail D Lukin. Properties of nitrogen-vacancy centers in diamond: the group theoretic approach. *New Journal of Physics*, 13(2):025025, 2011.

[21] Christian Hepp, Tina Müller, Victor Waselowski, Jonas N Becker, Benjamin Pingault, Hadwig Sternschulte, Doris Steinmüller-Nethl, Adam Gali, Jeronimo R Maze, Mete Atatüre, et al. Electronic structure of the silicon vacancy color center in diamond. *Physical Review Letters*, 112(3):036405, 2014.

[22] Ulrika FS D'Haenens-Johansson, AM Edmonds, BL Green, Mark E Newton, G Davies, PM Martineau, RUA Khan, and DJ Twitchen. Optical properties of the neutral silicon split-vacancy center in diamond. *Physical Review B*, 84(24):245208, 2011.

[23] Marcus W Doherty, Neil B Manson, Paul Delaney, Fedor Jelezko, Jörg Wrachtrup, and Lloyd CL Hollenberg. The nitrogen-vacancy colour centre in diamond. *Physics Reports*, 528(1):1–45, 2013.

[24] S Felton, AM Edmonds, Mark E Newton, PM Martineau, D Fisher, DJ Twitchen, and JM Baker. Hyperfine interaction in the ground state of the negatively charged nitrogen vacancy center in diamond. *Physical Review B*, 79(7):075203, 2009.

[25] NB Manson, JP Harrison, and MJ Sellars. Nitrogen-vacancy center in diamond: Model of the electronic structure and associated dynamics. *Physical Review B*, 74(10):104303, 2006.

[26] Abdelghani Laraoui, Jonathan S Hodges, and Carlos A Meriles. Nitrogen-vacancy-assisted magnetometry of paramagnetic centers in an individual diamond nanocrystal. *Nano letters*, 12(7):3477–3482, 2012.

[27] A Lenef and SC Rand. Electronic structure of the n-v center in diamond: Theory. *Physical Review B*, 53(20):13441, 1996.

[28] Philipp Neumann, Ingmar Jakobi, Florian Dolde, Christian Burk, Rolf Reuter, Gerald Waldherr, Jan Honert, Thomas Wolf, Andreas Brunner, Jeong Hyun Shim, et al. High-precision nanoscale temperature sensing using single defects in diamond. *Nano letters*, 13(6):2738–2742, 2013.

[29] Victor M Acosta, Erik Bauch, Micah P Ledbetter, Amir Waxman, L-S Bouchard, and Dmitry Budker. Temperature dependence of the nitrogen-vacancy magnetic resonance in diamond. *Physical review letters*, 104(7):070801, 2010.

[30] Marcus W Doherty, Viktor V Struzhkin, David A Simpson, Liam P McGuinness, Yufei Meng, Alastair Stacey, Timothy J Karle, Russell J Hemley, Neil B Manson, Lloyd CL Hollenberg, et al. Electronic properties and metrology applications of the diamond nv- center under pressure. *Physical review letters*, 112(4):047601, 2014.

[31] Elke Neu, Christian Hepp, Michael Hauschild, Stefan Gsell, Martin Fischer, Hadwig Sternschulte, Doris Steinmüller-Nethl, Matthias Schreck, and Christoph Becher. Low-temperature investigations of single silicon vacancy colour centres in diamond. *New Journal of Physics*, 15(4):043005, 2013.

[32] Mary CM O'Brien and CC Chancey. The jahn–teller effect: An introduction and current review. *American Journal of Physics*, 61(8):688–697, 1993.

[33] Patrick WM Jacobs. *Group theory with applications in chemical physics.* Cambridge University Press, 2005.

[34] AA Kaplyanskii. Noncubic centers in cubic crystals and their piezospectroscopic investigation. *Optics and Spectroscopy*, 16:329, 1964.

[35] Jeronimo Maze Rios. *Quantum manipulation of nitrogen-vacancy centers in diamond: from basic properties to applications.* Harvard University, 2010.

[36] LC Bassett, FJ Heremans, CG Yale, BB Buckley, and DD Awschalom. Electrical tuning of single nitrogen-vacancy center optical transitions enhanced by photoinduced fields. *Physical review letters*, 107(26):266403, 2011.

[37] Thomas Müller, I Aharonovich, Laurent Lombez, Yury Alaverdyan, AN Vamivakas, Stefania Castelletto, Fedor Jelezko, Joerg Wrachtrup, Steven Prawer, and Mete Atatüre. Wide-range electrical tunability of single-photon emission from chromium-based colour centres in diamond. *New Journal of Physics*, 13(7):075001, 2011.

[38] H Sternschulte, K Thonke, J Gerster, W Limmer, R Sauer, J Spitzer, and PC Muenzinger. Uniaxial stress and zeeman splitting of the 1.681 ev optical center in a homoepitaxial cvd diamond film. *Diamond and Related Materials*, 4(10):1189–1192, 1995.

Chapter 4

Synthesis of Fluorescent Nanodiamonds: One-Step Process by Pulsed Laser Ablation of Graphite in Liquid Nitrogen

As already said in chapter 2, fluorescent nanodiamonds containing NV centers can be obtained by Pulsed Laser Ablation in different media (e.g. liquid nitrogen, nitrogen rich atmosphere) [1].

From previous works [1], the most efficient setup is the ablation of graphite in liquid nitrogen, which gives nano powders which much higher photoluminescence intensity.

In our laboratory we developed an ad-hoc apparatus for PLA of graphite in liquid nitrogen, which is described in the next section of this chapter. The main focus for this apparatus is the possibility of operating continuously over long times, allowing the production of relatively large amounts of nanopowders.

In the following sections I will cover the procedures employed for the removal of graphite residues and the results of the characterisation of the resulting nanopowders.

4.1   Apparatus

The apparatus we employed for the production of the nanodiamonds is schematised in figure 4.1.
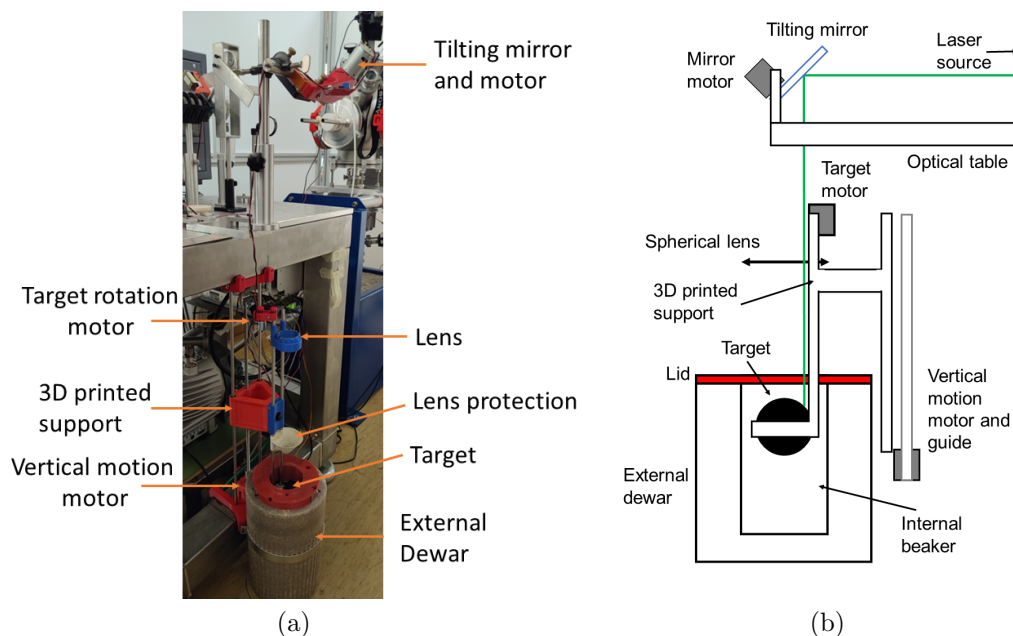
Figure 4.1: Panel (a): photo of the experimental apparatus. Panel (b): schematic of the experimental apparatus.

Starting from the bottom, in fig4.1 one can see the insulated container, where the ablation procedure takes place. Between the internal beaker and the external polystyrene container there is a space that can be filled with more liquid nitrogen in order to reduce the evaporation of nitrogen from the main container; this is shown in more detail in figure 4.3.

Moving upward on the image one can see the structure that holds the lens and the target. The structure is connected (blue and red assembly in the middle) to the steel supports anchored to the optical table. The vertical motion of the system is provided by a motor connected to the base of the supports, which rotates a screw that governs the position of the main structure with respect to the supports. This configuration keeps the distance between the lens and the target constant (in the limit given by the degradation of the

target itself) during the operations of the system.

In the center one can see a white hollow cone, this is just a guard to shield (although not completely) the lens from possible splashing from the ablation procedure. The presence of this guard is more important when working with water.

At the top of the steel supports the blue lens holder can be adjusted to maintain the correct distance between the lens and the target. On top of the left support the DC motor that provides the rotation of the target.

In figure 4.2 one can see the detail of the mechanism that transmits the rotational movement to the target. The motor rotates a shaft inside the steel support. The bent end of the axle connects to a 3D-printed element in a crankshaft configuration. This transmission element imparts a step to the target for each rotation of the axle.

At the top of the image, the mirror and its corresponding motor are located on top of a steel support connected to the the optical table. The motor periodically tilts the mirror, this tilt moves the laser beam along the axis of the target, allowing the use of most of the target surface during operation.

(a)   (b)

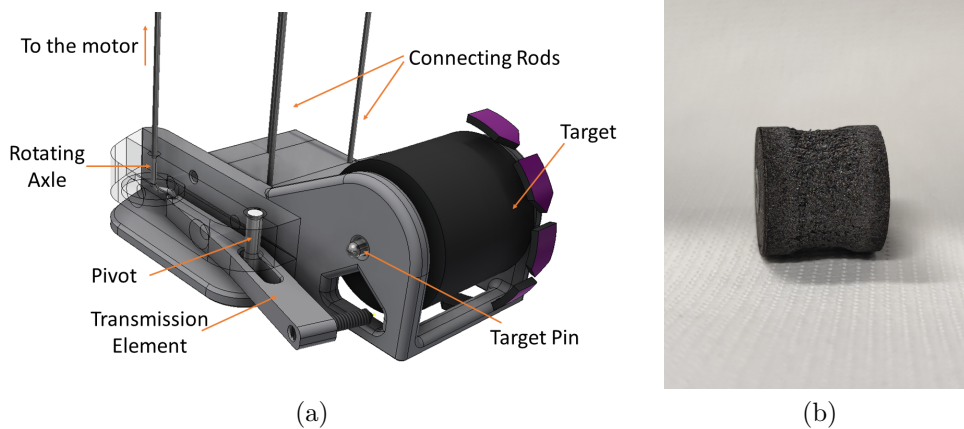Figure 4.2: (a)Detail of the component that transmits the rotational motion to the target, as shown in fig. 4.1. The support element keeping the assembly in place is left transparent for clarity. The purple arrows represent the step motion imparted to the target by the apparatus. (b) Photo of the graphite target after ablation.

The mirror and the lens are aligned in such a way as to focus the laser

beam in a position where the laser has 45° incidence with respect to the surface of the cylinder. This configuration reduces the interaction between the laser and the expanding plume with respect to the case of the laser impinging directly on top of the target, while avoiding excessive loss of fluence that would happen at higher incidence angles.
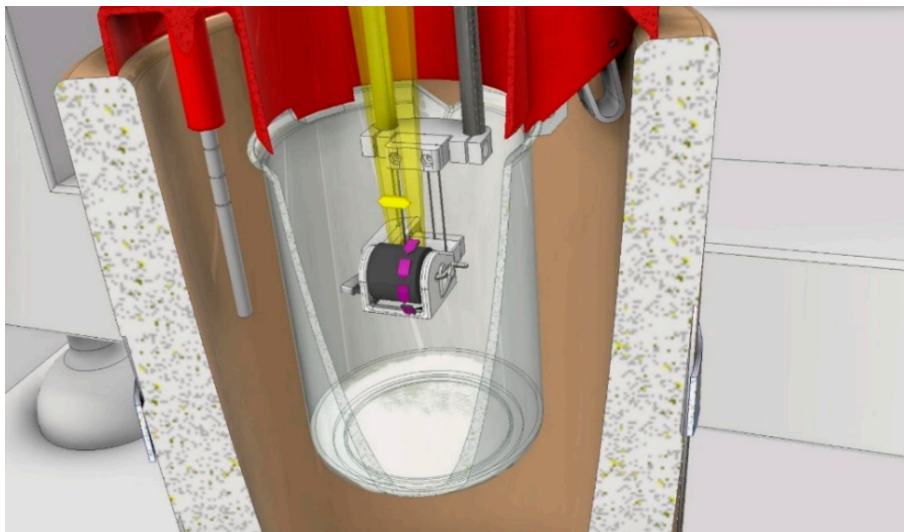
Figure 4.3: 3D rendering of the apparatus showing in detail the interior of the container. Reproduced from [2].

As can be seen in the fig 4.3 the target is attached to a 3D printed support suspended from the main apparatus by thin metal wires. The thin wires have lower thermal conductivity than the larger rods forming the apparatus and thus transfer less heat to the liquid nitrogen, reducing the rate of evaporation. The vertical shaft which transfers the motion from the motor on top of the apparatus to the target is also very thin for the same reason.

The beaker is suspended from the lid and the kept in place by 3D printed locks. The lid itself is connected to the polystyrene container and fixed in place by a spring mechanism. The connections between the lid and the beaker are not airtight to avoid excessive pressure increase.

When operating the apparatus, both the containers are filled with liquid nitrogen up to the same level, just below the beak of the beaker in order to maximise the insulation of the internal container while avoiding contamination of the inner container from the insulating layer.

To avoid excessive thermal stresses on the internal container, during the first filling the liquid nitrogen is poured relatively slowly, keeping the levels on the inner and outer containers to similar heights. The beaker is filled from the central opening, while the Dewar is filled from a hole in the lid. Subsequent refills are performed with the system already in thermal equilibrium and do not require the same attention.

Once the system has thermalized, the target can be lowered in the liquid nitrogen and the ablation process can take place. To avoid formation of ice that could impair the functioning of the apparatus the target has to remain submerged at all times.

During operation the strong radiation of the laser induces strong evaporation of the nitrogen inside the beaker, the vertical motion of the setup is used to track the evaporating surface, keeping the target $5mm$ below the surface (considering the point of the target where the laser impinges on the graphite).

The details of the ablation process have already been discussed in chapter 2. For the present work the lens employed had 45 cm focal length, the laser fluence was kept at $\sim 40 - 50 J/cm^2$ as written in the previous chapter and each ablation procedure was conducted to perform at least ~ 80000 laser pulses.

4.2 Purification Procedure

The main advantage of long operation is the production of large batches of nanopowders. This allows to perform more intense cleaning procedures, in line with industrial requirements for scalability, without the risk of losing a large portion of the prepared samples.

We employed two procedures:

- Oxidative procedure

- Chemical procedure

4.2.1 Oxidative Procedure

The first procedure employed consists in selectively oxidise graphitic and amorphous sp^2 carbon components, without attacking the diamond phase.

(a)

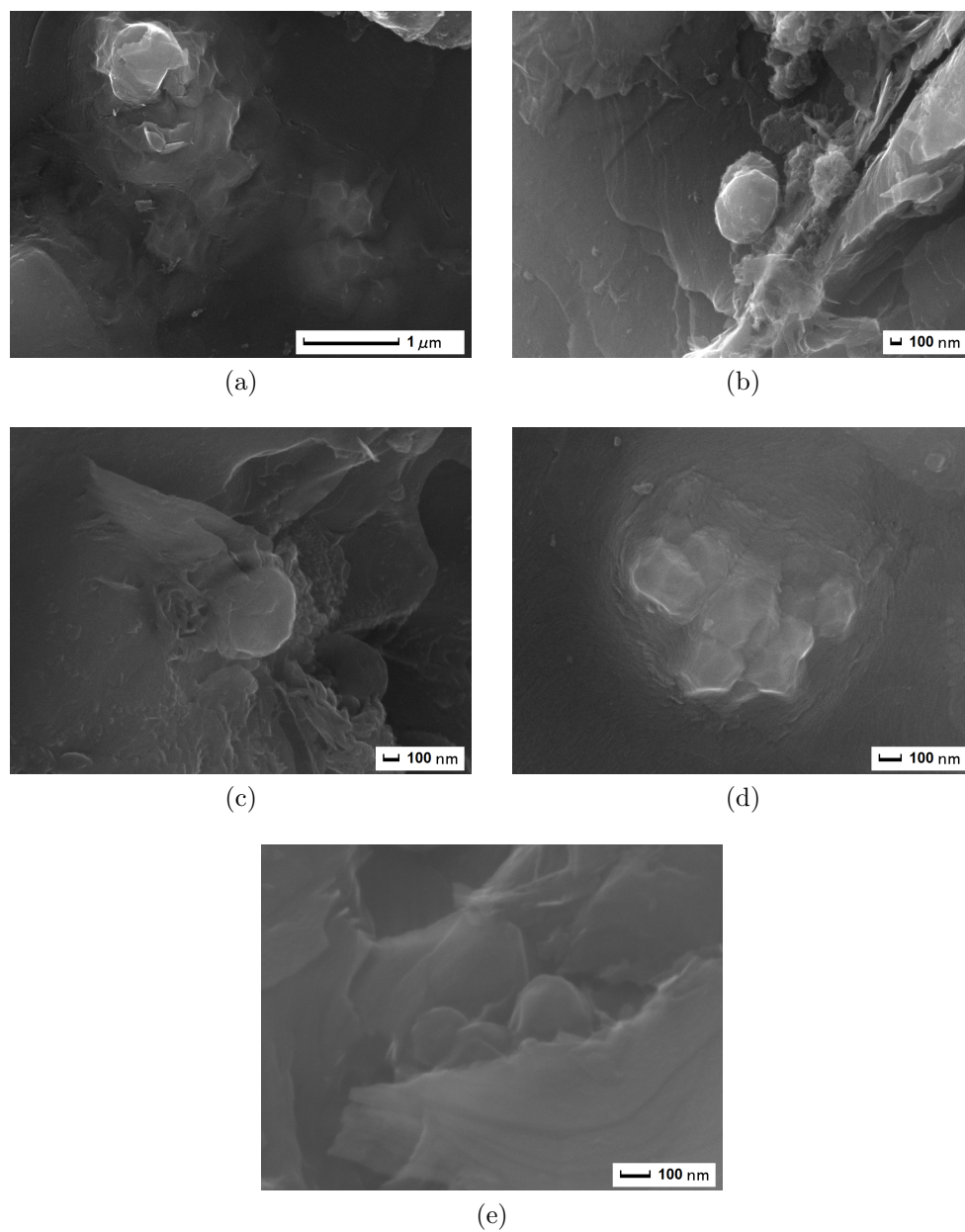(b)

(c)

(d)

(e)

Figure 4.4: SEM micrographs the raw powders after re-dispersion in distilled water. Panels (a,b) belong to the first sample produced and panels (c-e) belong to the second sample of nanopowders, produced under the same conditions. In particular panel (e) shows conglomerates embedded particularly deep in the surrounding graphite, revealed by the cracking of the substrate.

This is possible because in the temperature range $375 - 450°C$ the oxidation rates of sp^2 and sp^3 carbon are different, and in particular between $400-430°C$ sp^2 carbon oxidation is very efficient, while there is no or minimal loss of sp^3 carbon [3].

Therefore this treatment was performed at $425°C$ in a tube furnace (Carbolite CTF 12/65/550) initially for 5h and afterward for 72 h. The morphology of the material is evidently modified by the treatment as will be shown in the next images.

For the SEM characterisation of the samples, the powders are dispersed in isopropyl alcohol and a single drop is deposited on a silicon substrate.

The initial "as deposited" samples show the presence of smooth, slightly faceted, structures in the order of the hundreds on nm in diameter, comparable with previous works [1, 4], and associated with nanodiamond clusters.

These clusters appear to be fully embedded into the surrounding graphite matrix as can be seen in fig:4.4.

The powders are then subjected to a 5 h oxidation process. It is apparent from figure 4.5 that the particles observed previously are now more detached from the matrix and their surface appears less smooth and uniform, partially etched by the oxygen in the atmosphere.

Another feature that can be observed is the presence of "holes" in the matrix which are likely an indication of missing clusters (based on the typical dimension of the holes and clusters) that have completely detached from the surrounding matrix due to the oxidation of the binding sp^2 layers.

After the last oxidative step the surface of the samples is heavily modified. In figure 4.6 one can see that the clusters are completely detached from the matrix, forming a discontinuous structure. The oxidation removes material around and below the particles, which instead remain affected only on a superficial level. This further proves the presence of sp^3 carbon in the core of the particles, while the external layers of graphitic carbon are etched away.

Although this technique allows to remove the sp^2 carbon selectively, without introducing impurities of any kind, it is also extremely inefficient. While in principle the problem could be solved by increasing the oxidation times, it is not a good solution if the scalability of the process is considered.

Therefore this purely thermal process is unsuitable for the removal of large amounts of graphite, while it can still be considered a good option for the removal of smaller residues. In fact in Chapter 5 I will show the combined use of this technique and the chemical purification procedure described in the next section.

(a)   (b)

(c)   (d)

(e)   (f)
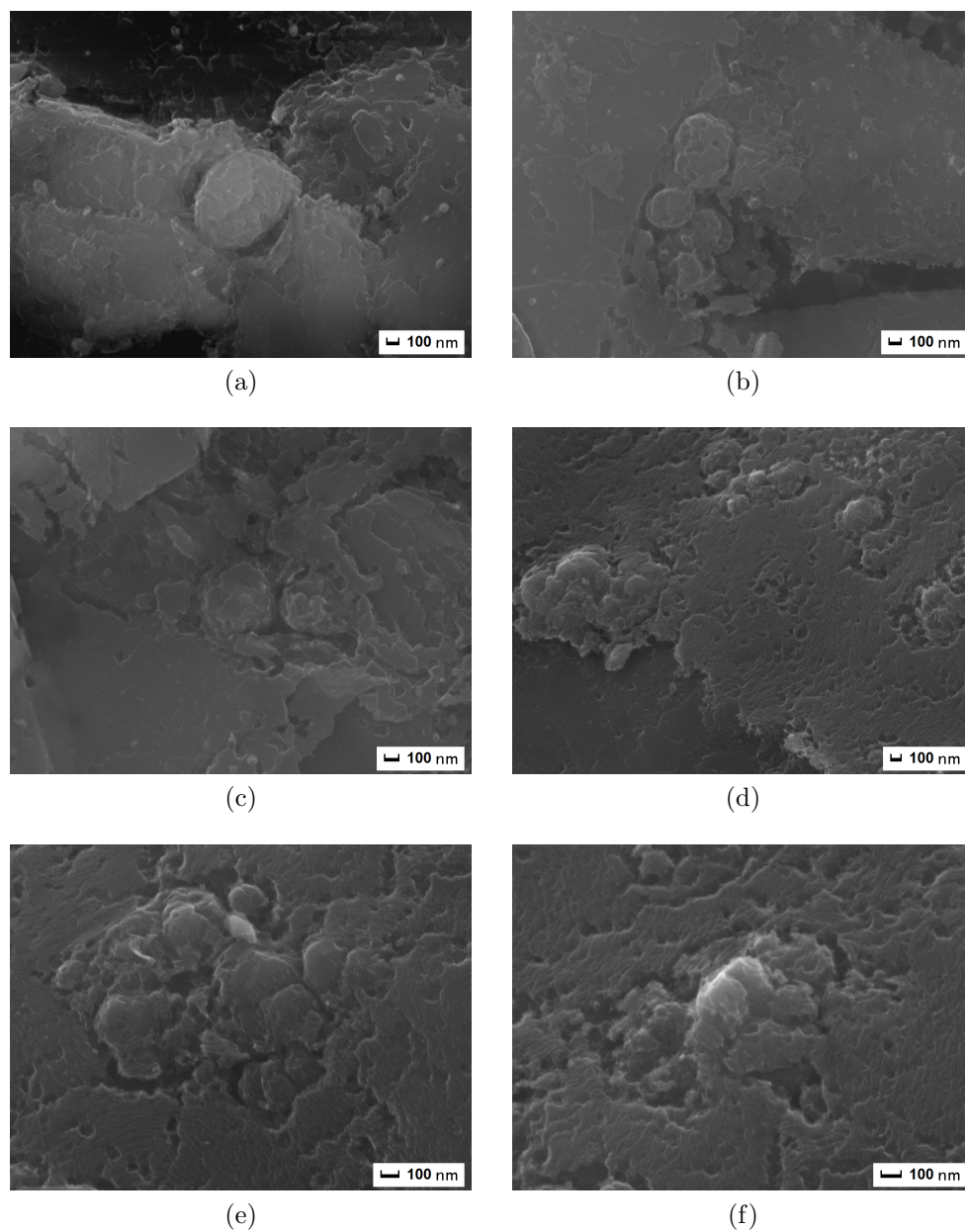
Figure 4.5: SEM micrographs of the powders after 5h oxidative treatment. Here two samples are shown, produced and treated under the same conditions. Panels (a-c) show the surface of the first sample, while panels (d-f) of the second one. Both exhibit partial erosion of the matrix surrounding the conglomerates.
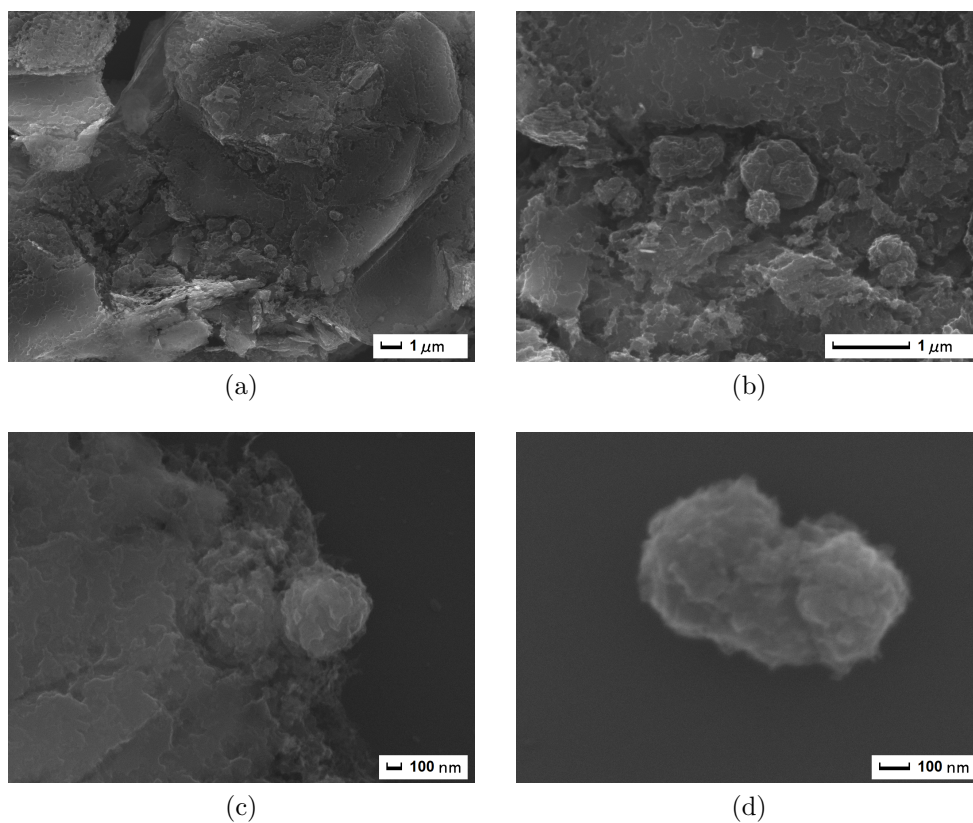
Figure 4.6: SEM micrographs of the powders after the full 77 h oxidation process

4.2.2 Chemical Purification Procedure

While thermal oxidation is a relatively clean procedure for the purification of nanodiamonds, it is too inefficient to remove graphitic carbon from raw powders, where the sp^2 carbon content makes up the majority of the material.

Considering industrial procedures used for other synthesis techniques, the employed a process was derived from techniques used for detonation nanodiamond purification. [5]

The powders are treated with sulphonitric solution (3 parts concentrated sulphuric acid 98% and 1 part concentrated nitric acid 60%) at a temperature of 190°C for 3 h under reflux. For approximately 100mg of raw powders 100ml of sulphonitric solution were employed.
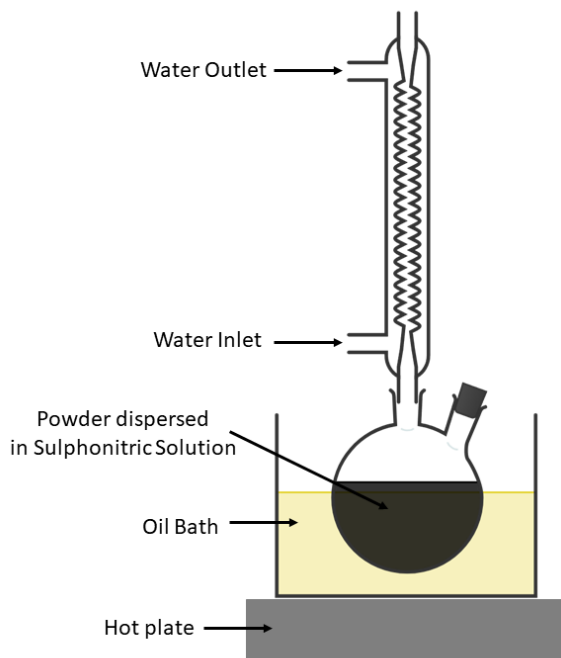
Figure 4.7: Scheme of the simple apparatus employed in the chemical treatment of the powders. As the top of the apparatus is loosely stopped to avoid excessive pressure build up, the procedure is performed under a fume hood.

The powders recovered directly from the internal beaker of the ablation apparatus are put into a flask connected to a condensation column. The sulphonitric solution is added to the system and the lateral neck of the flask is sealed. The top of the condensation column is loosely stopped to avoid excessive pressure increase inside the system. The flask is placed in the oil bath which allows to keep the temperature to exactly $190°C$.

During the procedure the suspension of the powder inside the acids goes from black to red, to light yellow color. After 3 hours the heating is turned off and the system is allowed to cool down overnight. We observe that when temperature goes below $150°C$ any sign of further reactions stops. At this point only the larger fragments (residues of large scale fragmentation of the target) of graphite appear visible inside the ampule.

Since the process is conducted with high stoichiometric abundance of acids and under reflux, the dispersion is at this point extremely acidic. There-

fore the next step is a neutralisation of the dispersion.

The dispersion is moved to a conical flask surrounded by an ice bath. Here concentrated (5 M) Sodium hydroxide solution is added drop by drop. The ice bath counteracts the strongly exothermic reaction between the acids and the base, avoiding overheating and possible boiling of the dispersion.

The pH of the dispersion is periodically checked by dropping a single drop of it on a universal indicator paper.

Near neutral pH there is the formation of salt crystals which deposit out of solution. These are re-dissolved by slow addition of distilled water, in order to add just enough to avoid formation of crystals. At the end the pH of the dispersion is checked again with a pH meter.

To recover the powder and remove the salts subsequent centrifugation steps are performed.

The concentration steps are performed by centrifugating the neutralised dispersion and removing the supernatant liquid. The vials are then filled again with the dispersion until all the liquid has been processed.

The remaining liquid is now nearly saturated with salt, which has to be removed in order to obtain pure dry powders.

Again the remaining dispersion inside the vials ($\sim 5ml$) is dispersed, this time with distilled water, to the maximum volume of $50ml$, reducing the concentration of salt by a factor of 10. The procedure is repeated 5 times, assuming that the main solute is sodium sulfate, after neutralisation the concentration can be considered to be $\sim 0.047g/ml$, therefore after 5 washings it can be estimated to be $\sim 4.7 \times 10^{-7}g/ml$. Only isolated traces of salts have been found during SEM measurements

The resulting powders are characterised by SEM imaging in figure 4.8.

The resulting morphology is extremely different from the powders treated only by thermal oxidation. The underlying graphitic matrix appears to have completely dissolved.

What can be observed are nanodiamonds agglomerated together with residual sheets of graphite and amorphous layers between the nanodiamonds themselves.

The yield of the chemical purification results to be $7 \pm 1\%$ in weight with respect to the initial ablation soot. This is in line with results from literature for laser ablation based techniques which report yields of $5-10\%$[6, 7]. Other techniques have yields of around 15% for HPHT [8], 10% for cavitation-assisted techniques [9] and 4–10% for detonation nanodiamonds[9, 10]

(a)

(b)

(c)
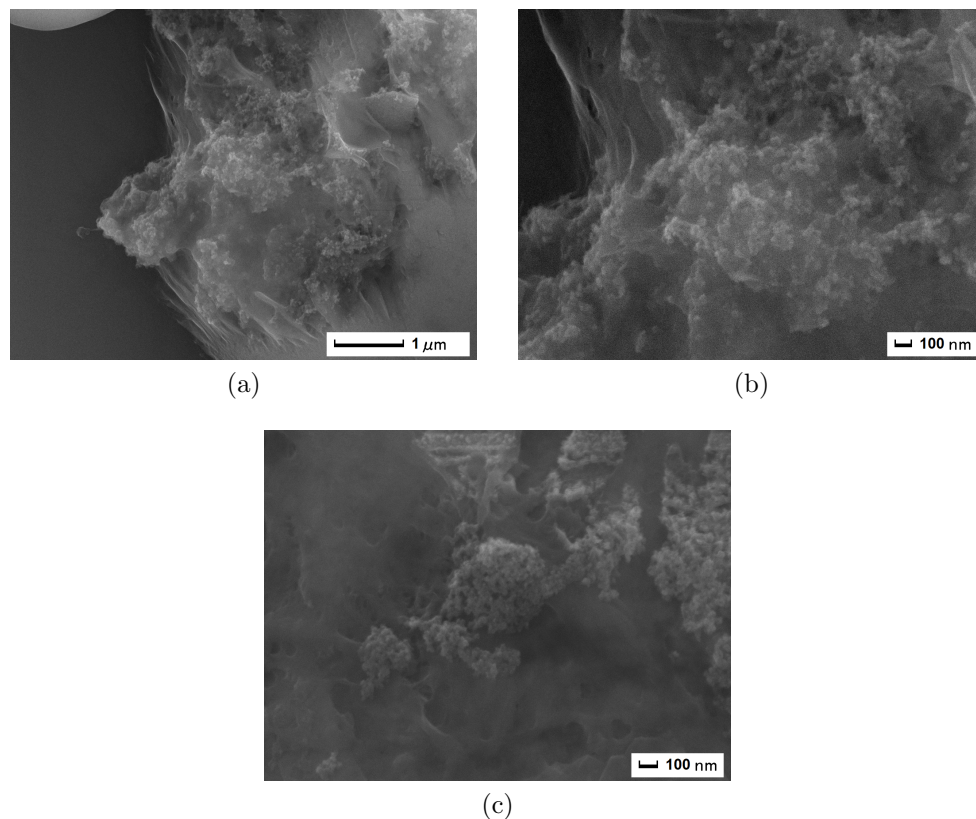
Figure 4.8: SEM micrographs of chemically purified nanodiamonds. Panels (a) and (b) show the same conglomerate partially enveloped by a residual salt impurity from the neutralisation process. Panel (c) shows a different conglomerate on top of a residue of graphite.

4.3   Optical Characterisation

The optical properties of the powders have been observed using a confocal microRaman Jobin–Yvon LabRam apparatus. When performing ODMR measurements the sample was fixed on an epoxy-glass sample holder equipped with a Hertzian RF antenna; the RF irradiation served as the ground $|g\rangle$ level pump to populate the $m_s = \pm 1$ sublevels in order to observe the spin dependent properties of the NV center photoluminescence [11].

The observation are performed under continuous laser excitation at 532 nm. The powders are deposited on quartz slides.

The observed photoluminescence show a broad emission in the red region of the spectrum as shown in figure 4.9, consistent with the emission recorded for NV centers in nanodiamond [12]. Additionally the spectra show a tail in the region with wavelength $> 700nm$ which is possibly due to residual graphitic layers on the surface of the nanodiamonds or between them in the conglomerates.

These features of the emission spectra are compatible with previous works [1, 4] even after chemical purification procedures.

In the spectra two sharp peaks can be observed in the region with $\lambda < 600nm$, these are the D and G Raman peaks of graphite, which are conspicuously absent in the samples that have undergone chemical purification or the full 77h thermal treatment.
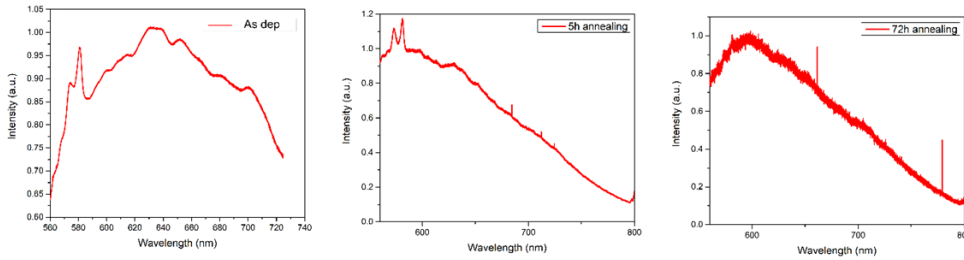
Figure 4.9: Representative spectra of the samples under different purification conditions. From left to right: raw samples, samples after 5 h oxidation in air and samples after 77 h oxidation in air; as published in [2].

The ODMR measurements performed on the powders are sensible only to the emission of the NV centers [11]. NV center fluorescence undergoes significant intensity changes when the centers are subjected to radiofrequency irradiation resonant with the energy separation of the ground state sublevels with $m_s = 0$ and $m_s = \pm 1$ of $2870MHz$[13], schematised in figure 4.10 panel (a). The microwave radiation sends the ground state from the $m_S = 0$ sublevel to the degenerate $m_S = \pm 1$ sublevels. The excitation of the $m_S = 0$ sublevel leads to emission of photoluminescence while the excitation of the degenerate sublevels has larger probability of non radiative recombination, leading to reduced photoluminescence intensity.

The experiments show (fig:4.10) a noticeable intensity dip at $\sim 2870MHz$, confirming the presence of NV centers. The width of the observed dip is compatible with previous observations [4] and is attributed to local strain fields present inside the nanodiamonds.
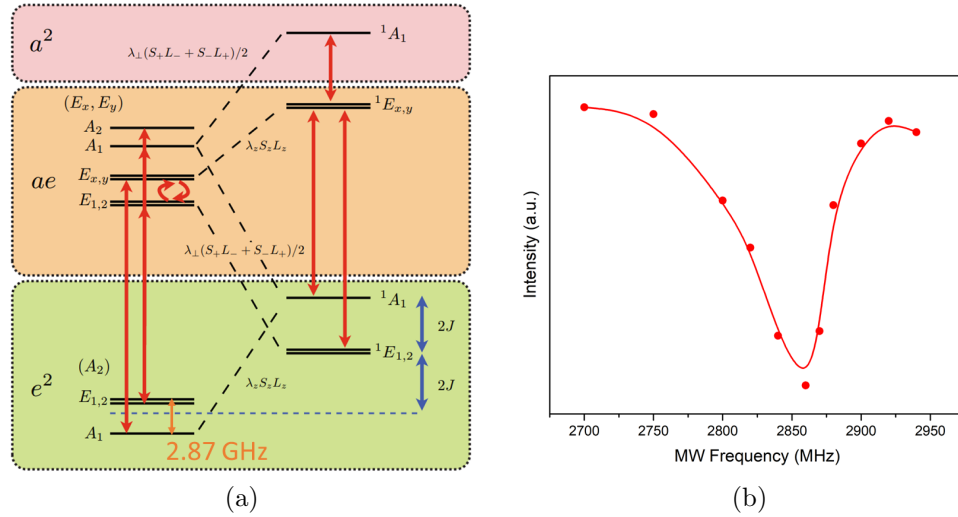
Figure 4.10: Panel a: energy level structure of the NV center in diamond with the different triplet (left) and singlet (right) states. The straight red arrows represent allowed optical transitions, the curved red arrows transitions due to spin-spin interaction and the dashed black lines non-radiative transitions. The blue arrows represent the energy separation between the singlet level and the orbital energy level of the ground state (blue dashed line), lastly the added orange arrow indicate the energy separation between the $m_S = 0$ and $m_S = \pm 1$ in absence of external magnetic fields. Reproduced from [14]. Panel b: representative ODMR spectrum of the chemically purified samples as published in [2]. The line is added as a guide to the eye.

The continuous operation of the ablation apparatus together with the efficient purification treatment using acids allows to produce significant amounts of clean nanodiamonds without significant impurities or graphitic residues, without compromising their optical and magneto-optical properties, with an efficiency comparable to other established techniques.

Bibliography

[1] Luca Basso, Nicola Bazzanella, Massimo Cazzanelli, and Antonio Miotello. On the route towards a facile fluorescent nanodiamonds laser-synthesis. *Carbon*, 153:148–155, 2019.

[2] Massimo Cazzanelli, Luca Basso, Claudio Cestari, Nicola Bazzanella, Enrico Moser, Michele Orlandi, Alessandro Piccoli, and Antonio Miotello. Fluorescent nanodiamonds synthesized in one-step by pulsed laser ablation of graphite in liquid-nitrogen. *C*, 7(2):49, 2021.

[3] Sebastian Osswald, Gleb Yushin, Vadym Mochalin, Sergei O Kucheyev, and Yury Gogotsi. Control of sp2/sp3 carbon ratio and surface chemistry of nanodiamond powders by selective oxidation in air. *Journal of the American Chemical Society*, 128(35):11635–11642, 2006.

[4] Luca Basso, F Gorrini, M Cazzanelli, N Bazzanella, A Bifone, and A Miotello. An all-optical single-step process for production of nanometric-sized fluorescent diamonds. *Nanoscale*, 10(12):5738–5744, 2018.

[5] Yuto Makino, Tomoaki Mahiko, Ming Liu, Akihiko Tsurui, Taro Yoshikawa, Shinji Nagamachi, Shigeru Tanaka, Kazuyuki Hokamoto, Masaaki Ashida, Masanori Fujiwara, et al. Straightforward synthesis of silicon vacancy (siv) center-containing single-digit nanometer nanodiamonds via detonation process. *Diamond and Related Materials*, 112:108248, 2021.

[6] L Yang, PW May, L Yin, JA Smith, and KN Rosser. Growth of diamond nanocrystals by pulsed laser ablation of graphite in liquid. *Diamond and related materials*, 16(4-7):725–729, 2007.

[7] J Xiao, P Liu, and GW Yang. Nanodiamonds from coal under ambient conditions. *Nanoscale*, 7(14):6114–6125, 2015.

[8] Jean-Paul Boudou, Patrick A Curmi, Fedor Jelezko, Joerg Wrachtrup, Pascal Aubert, Mohamed Sennour, Gopalakrischnan Balasubramanian, Rolf Reuter, Alain Thorel, and Eric Gaffet. High yield fabrication of fluorescent nanodiamonds. *Nanotechnology*, 20(23):235602, 2009.

[9] Jean-Charles Arnault. *Nanodiamonds: advanced material analysis, properties and applications*. William Andrew, 2017.

[10] Amanda M Schrand, Suzanne A Ciftan Hens, and Olga A Shenderova. Nanodiamond particles: properties and perspectives for bioapplications. *Critical reviews in solid state and materials sciences*, 34(1-2):18–74, 2009.

[11] Marcus W Doherty, Neil B Manson, Paul Delaney, Fedor Jelezko, Jörg Wrachtrup, and Lloyd CL Hollenberg. The nitrogen-vacancy colour centre in diamond. *Physics Reports*, 528(1):1–45, 2013.

[12] P-H Chung, E Perevedentseva, and C-L Cheng. The particle size-dependent photoluminescence of nanodiamonds. *Surface Science*, 601(18):3866–3870, 2007.

[13] Maria Simanovskaia, Kasper Jensen, Andrey Jarmola, Kurt Aulenbacher, Neil Manson, and Dmitry Budker. Sidebands in optically detected magnetic resonance signals of nitrogen vacancy centers in diamond. *Physical Review B*, 87(22):224106, 2013.

[14] Jeronimo R Maze, Adam Gali, Emre Togan, Yiwen Chu, Alexei Trifonov, Efthimios Kaxiras, and Mikhail D Lukin. Properties of nitrogen-vacancy centers in diamond: the group theoretic approach. *New Journal of Physics*, 13(2):025025, 2011.

Chapter 5

Synthesis of Fluorescent Nanodiamonds Mixed with Silicon Carbide Nanoparticles from Composite Precursors

In chapter 3, I showed the main advantages of Silicon Vacancy centers when compared with Nitrogen Vacancy centers, mainly the superior spectral purity of SiV centers as well as the possibility of working as single-photon sources. The synthesis of such NDs is an active field of research [1–3] thanks to their attractiveness for quantum applications.

In order to produce SiV centers in diamond by PLAL one has to find a way to introduce silicon into the system, in the same manner we employed liquid nitrogen as an ablation medium for the production of NV centers.

A possible avenue is to work with a precursor containing both Carbon and Silicon. We chose to work with composite targets composed of graphite and silicon carbide, sintered together at high temperature. The process employed in the production of the targets is described in section 5.1 and allows for good control of the composition of the material, in particular the Si concentration.

The precursors have been subjected to the ablation process in water and the resulting powders have been characterised via Raman Spectroscopy, Photoluminescence spectroscopy, SEM and EDXS characterisation, TEM and SAED characterisation.

Different silicon carbide (and consequently silicon) concentration targets have been prepared to investigate a concentration range which is typical of

other ND synthesis techniques[3–5].

5.1   Composite Precursors

The precursors have been prepared in the department of industrial engineering (DII) of the University of Trento.

Graphite powder (Fluka Chemie, DE) is mixed with liquid polycarbosilane (SMP-10, Starfire Systems, US) in acetone suspension. The mixture is dried for 24 h in an oven at $150°C$ to remove the solvent and is then loaded into a 20 mm diameter die and pelletized with a hydraulic press at 160 MPa. The pellet is then pyrolyzed in a graphite furnace (Astro, Thermal Technology LLC, US) with a heating rate of $5°C/min$ up to $1600°C$ being kept at such temperature for 2h, and then cooled down with cooling rate of $15°C/min$. To avoid oxidation of the pellet the process is performed under Argon flux of $300cm^3/min$.

The ceramization process leads to a relative weight loss of SMP-10 of 26.3% and, considering that the pyrolysis of SMP-10 gives stoichiometric SiC, this allows to calculate the theoretical weight fraction of silicon inside the sintered pellet.

Graphite:SMP10 (wt ratio)	Compressive load ($\mathbf{MPa}$)	Bulk Density ($\mathbf{g/cm^3}$)	Estimated Si % wt after pyrolysis
10 : 3	110	1.47	11.9
10 : 2	160	1.41	8.6
10 : 1	160	1.54	4.7
30 : 1	110	1.40	1.7
100 : 1	110	1.46	0.5

Table 5.1: General properties of sintered samples. The estimated Silicon content is calculated taking into account the loss of SMP-10 during the pyrolysis.

During this work the various samples will be identified using the initial weight ratio or percentage weight ratio of graphite and SMP-10; that is the one with the highest silicon concentration will be called the 10:3 or 30% sample and so on.

This preparation procedure is called Polymer-Derived Ceramic (PDC) route. PDC allows to use complex pre-ceramic polymers which can be turned into the desired ceramics by sintering at high temperature in controlled atmosphere [6]. This makes the use of PDC particularly suited to the production of non-oxide ceramics like SiC or more complex compositions like SiCN, SiBCN; with the possibility of pre-doping the material with other elements like transition metals [7].
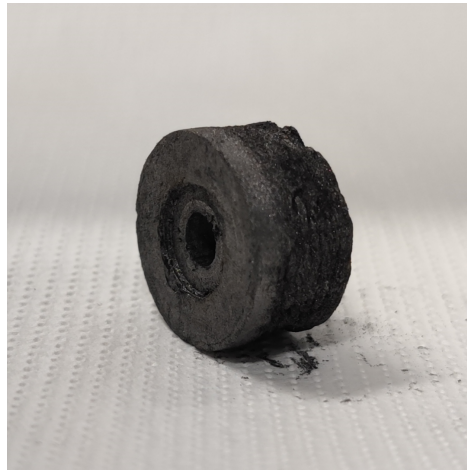
Figure 5.1: Photograph of the 30:1 precursor after ablation in water. The ablated surface is shifted to one side to avoid degradation of the plastic support structure shown in the previous chapter, the pristine flat face is the region were samples are obtained for SEM and EDXS measurements.

The polymer to ceramic evolution is characterised by the formation of amorphous ceramics that generally undergo phase separation at the nanoscale as pyrolysis temperatures exceed $1000 - 1200°C$[8] which could be exploited to produce nanocrystalline ceramics[9, 10].

The precursor structure has been observed by taking samples of the material from the circular faces of the cylinders in order to avoid damages or contamination to the surface involved in the PLA process. The morphology is shown in section 5.3.3. As will be shown the precursors present some impurities and their composition has been analysed by Energy Dispersive X-ray Spectroscopy (EDXS).

In table 5.1 one can see that the bulk density of the precursors falls in a range between $1.40 - 1.54 g/cm^3$ and the estimated Si content covers a large

interval from 0.5% to $\sim 12\%$. The silicon concentration range is compatible with concentrations explored in literature for other techniques, e.g. the work from Bolshakov et al. [4].

Although the formation of diamond phase in CVD and PLAL processes is extremely different, this observation coupled with the experimental results shown in the next section informs our decision to avoid exploring precursors with higher silicon concentration.

In this work we also avoid performing a "blank" synthesis, that is with no silicon present, because in previous works in our laboratory the formation of non-fluorescent nanodiamonds was already shown [11]

5.2 Processing

Ablation

As opposed to the procedure performed in chapter 4, here the precursors are ablated in ultrapure water. Working at room temperature allows for much easier to control operation, the targets can be positioned with care without the risk of jamming the mechanisms with ice. Moreover the low rate of evaporation of water is helpful in maintaining the operation working for longer, without pauses to refill the containers or the need to precisely program the vertical movement of the apparatus, necessitating only of small adjustments over hours of operation.

The apparatus employed in this procedure remains largely the same as that schematised in chapter 4, with only minor modifications.

Working with water at room temperature does not require additional temperature control for the system, so the external polystyrene container acts only as a support for the internal beaker.

Purification

In chapter 4 the samples have been subjected to two different purification procedures: Thermal oxidation in air[12–14] and high temperature acid treatment[13, 15, 16].

Here the procedures are combined as two steps to be performed one after the other.

The raw powder is subjected to the acid treatment as shown in the previous chapter for the NV luminescent nanodiamonds. After this first step,

most of the powder is degraded, leaving behind only the nanodiamond and silicon carbide components of the powders, with minor contribution from non-diamond carbon species. None of the metallic impurities present in the precursors appears to survive this step, as shown in the next sections. Neutralisation of the dispersion and the removal of salts is performed in the same manner discussed in chapter 4.

The second step consists in a 72 h oxidation process which can remove the remaining sp^2 carbon at the micro/nano scale.

While before the nanopowders were subjected to high-temperature oxidation on the substrate used for the measurements (quartz for optical characterisation and silicon wafer for SEM imaging), here the second step is performed on all the chemically purified material.

The powders after chemical purification are stored in suspension in either deionised water or ethanol, this suspension is poured in a small crystallizer on a heated plate and the solvent is left to evaporate at low temperature (below the boiling point). Once the powders form a thin dry layer on the bottom of the glassware, they are subjected to the heat treatment in a tube furnace (Carbolite CTF 12/65/550) starting with a ramp of $5°C/s$, then they are kept at $425°C$ for 72 h and lastly they are left to cool relatively slowly overnight with the furnace turned off.

The powders are later redispersed in ethanol. The results of the procedure are shown in the next section. All samples have been observed both after only the chemical purification step and after the full procedure.

Already one problem with the procedure is apparent: the nanodiamonds coexist with silicon carbide nanoparticles and larger fragments of SiC. The larger particles can be removed by sedimentation, but this is not possible for the smaller ones since SiC and diamond have similar density.

Moreover SiC appears to be even more resistant to chemical attacks then diamond and is unaffected by thermal processes even at temperatures in excess of $700°C$.

In this work therefore the studied material is a mixture of nanodiamonds and SiC nanoparticles.

A possible solution, partially explored at the end of the work, appears to be the use of ammonia solution as dispersing medium, which from literature is found to selectively stabilise the suspension of nanodiamonds while allowing the sedimentation of silicon carbide nanoparticles[17, 18].

5.3   Characterizations

As previously written, the samples have been subjected to an extensive characterisation campaign with different techniques.

The observation in sample 10:1 of photoluminescence in the region surrounding the $\sim 738nm$ wavelength associated with the ZPL of the SiV center [19, 20] led to the full characterization campaign described in this section.

The samples have been observed in order of fabrication, that is first the 10:1, followed by the two higher concentration samples and lastly the 3% and 1% ones.

In this section I will show the results of the different characterizations performed on the samples, focusing on the oxidized materials, that is the nanopowders subjected to the full post-processing procedure described in the previous section.

5.3.1   SEM and EDXS characterisation

The morphology of the samples has been observed using a Jeol JSM-7001F Scanning Electron Microscope, equipped with an Oxford INCA PentaFETx3 EDS for compositional analysis.

SERS substrate

While the NDs produced by PLAL in liquid nitrogen described in Chapter 4 have been deposited on different substrates for optical characterisation and SEM imaging (quartz and silicon respectively); here the powders have been deposited on the same conductive substrate for both characterisations.

This was necessary to perform Surface Enhanced Raman Spectroscopy (SERS) as will be discussed in section 5.3.4. Here in fig. 5.2 one can see the nanostructured silver substrate employed, which was produced by evaporating Ag on a silicon wafer. The use of the silver substrate allows not only to perform SERS measurements, but also to observe with the different techniques the exact same points on the sample, without switching between the ones deposited on quartz and the one on silicon.
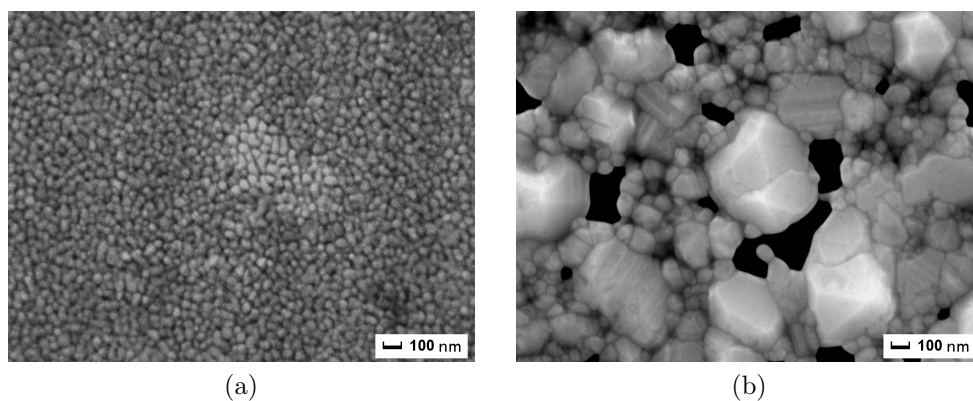
Figure 5.2: (a) SEM micrograph of pristine silver substrate, the surface shows nanostructures in the order of the tens of nm. (b) Larger recrystallised silver structures appear just outside the region occupied by the deposited sample. The black areas are deeper holes in the substrate that trap scattered electrons.

The surface of the substrate shows the presence of relatively uniform islands $\sim 20nm$ in diameter, clearly visible in panel (a) of fig. 5.2. Notably in the proximity of the deposited powder the structures can appear modified as can be seen in panel (b), showing larger structures which appear to have recrystallised since some of the atomic planes can be glimpsed from the image. This could be due to overheating during some of the longer SERS measurements. Another possibility is that this modified region of the substrate is caused by the force exerted on the 100 nm thick Ag layer by the evaporating solvent at the moment of the deposition of the powder. The retreating liquid may have dragged some of the grains of the substrate, upturning the islands and exposing the bottom layer of the silver, generating the voids that can be seen in panel (b).

In figure 5.3 one can see an SEM micrograph obtained by superposition with false colors of an SEM image taken from back scattering electrons and Secondary emission electrons showing a low magnification image of the samples.
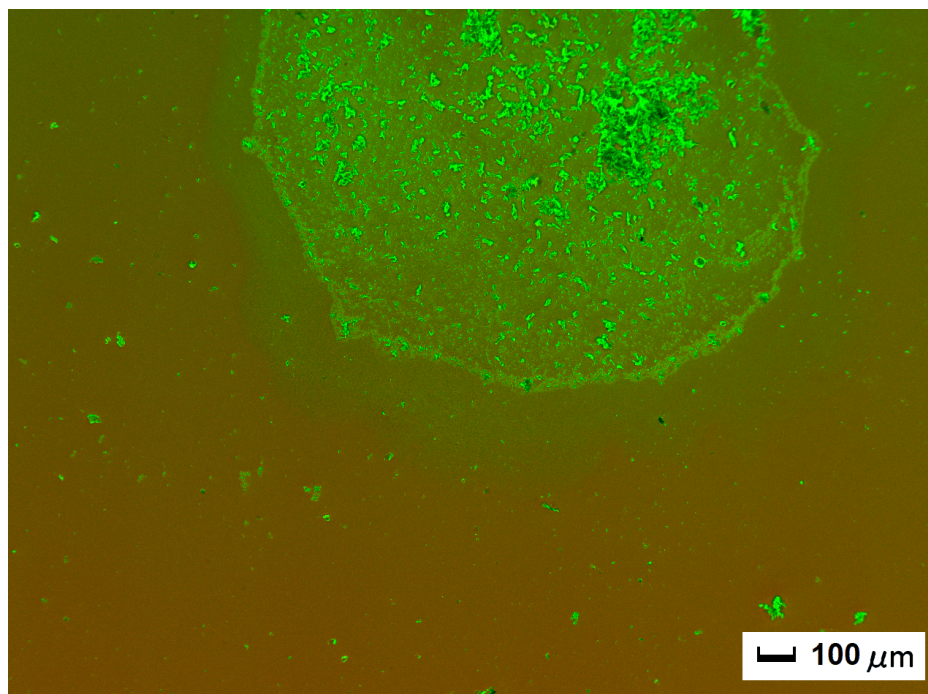
(a)

Figure 5.3: Low magnification SEM micrograph of sample 100:1 over the silver substrate. The composite image (Secondary electrons and backscattered electrons) clearly shows the difference between the light atoms of the nanopowders in green and the heavier silver atoms of the substrate in orange. Some large fragments appear outside the main patch due to handling of the sample.

The nanopowders are composed of light elements and appear bright green over the orange of the silver substrate.

Around the main cluster of powders, corresponding to the dried dispersion drop, a green halo can bee seen, clearly separated from the surrounding dull orange of the substrate. This is the region observed in panel (b) of fig.5.2. The presence of this halo suggests the presence of lighter elements over the silver substrate, yet SEM observation do not show the presence of nanoparticles in this region. This could be explained considering that some of the solvent in which the particles were dispersed (ethanol) may have seeped in the voids that can be observed in this region. Alternatively the displacement of the silver layer may lead to increased contribution of the

underlying silicon wafer to the signal.

The analysis of the different samples was focused on the main patches of material, avoiding the surrounding fragments.

Precursors

The precursors used in this work are characterised by a microscopic structure composed of relatively large graphite fragments, with major dimension in the tens to hundreds of micrometers, sintered together at the boundaries, with smaller SiC grains interspersed between the larger particles. From fig. 5.4 one can see that all the precursors show clear separation between the graphite matrix and the smaller SiC inclusions.

Panels (a,b,d) show a similar configuration of relatively uniformly distributed SiC conglomerates. In the center of panel (b) one can also see a bright white spot, indicative of the presence of heavier elements. This spot is shown in detail in panel (c), here the image is taken as a composite of backscattering and secondary electrons, highlighting the composition of the different structures. The graphite appears green in this observation mode, while the silicon carbide appears as a dull yellow/green color. Several SiC structures appear throughout the image, generally along the borders of the graphite grains where the liquid SMP-10 was trapped during the pelletisation process and presenting a rounded morphology.

At the center of the image the impurity appears brigh orange, EDXS measurements show it is composed of tungsten.

Panel (e) instead shows that the 30% precursor contains large, elongated structures of SiC tens of micrometers long in addition to the smaller, rounded structures one can see in the other precursors.
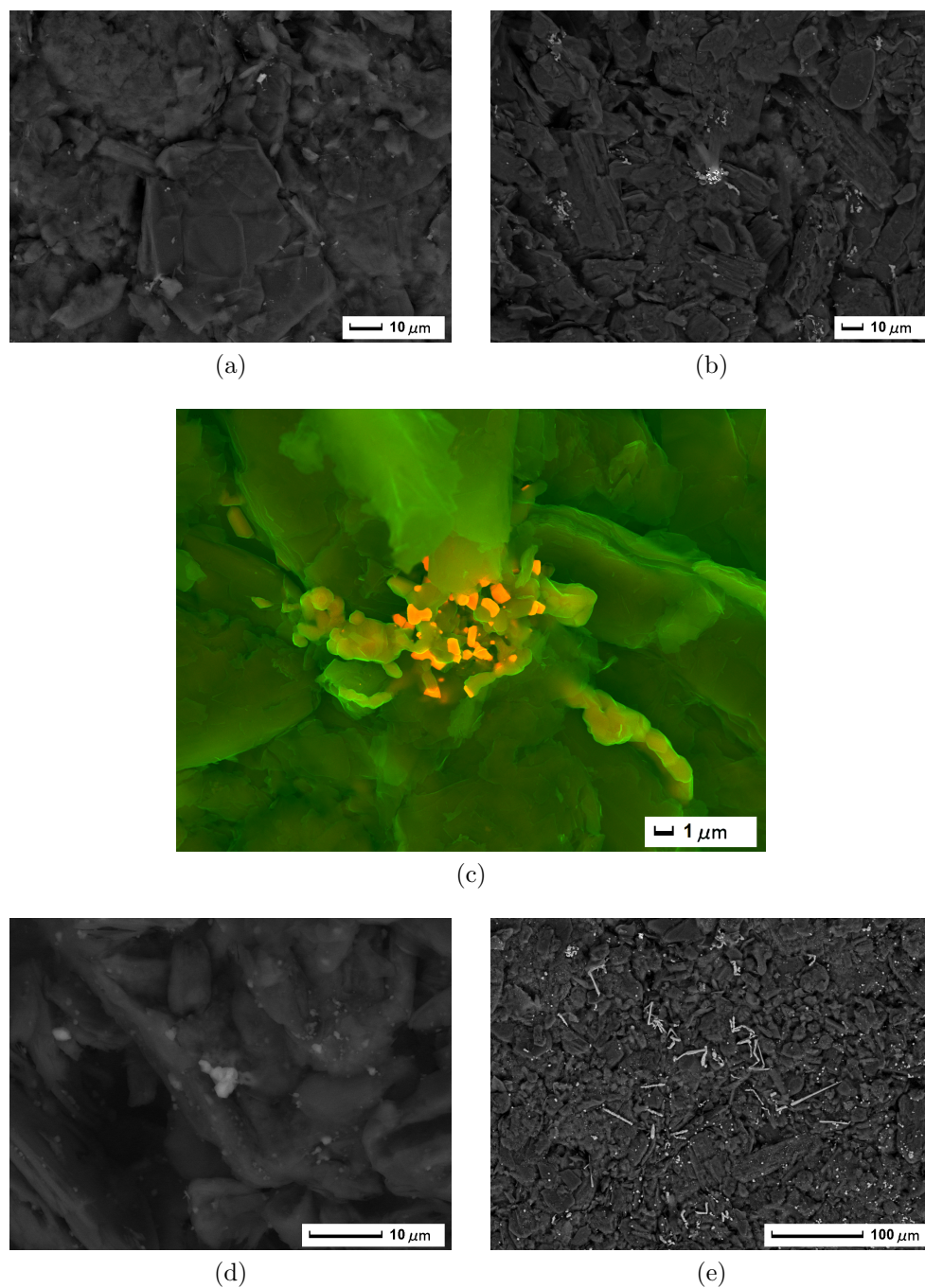
Figure 5.4: Panel (a,b,d,e) show the morphology of the $1, 3, 20$ and 30% samples respectively. Panel (c) is a composite image of secondary electron emission and back scattered electron showing a detail of panel (b), focused on the impurity at the center of the image.

(a)

(b)

(c)

(d)
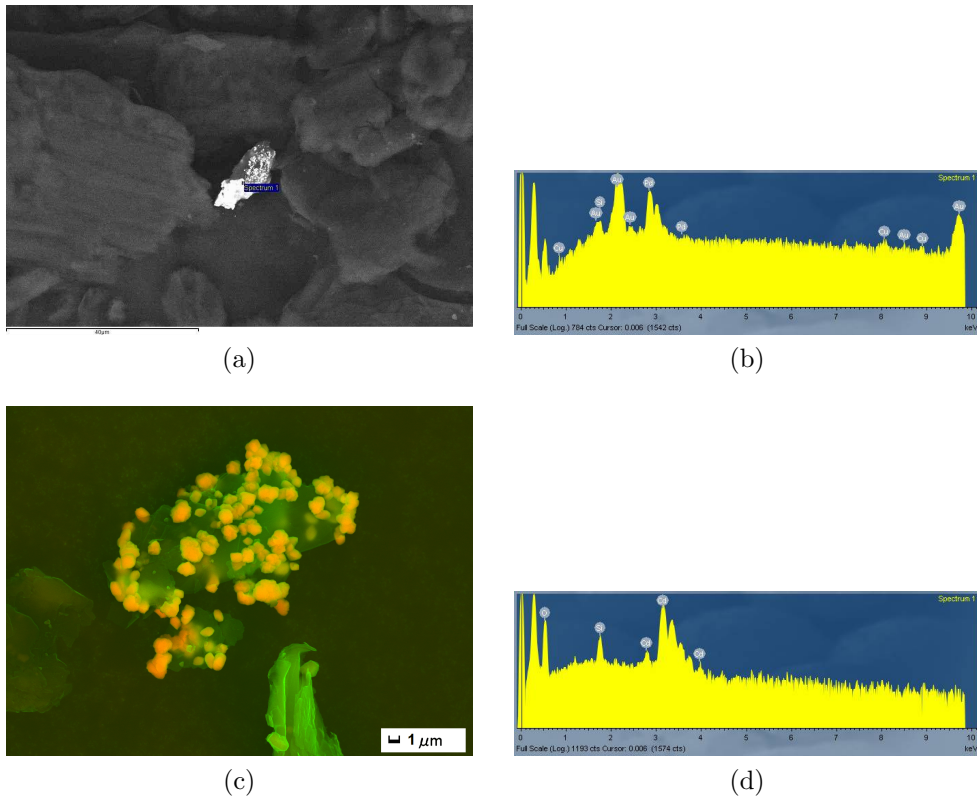
Figure 5.5: SEM and EDXS spectra of impurities found in precursors. Panels (a,b) are associated to the 1% precursor, while panels (c,d) to the 20% precursor

Other impurities are shown in figure 5.5 and it was found that each precursor shows the presence of different metallic fragments, which are identified by EDXS. In the case of the 1% precursor the observed impurities in panel (a) were made of gold and for the 20% (c) of cadmium, with the corresponding EDXS spectra in figure. Not depicted here there were also impurities in the 30% precursor which are composed of a blend of elements typical of steel.

Each precursor has been analysed after the ablation process. The observed metallic fragments cannot come from the environment of the laboratory, where the equipment is adequately cleaned before use and the cylinders only come in contact with ultra-pure water used during the ablation process.

They can instead be residues of previous preparations inside the die or residues of the machining necessary to mount the cylinders on the apparatus.

These impurities are not observed in any sample, which is a confirmation of the efficacy of the purification procedure.

The original 10 : 1 precursor has not been characterised as the others because during a second ablation procedure in liquid nitrogen (for a possible future project) the cylinder was accidentally destroyed.

Nanomaterials from PLAL

(a)   (b)

(c)

Figure 5.6: Representative SEM micrographs of the powders of sample 100:1 (a) and 30:1 (b,c). Panel (a) is a composite image of secondary electrons and back scattered electrons. Panel (b,c) is shown only with secondary electrons for clarity.
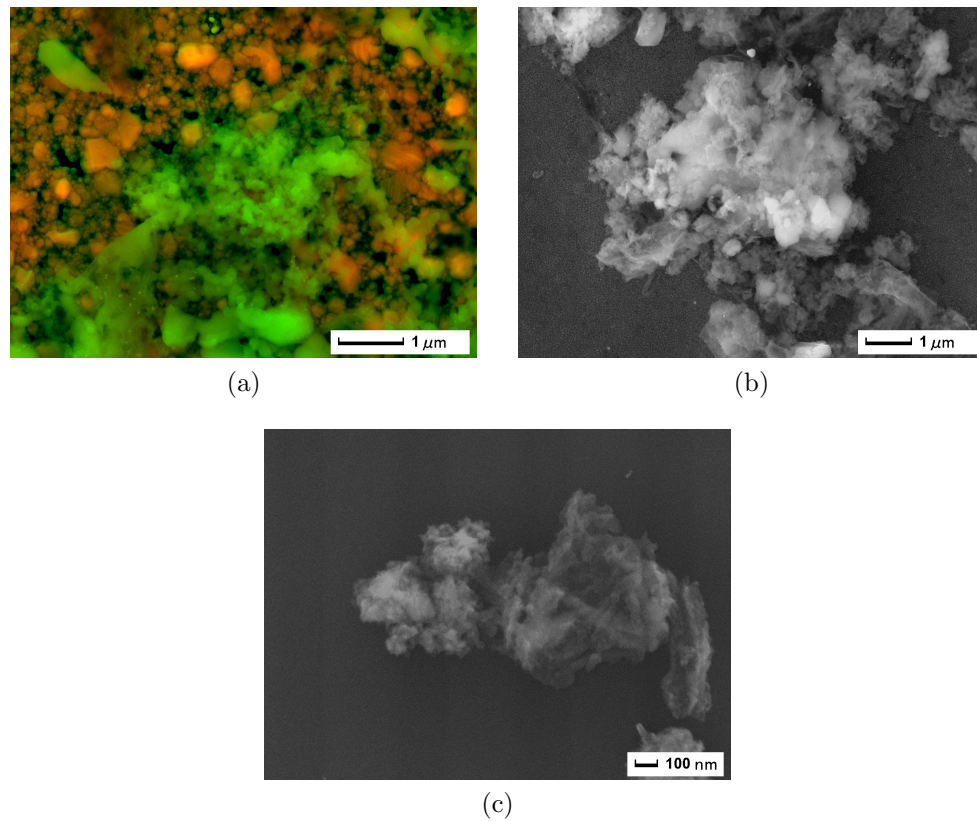
The SEM analysis of the samples shows a complex morphology.

Figure 5.6 shows the morphology of the samples 1% and 3%. In particular panel (a) is taken at the same position observed in the SERS measurement that produced figure 5.13 (a) plot in section 5.3.4.

The morphology is compatible with previous observations of nanodiamonds produced from PLAL[13, 21]. The bright green carbon conglomerate at the center of the image stands out over the orange of the silver substrate.

Looking at panel (b) one can see that the morphology of sample 3% is already more complex, with a larger variety of structures observed on the sample. While in panel (a) there were some large polyhedral particles, here they form a large conglomerate together with more amorphous structures. Pane (c) shows instead a detail of the 3% sample, showing a small conglomerate in which the presence of both spherical and sheet like structures are present.

The other samples are shown in figure 5.7. A cursory glance is enough to notice that the morphology of the samples exhibits more structures associated with silicon carbide proportionally to the concentration of silicon carbide in the precursor.

Panels (a,b) show the morphology of sample 10%, large SiC particles exhibit polyhedral morphology, between the larger particles a matrix formed by smaller SiC nanoparticles and amorphous carbon presents the presence of some more rounded particles which can be associated with previously observed ND morphology. In particular panel (b) shows a small conglomerate of round particles on top of a slightly larger column of SiC, which is one of the clearer examples of the different particles present in these samples.

Panels (c,d) show the morphology of sample 20%. This sample shows the presence of large fragments composed of an amorphous matrix interspersed with different kinds of nanoparticles (c). In particular the detail in panel (d) shows peculiar nanoparticles which appear particularly defective, which may be associated to the emission observed in the section 5.3.3 for the 20% sample. This particular structures seems exclusive to this sample.

Panels (e,f) lastly show the sample with highest concentration of SiC. The morphology here appears uniform over the prepared samples, composed mostly of sub-micrometer particles, together with larger particulate. Panel (e) is a good representation of the morphology of the whole sample, with few differences over the surface. Panel (f) shows an outlier in the form of three larger particles connected by what appears to be a conglomerate of finer particles, isolated from the rest of the material.
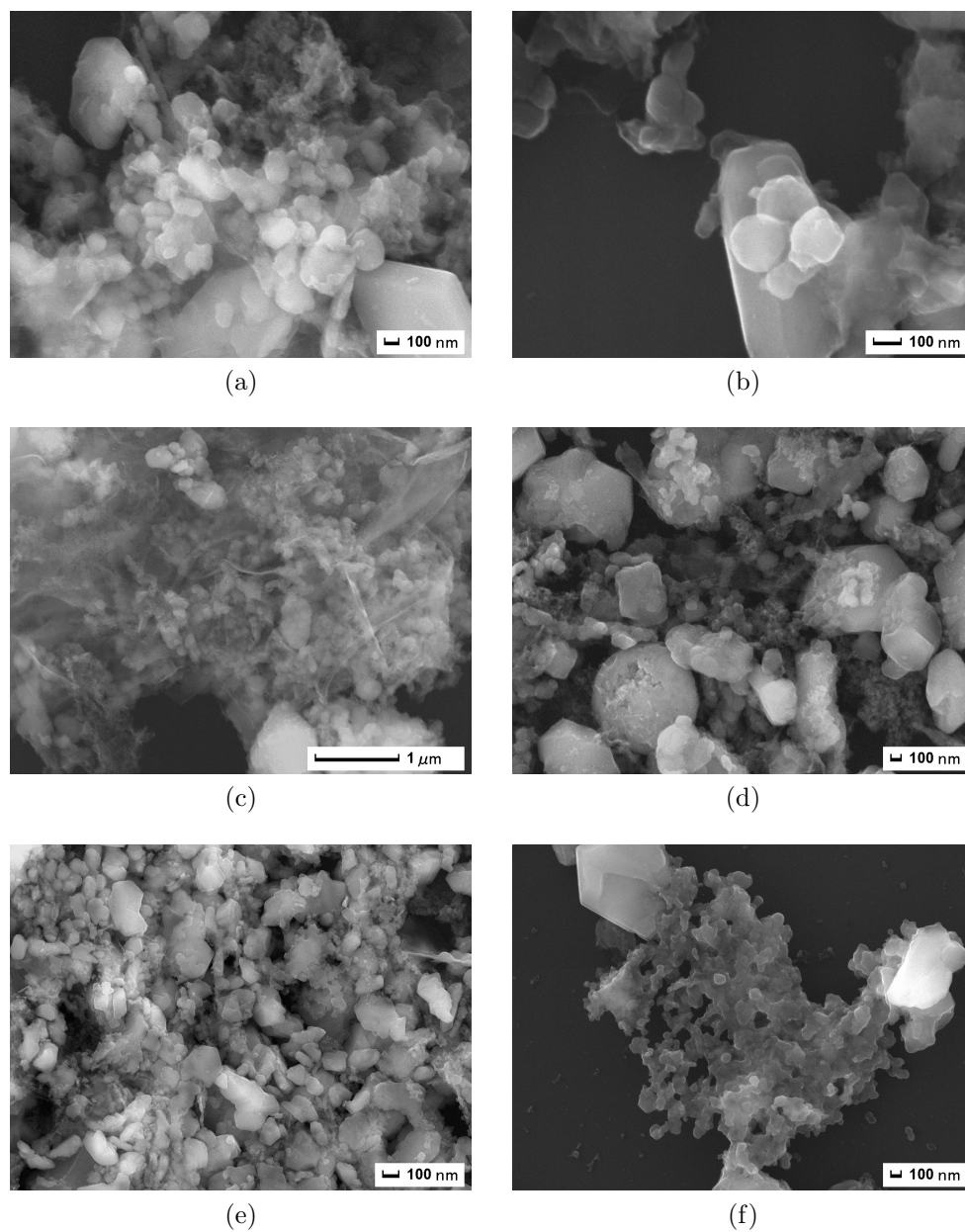
Figure 5.7: Relevant SEM micrographs of the sample 10:1 (a,b), 10:2 (c,d) and 10:3 (e,f)

This more uniform morphology composed of larger, and well crystallised

particles, considering also the results of the Raman analysis (section 5.3.4) which present sharp and intense peaks which practically reproduce bulk SiC features, can be associated to the much lower optical activity of the sample (section 5.3.3). This sample is also the only one to sometime exhibit Raman peaks typical of Si nanoparticles, but it does not appear to form structures which can be distinguished from the surrounding SiC particles.

5.3.2 TEM and SAED characterisation

(a)   (b)
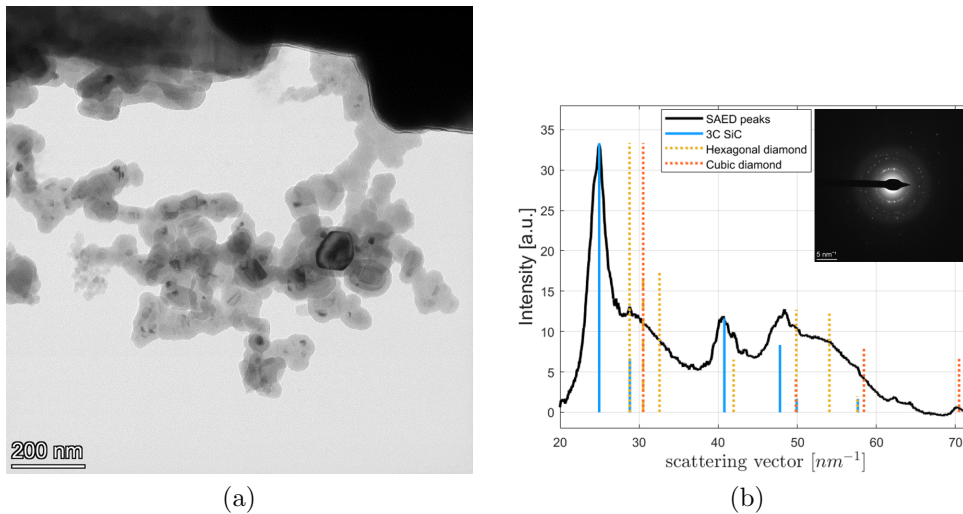
Figure 5.8: TEM micrograph of the 3% sample (a) and intensity profile (b) of the corresponding diffraction rings (b-inset)

The samples are prepared by depositing a drop of a diluted suspension of the 1% and 3% samples on a carbon-coated Cu TEM grid. The TEM characterisation was performed only on the two samples which showed the presence of diamond in the Raman Spectroscopy experiments, as will be discussed in the next sections.

TEM/SAED measurements are performed with a Thermo Scientific Talos F200S microscope at an accelerating voltage of 200 kV.

The grids are first observed in the SEM in transmission configuration (STEM) in order to image the samples and define regions of interest for the TEM Experiments.

Figure 5.8 shows an example of the observed particles, together with the results of the corresponding Selected Area Electron Diffraction (SAED) experiments.

The main contribution to the spectra is from the silicon carbide crystallites, as can be seen from the SAED plot. Here the plot reveals that the nanoparticles under examination are composed of cubic 3C SiC [22].

The plot also presents faint peaks in correspondence to the expected position for diamond. The comparison are performed both with standard cubic diamond and hexagonal diamonds as seen in figure, in fact in this particular cluster the hexagonal diamond contribution appears stronger than that of normal cubic diamond.

The peaks appear to be superimposed to a broader structure of more diffused bands. Observing the expected peak positions of cubic and hexagonal diamond these bands appear to be related to a superposition of both components.

These broader features can be considered the fingerprint of extremely small crystallites [23] either inside the nanodiamond (that is diamond nanoparticles with ultra-nano crystalline domains) or as separate ultra-nanodiamonds being part of the matrix connecting the other nanoparticles in the conglomerates, in the shell-like structures observed in panel (a) of fig. 5.8. This second possibility is corroborated by the presence of the broader bands also on nanoparticles exhibiting only the SiC peaks.

Over the various measurements we were able to evaluate the (111) interplane spacing by observing the position of the relative SAED peak. The values obtained differed from the expected $d_0 = 2.0975$ Å[24] by at most $\Delta d_0 = 0.0395$ Å. This shift can be interpreted in terms of local nanoscale strain fields, which correspond to a maximum stress acting on the probed NDs of $\sigma \sim 21 GPa$, compatible with strain fields acting on diamond nanostructures as those observed in fig. 5.8, in fact the largest stress observed in this work amounts at most to $\sim 20\%$ to the maximum stresses observed in [25].

5.3.3 Photoluminescence Spectroscopy Results

The samples have been observed under 532 nm and 633 nm excitation with a Jobin-Yvon LabRam Aramis spectrometer. As described in chapter 3, SiV centers in diamond show a very sharp emission at 738 nm. In nanodiamonds, the emission appears to be broader, due to size effects (quantum confinement,
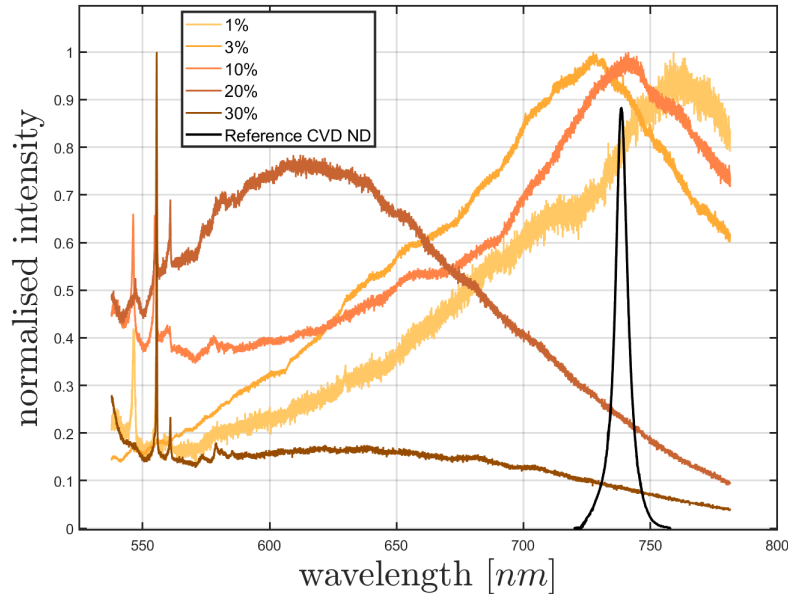
Figure 5.9: Representative photoluminescence spectra of the samples after the full chemical and thermal cleaning procedure, described in terms of the initial Si concentration of the precursor; in black the reference emission from literature. The reference CVD ND emission is reproduced from [26]

strain in the crystal lattice)[15, 27].

The photoluminescence of the different samples is shown in figure 5.9 and discussed in the next paragraphs. All samples show some sharp Raman peaks near the wavelength of the pump laser, which are going to be discussed in the next section.

The 10:1 sample

Going in order of sample preparation, the first measurements were performed on the original 10:1 sample. This is the only sample that shows significantly different behaviour between the as deposited and oxidised powders. In fact, as can be seen in figure 5.11, the as deposited powders show no luminescence in the region of interest surrounding the 738 nm value, at any observed point. Instead in the oxidised powder we observe the presence of a broad emission band in the red-near infrared region of the spectrum.

This observation on 4/50 observation points spurred the analysis of other samples with different silicon concentrations.

The 10:2 and 10:3 samples

The sample 10:2 shows only a broad band in the orange-red part of the spetrum . This was also observed in the 10:1 sample, but was originally associated with sp^2 carbon structures (graphene oxides, carbon nanodots). Since the observation persists in both samples even after the oxidation of the nanopowders, this emission band can be attributed to emissive defects in the silicon carbide nanoparticles, in particular to deep level defects in 3C-SiC nanoparticles [28] and/or C-vacancies in SiC nanoparticles [22] (the composition of the NPs is described in more detail in the next section). This is a possible unforeseen feature of the material because such defects are good candidates for single-photon emission quantum-optical applications [29].

Sample 10:3 showed no bright luminescence under either 532 nm or 633 nm excitation. The spectra observed show only the sharp Raman peaks of silicon carbide. This is somewhat unexpected because after the observation for the previous sample one would expect some contribution (if not more given the higher concentration) from products of the ablation of SiC.

This observation could be related to the mechanical properties of the 10:3 precursor, which appeared much softer and difficult to work with, requiring additional care while being mounted on and removed from the apparatus and in particular during the initial machining after sinterisation.

The 30:1 and 100:1 samples

Again in fig. 5.9, one can see that both of these samples present emission in a broad band surrounding the expected position for the emission of SiV centers in the near infrared region of the spectrum. In opposition with what is observed for the 10% sample, here both the oxidised and non-oxidised powders show photoluminescence, with a slight increase in the oxidised powders, again associated to the removal of residual layers of sp^2 carbon, as shown in figure 5.11.

The near infrared band observed on the three samples with lower concentration can be attributed to silicon vacancy centers in NDs [26]. The peculiar

width of this band can be explained in terms of strong inhomogeneous broadening of SiV in strongly strained NDs with dimensions $< 100nm$ as well as from unidentified silicon related defects [2, 15, 27].

Moreover, the ZPL of SiV centers in NDs can be significantly shifted from the 738 nm value, in particular [27] reports ZPL distributions in the range $715–835nm$, also associated with linewidth ranging up to 18 nm. This together with the fact that the NDs observed are part of relatively large conglomerates, as will be shown in the next section, can explain the broadening of the emission as a superposition of the photoluminescence of different SiV centers embedded in different strongly strained NDs.

The 3% sample emission was also measured using a spectrometer setup which allowed the observation of the full surface of the sample (Ocean Optics spectrograph, 1 nm spectral resolution, 517 nm quasi-CW -10 MHz repetition rate for 10 ns long laser pulses- diode laser, 1 mW on average over the sample surface), even under relatively low pump power the band is visible as shown in figure 5.10
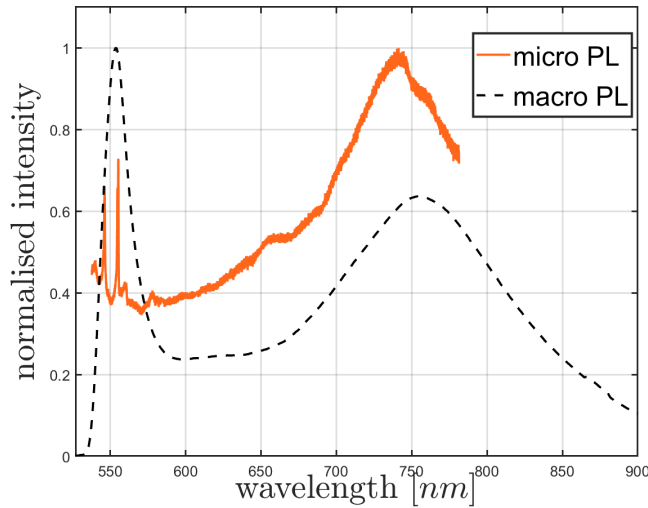

Figure 5.10: Comparison between one emissive spectrum of sample 3% and the PL collected over the full surface of the deposited powder.

The macro-PL of the powder appears shifted to higher wavelengths, suggesting that the tail emission at $550 - 700nm$ is likely related to emission from other carbon conglomerates, like carbon nanodots, which might survive

the purification steps (particularly if enveloped together with the other more stable species) [30, 31]. The disappearance of this tail under $633nm$ excitation supports this attribution and is a typical spectral fingerprint of carbon nanodots PL emission.

(a)   (b)
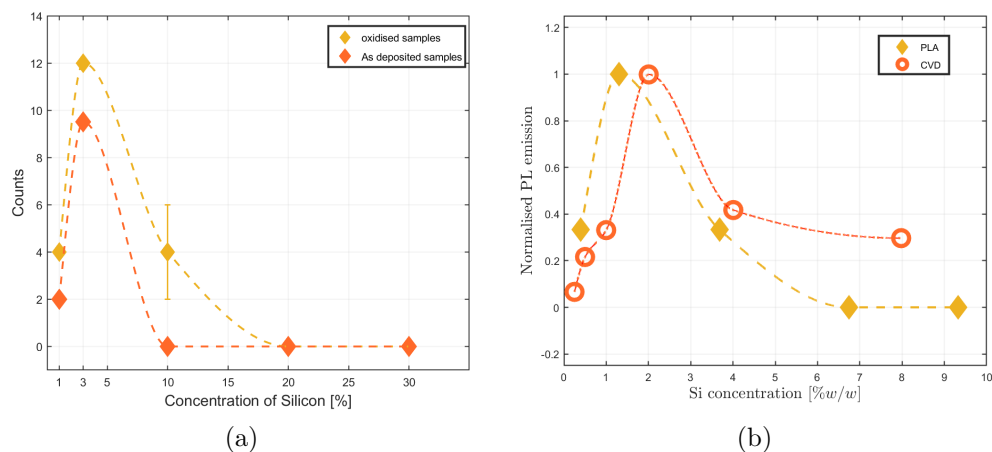
Figure 5.11: Panel a: abundance of emitting points in the different samples in dependence to the nominal Si concentration in the initial precursor. Each is the result of measurements over sets of 50 points. Panel b: comparison between PLAL and CVD production of SiV fluorescent NDs, PLA silicon concentration shown as estimates of effective concentration as seen in tab. 5.1. The CVD results are derived from [4]. The connecting dashed lines are just a guide for the eye.

The number of emitting points results highest in the 30:1 sample, suggesting that the ideal concentration of silicon for the formation of SiV centers by PLAL is around $\sim 1.7\%$ as seen in panel a of fig. 5.11.

The behaviour of the photoluminescence in dependence to the silicon concentration appears to be associated mostly to the efficiency of formation of NDs with SiV centers, without particular changes in the properties of the spectra of the 3 emitting samples.

What we propose is that the excess of silicon in the precursors 10:2 and 10:3 inhibits the formation of nanodiamonds due to the peculiar behaviour of the carbon-silicon system. This is observed also in CVD synthesis [4] where

excessive silicon concentration distorts the crystalline lattice and reduces the formation of the desired structures. On the other end, at lower concentration the silicon acts more as a dopant rather than a stoichiometric component, allowing for the formation of the desired impurities without damaging the crystalline structures. For the lowest concentration then the reduction of the emissive points is only related to a reduction of the available silicon. The comparison with the CVD produced NDs is shown in panel b of fig. 5.11, here the results are normalised to the maximum of each dataset. In order to compare the different techniques here the data are shown in terms of the Si concentration of the precursors after pyrolysis as specified in tab. 5.1.

5.3.4 Raman Spectroscopy Results

In the previous section, the Raman spectra were already visible in the photo-luminescence plots, in particular the more intense peaks of the silicon carbide.

Focusing more on the $100 - 2000 cm^{-1}$ window one can analyse the spectra in order to investigate the chemical composition and the crystalline structure of the material.

The main components of the powders are silicon carbide particulates and nanodiamonds, with the exception of some larger fragments which clearly show the composition of graphite: the G and D peaks of graphite are clearly visible at around $1580 cm^{-1}$ and $1345 cm^{-1}$ respectively. The relative intensity of the peaks show that the material in the larger fragments are well crystallised and unmodified by the ablation process.

In the three larger concentration samples the dominant features are those of silicon carbide. In particular one can see, as shown in figure, that the samples show the presence of both α-SiC (6H hexagonal polytype) and β-SiC (3C cubic polytype)[22]. The presence of the 3C SiC polytype is an indication that the silicon carbide nanoparticles undergo a modification during the ablation process, since the dominant polytype in SiC produced by equilibrium routes is the cubic α-SiC, while shock experiments show a decrease of the hexagonal phase coupled to an increase of cubic and rhombohedral phases[32]. The more evident peaks are those related to the Transverse Optical (TO) vibration modes as highlighted in fig. 5.12 [22, 33]. Other features of SiC are visible in the region around $\sim 950 - 1000 cm^{-1}$ and $\sim 1400 - 1600 cm^{-1}$. The latter shows also the presence of graphite contribution, in particular from the sample pre-oxidation.
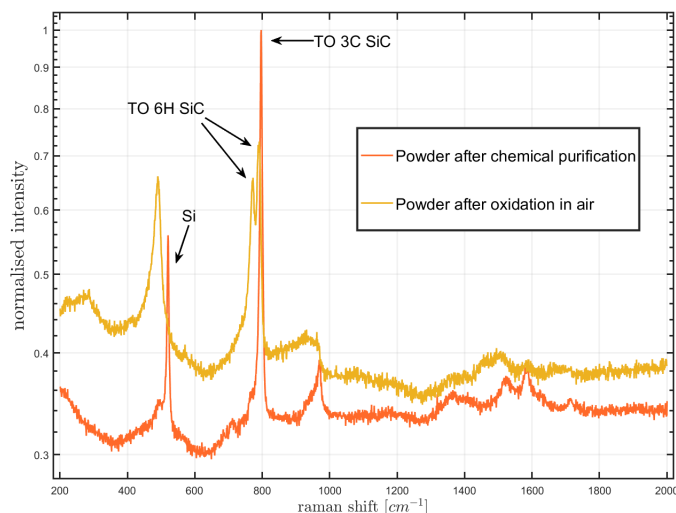
Figure 5.12: Detail of the Raman spectra obtained from the 10:3 sample. One can observe the presence of both the α-SiC and β-SiC structures.

Another sharp peak at around $517 cm^{-1}$ is attributed to nanocrystalline Si present in the nanopowders, which is absent in lower concentration samples.

The observation of the Raman signal of diamond results more problematic. At the available pump wavelengths (532, 633 and 785 nm, but the green 532 nm was not available for most of the experimental observations) the Raman signal of diamond is particularly weak because it is far from resonant frequencies in the UV-C range [34].

In order to alleviate the problem Surface Enhanced Raman Spectroscopy (SERS) measurements are performed using a nanostructured silver substrate[35–37]. The substrate used was shown in in fig. 5.2.

The substrate was tested on commercial fluorescent nanodiamonds (Sigma-Aldritch). The intensity of the diamond peak obtained from SERS measurements of commercial NDs is 2.5 times larger than that obtained from the same NDs deposited on either quartz or bare silicon wafer, even with relatively loose contact between the nanopowders and the substrate (the particles are simply deposited as usual, without employing any implantation technique, e.g. laser accelerated deposition). The measurements were performed under 785 nm excitation in order to avoid the photoluminescence of the NV centers in the commercial nanodiamonds.

(a)   (b)
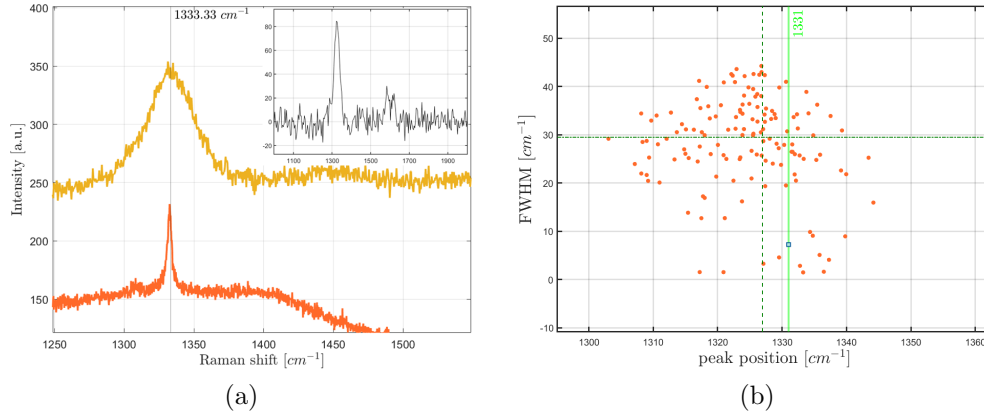
Figure 5.13: (a) Long exposures, high resolution Raman spectrum centered of a region of sample 30:1 which shows the peak of diamond, the reference spectrum is obtained from Sigma-Aldritch fluorescent nanodiamonds in the same experimental conditions. (a) - inset: spectrum from a low resolution fast measurement over the 30:1 sample. (b) Width versus position plot of the observed Raman peaks of diamond in sample 30:1 over 400 measurements, the solid green line identifies the position of the Raman peak of bulk diamond, while the two green dashed lines represent the average peak position and peak FWHM of the observed peaks.

The signal measured in the PLAL powders remains very low, visible only on the oxidised particles and requiring long exposure times, with the risk of overheating the powders and damaging the sample.

Moreover, the particularly broad photoluminescence emission observed in the previous section makes detection of the weak Raman peak of diamond impossible when observing the spectra of the emitting points.

The three samples with higher concentration (10, 20 and 30%) show no presence of the diamond peak even in non emitting points. This is to be expected at least for the two samples with highest silicon concentration given the lack of observed PL in the SiV region and the previous discussion on the lower formation efficiency of NDs in these conditions.

The two lower concentration samples show instead the presence of diamond peaks with large FWHM and often relatively large shift in the peak position from the expected values of bulk diamond, as can be seen in figure 5.13

This is interpreted as the consequence of two phenomena: firstly the presence of intrinsic strain fields in nanodiamonds formed by PLAL, which was already observed in previous works [21, 38, 39] and also the fact that the observed nanodiamonds are always present in clusters, as shown by the SEM characterisation.

The sum of these effects causes both a shift and a broadening of the peaks. Moreover the nanodiamonds in the same cluster can in principle be host of different strain fields and therefore the different contributions can superimpose to form a large peak with low shift.

Mapping a large amount of point in the lowest concentration sample allows to perform a statistical analysis of the distribution of the peaks positions and FWHM, shown in figure 5.13 panel (b). Over 400 observation points $\sim 35\%$ of the them show a the presence of diamond signal. The FWHM of most of the observed data points is in the range of $\sim 20 - 40 cm^{-1}$. The peak position for the observed nanodiamonds exhibits shifts towards both higher and lower frequencies than that of bulk diamond. This implies the presence of both compressive and tensile stress respectively inside the nanoparticles. Observing the distribution for sample 3% a larger fraction of the observed data points shows tensile stress.

One can notice that the observation of the Raman peaks on less than 40% of the observed points means that the yield of the process is at least half than in the case of ablation of pure graphite in water (or liquid nitrogen) for the formation of nanodiamonds.

This can be seen as the result of using a non-ideal precursor as the target for ablation. In the Chapter 6 of this thesis I will focus briefly on this point and suggest possible solutions to the issue.

Yet the observed features of the Raman spectra of the 100:1 and 30:1 samples are in line with previously observed nanodiamonds produced from pure graphite [21, 38] in the same experimental conditions, and the attribution is corroborated by the observation of compatible morphology on the sites showing the Raman fingerprint of diamond.

5.3.5   Final remarks

The extensive characterisation campaign leaves some interesting results.

This work demonstrated that employing Pulsed Laser Ablation in water of composite precursors allows for the production of fluorescent nanomaterials.

The properties of these nanoparticles are strongly affected by the precursor composition and in particular by the effective silicon concentration.

Considering the production of fluorescent NDs with SiV centers we found an ideal Si concentration of 1.7% in weight.

The use of precursors with concentrations in a range of approximately $\sim 4.7 - 8.6\%$ Si promotes instead the production of fluorescent SiC nanoparticles, while at higher concentrations the system appears mostly optically inert.

While this opens the possibility of one-step procedures for the production of composite, fluorescent nanomaterials, with already good chemical purity; on the other end the explorative nature of this work results in materials that are far from being application ready.

In fact, the presence of such wide fluorescence bands in the agglomerated powders means that the main advantage of these silicon based materials over for example the NV center of diamond discussed above, that is the spectral purity of the emission and the possible single-photon emission properties, are not exploitable yet.

Some avenues for refining the process can be identified in better separation techniques for the existing nanomaterial and/or the production of precursors with better control over the microscopic structure of the pellet.

In fact in this work, while overall the concentrations were well defined, on the microscopic scale there were large gradients in the silicon concentration. Taking into account the fact that under equilibrium conditions carbon and silicon are immiscible, over few micrometers the atomic concentration of silicon goes from negligible inside the graphite grains to roughly 50% in the SiC clumps.

For this the PDC route could be refined in order to achieve a more uniform structure which could guarantee control of the silicon concentration to the micro or ideally even nano scale.

If one focuses only on the production of NDs, eschewing the formation of composite products, one could consider the use of precursors composed of Si-enriched graphite, e.g. by ion implantation.

Another possibility could be the production of sintered precursors, starting from already nanoscale materials, for example a solid mixture of carbon and silicon nanoparticles. This would have the advantage of using a relatively simple technique while still having a material with homogeneous micro scale structure. Moreover this could be achieved without employing silicon carbide, which avoids most of the difficulties of the separation process.

Bibliography

[1] Yuto Makino, Yoshiki Saito, Hikaru Takehara, Akihiko Tsurui, Naoto Okuyama, and Masaaki Ashida. Effect of particle size on the optical properties of silicon-vacancy centers in nanodiamonds fabricated by a detonation process. *physica status solidi (a)*, 219(22):2200342, 2022.

[2] Xiaohui Xu, Zachariah O Martin, Michael Titze, Yongqiang Wang, Demid Sychev, Jacob Henshaw, Alexei S Lagutchev, Han Htoon, Edward S Bielejec, Simeon I Bogdanov, et al. Fabrication of single color centers in sub-50 nm nanodiamonds using ion implantation. *Nanophotonics*, 12(3):485–494, 2023.

[3] Konosuke Shimazaki, Hiroki Kawaguchi, Hideaki Takashima, Takuya Fabian Segawa, Frederick T-K So, Daiki Terada, Shinobu Onoda, Takeshi Ohshima, Masahiro Shirakawa, and Shigeki Takeuchi. Fabrication of detonation nanodiamonds containing silicon-vacancy color centers by high temperature annealing. *physica status solidi (a)*, 218(19):2100144, 2021.

[4] Andrey Bolshakov, Victor Ralchenko, Vadim Sedov, Andrey Khomich, Igor Vlasov, Alexander Khomich, Nikolay Trofimov, Vladimir Krivobok, Sergei Nikolaev, Roman Khmelnitskii, et al. Photoluminescence of siv centers in single crystal cvd diamond in situ doped with si from silane. *physica status solidi (a)*, 212(11):2525–2532, 2015.

[5] Anke Krueger and Daniel Lang. Functionality is key: recent progress in the surface modification of nanodiamond. *Advanced Functional Materials*, 22(5):890–906, 2012.

[6] RIEDEL Ralf, MERA Gabriela, HAUSER Ralf, and KLONCZYNSKI Alexander. . *Journal of the Ceramic Society of Japan ()*, 114(1330):425–444, 2006.

[7] Donald Erb and Kathy Lu. Synthesis of sioc using solvent-modified polymer precursors. *Materials Chemistry and Physics*, 237:121844, 2019.

[8] Qingbo Wen, Zhaoju Yu, and Ralf Riedel. The fate and role of in situ formed carbon in polymer-derived ceramics. *Progress in Materials Science*, 109:100623, 2020.

[9] Yichen Wang, Peng Xiao, Wei Zhou, Heng Luo, Zhuan Li, Wenbo Chen, and Yang Li. Microstructures, dielectric response and microwave absorption properties of polycarbosilane derived sic powders. *Ceramics International*, 44(4):3606–3613, 2018.

[10] Luigi Ferraioli, Dongjoon Ahn, Atanu Saha, Lorenzo Pavesi, and Rishi Raj. Intensely photoluminescent pseudo-amorphous siliconoxycarbonitride polymer–ceramic hybrids. *Journal of the American Ceramic Society*, 91(7):2422–2424, 2008.

[11] Federico Gorrini, Massimo Cazzanelli, Nicola Bazzanella, Raju Edla, M Gemmi, V Cappello, J David, C Dorigoni, A Bifone, and Antonio Miotello. On the thermodynamic path enabling a room-temperature, laser-assisted graphite to nanodiamond transformation. *Scientific reports*, 6(1):35244, 2016.

[12] Sebastian Osswald, Gleb Yushin, Vadym Mochalin, Sergei O Kucheyev, and Yury Gogotsi. Control of sp2/sp3 carbon ratio and surface chemistry of nanodiamond powders by selective oxidation in air. *Journal of the American Chemical Society*, 128(35):11635–11642, 2006.

[13] Massimo Cazzanelli, Luca Basso, Claudio Cestari, Nicola Bazzanella, Enrico Moser, Michele Orlandi, Alessandro Piccoli, and Antonio Miotello. Fluorescent nanodiamonds synthesized in one-step by pulsed laser ablation of graphite in liquid-nitrogen. *C*, 7(2):49, 2021.

[14] Abraham Wolcott, Theanne Schiros, Matthew E Trusheim, Edward H Chen, Dennis Nordlund, Rosa E Diaz, Ophir Gaathon, Dirk Englund, and Jonathan S Owen. Surface structure of aerobically oxidized diamond nanocrystals. *The Journal of Physical Chemistry C*, 118(46):26695–26702, 2014.

[15] Yuto Makino, Tomoaki Mahiko, Ming Liu, Akihiko Tsurui, Taro Yoshikawa, Shinji Nagamachi, Shigeru Tanaka, Kazuyuki Hokamoto, Masaaki Ashida, Masanori Fujiwara, et al. Straightforward synthesis of silicon vacancy (siv) center-containing single-digit nanometer nanodiamonds via detonation process. *Diamond and Related Materials*, 112:108248, 2021.

[16] Luca Basso, Massimo Cazzanelli, Michele Orlandi, and Antonio Miotello. Nanodiamonds: Synthesis and application in sensing, catalysis, and the possible connection with some processes occurring in space. *Applied Sciences*, 10(12):4094, 2020.

[17] Gary R Huss and Roy S Lewis. Presolar diamond, sic, and graphite in primitive chondrites: Abundances as a function of meteorite class and petrologic type. *Geochimica et Cosmochimica Acta*, 59(1):115–160, 1995.

[18] Gary R Huss, Alex P Meshik, Julie B Smith, and CM Hohenberg. Presolar diamond, silicon carbide, and graphite in carbonaceous chondrites: Implications for thermal processing in the solar nebula. *Geochimica et Cosmochimica Acta*, 67(24):4823–4848, 2003.

[19] Elke Neu, David Steinmetz, Janine Riedrich-Möller, Stefan Gsell, Martin Fischer, Matthias Schreck, and Christoph Becher. Single photon emission from silicon-vacancy colour centres in chemical vapour deposition nano-diamonds on iridium. *New Journal of Physics*, 13(2):025012, 2011.

[20] SW Brown and Stephen C Rand. Site symmetry analysis of the 738 nm defect in diamond. *Journal of applied physics*, 78(6):4069–4075, 1995.

[21] Luca Basso, F Gorrini, M Cazzanelli, N Bazzanella, A Bifone, and A Miotello. An all-optical single-step process for production of nanometric-sized fluorescent diamonds. *Nanoscale*, 10(12):5738–5744, 2018.

[22] H Okumura, Eiichiro Sakuma, JH Lee, H Mukaida, S Misawa, K Endo, and S Yoshida. Raman scattering of sic: Application to the identification of heteroepitaxy of sic polytypes. *Journal of applied physics*, 61(3):1134–1136, 1987.

[23] ChengKe Chen, YingShuang Mei, JinMing Cui, Xiao Li, MeiYan Jiang, ShaoHua Lu, and XiaoJun Hu. Man-made synthesis of ultrafine photoluminescent nanodiamonds containing less than three silicon-vacancy colour centres. *Carbon*, 139:982–988, 2018.

[24] Anmin Nie, Yeqiang Bu, Penghui Li, Yizhi Zhang, Tianye Jin, Jiabin Liu, Zhang Su, Yanbin Wang, Julong He, Zhongyuan Liu, et al. Approaching diamond's theoretical elasticity and strength limits. *Nature communications*, 10(1):5533, 2019.

[25] Amit Banerjee, Daniel Bernoulli, Hongti Zhang, Muk-Fung Yuen, Jiabin Liu, Jichen Dong, Feng Ding, Jian Lu, Ming Dao, Wenjun Zhang, et al. Ultralarge elastic deformation of nanoscale diamond. *Science*, 360(6386):300–302, 2018.

[26] Igor I Vlasov, Andrey A Shiryaev, Torsten Rendler, Steffen Steinert, Sang-Yun Lee, Denis Antonov, Márton Vörös, Fedor Jelezko, Anatolii V Fisenko, Lubov F Semjonova, et al. Molecular-sized fluorescent nanodiamonds. *Nature nanotechnology*, 9(1):54–58, 2014.

[27] Sarah Lindner, Alexander Bommer, Andreas Muzha, Anke Krueger, Laia Gines, Soumen Mandal, Oliver Williams, Elisa Londero, Adam Gali, and Christoph Becher. Strongly inhomogeneous distribution of spectral properties of silicon-vacancy color centers in nanodiamonds. *New Journal of Physics*, 20(11):115002, 2018.

[28] AA Lebedev. Deep level centers in silicon carbide: A review. *Semiconductors*, 33:107–130, 1999.

[29] Stefania Castelletto, BC Johnson, Viktor Ivády, N Stavrias, T Umeda, A Gali, and T Ohshima. A silicon carbide room-temperature single-photon source. *Nature materials*, 13(2):151–156, 2014.

[30] G Ischia, M Cutillo, G Guella, N Bazzanella, M Cazzanelli, M Orlandi, A Miotello, and L Fiori. Hydrothermal carbonization of glucose: Secondary char properties, reaction pathways, and kinetics. *Chemical Engineering Journal*, 449:137827, 2022.

[31] Agata Kaczmarek, Jacek Hoffman, Jerzy Morgiel, Tomasz Mościcki, Leszek Stobiński, Zygmunt Szymański, and Artur Małolepszy. Luminescent carbon dots synthesized by the laser ablation of graphite in polyethylenimine and ethylenediamine. *Materials*, 14(4):729, 2021.

[32] Kierstin Daviau and Kanani KM Lee. High-pressure, high-temperature behavior of silicon carbide: A review. *Crystals*, 8(5):217, 2018.

[33] TS Perova, J Wasyluk, SA Kukushkin, AV Osipov, NA Feoktistov, and SA Grudinkin. Micro-raman mapping of 3c-sic thin films grown by solid–gas phase epitaxy on si (111). *Nanoscale research letters*, 5:1507–1511, 2010.

[34] J Wagner, M Ramsteiner, Ch Wild, and P Koidl. Resonant raman scattering of amorphous carbon and polycrystalline diamond films. *Physical Review B*, 40(3):1817, 1989.

[35] E Perevedentseva, A Karmenyan, P-H Chung, and C-L Cheng. Surface-enhanced raman spectroscopy of nanodiamond particles on silver. *Journal of Vacuum Science & Technology B: Microelectronics and Nanometer Structures Processing, Measurement, and Phenomena*, 23(5):1980–1983, 2005.

[36] AV Karmenyan, E Perevedentseva, M Veres, and C-L Cheng. Simultaneous photoluminescence and sers observation of nanodiamond at laser deposition on noble metals. *Plasmonics*, 8:325–333, 2013.

[37] Dana Cialla, Uwe Hübner, Henrik Schneidewind, Robert Möller, and Jürgen Popp. Probing innovative microfabricated substrates for their reproducible sers activity. *ChemPhysChem*, 9(5):758–762, 2008.

[38] Luca Basso, Nicola Bazzanella, Massimo Cazzanelli, and Antonio Miotello. On the route towards a facile fluorescent nanodiamonds laser-synthesis. *Carbon*, 153:148–155, 2019.

[39] Kien-Wen Sun, JY Wang, and TY Ko. Raman spectroscopy of single nanodiamond: Phonon-confinement effects. *Applied Physics Letters*, 92(15), 2008.

Chapter 6

Potential Refinement of the PLAL Technique and Future Perspectives

In the previous chapters I showed the results obtained from the main synthesis and characterisation procedures for SiV fluorescent NDs.

Some other procedures were hinted as possible solutions to some of the problems encountered during the experimental procedures.

In this last chapter I will discuss briefly the issue of separation of the different components of the nanopowders (diamond and silicon carbide phases), the preparation of alternative precursors and the investigation of an alternative synthesis technique for nanodiamonds by photoelectric absorption.

Most of the work covered here is in an initial or unfinished state due to the loss of the excimer laser at the beginning of the third year of my PhD, which made it impossible to test the new precursors or to produce more of the old material to test new procedures.

This means that the additional procedures were performed on just a small amount of the ND-SiC composite powders, after most of the available material had been used in all the other experiments of chapter 5.

6.1 Nanodiamond-NanoSiC Phase Separation

In chapter 5 I showed the morphology of the material produced by PLAL from graphite-SiC composite precursors. Discussing the resulting material shown

in figures 5.5 and 5.6 I highlighted the problems given by agglomeration and the combined contribution of diamond and silicon carbide.

A first step in the separation was isolating the nano scale components by removing the largest fragments of SiC, present in all the samples, even the two most promising low Si concentration samples.

According to Stokes' law, the stability of a colloidal suspension is directly influenced by the size of the particles in suspension as is the velocity of a suspended particle falling under gravity. Therefore it was decided to remove the largest particles from the dispersions by decanting them after estimating the necessary time of deposition.

The samples in dispersion were agitated and subjected to vigorous sonication for $\sim 1h$ in order to achieve homogeneous dispersion, then they were left at rest for $1h$, a time sufficient only for the deposition of the larger ($> 1\mu m$) pieces. The supernatant liquid containing most of the material was then moved to a different vial.

This was enough to remove the largest fragments as expected but the smaller particulate of diamond and SiC, exhibiting similar dimensions and density, are both still in suspension.

The second step was borrowed from separation techniques used for the analysis of meteoric rocks. When one wants to analyse gasses trapped in the various components of the meteorites the procedure consists in selectively break down different components and measure the composition of vapours/gasses. Some carbon rich meteorites contain both nanodiamonds and nanoparticles of SiC, which usually remain as the last two solid fractions. An ammonia solution, which selectively increases the stability of the nanodiamond dispersion, is used to separate the two phases[1, 2].

This technique was adapted by taking the lowest concentration sample 100:1, which also showed the largest contribution of nanodiamond, and dispersing all the remaining powder in a 0.1M ammonia solution and subjecting the dispersion to vigorous ultrasound treatment (hielscher UP400S ultrasonic processor, 50% cycle, 60% amplitude), after that the suspension was left at rest for $\sim 12h$ and again the supernatant was separated into a different vial. The solvent was left to evaporate slowly overnight under a fume hood to remove any ammonia and the powders redispersed in ethanol.

The new dispersion was then deposited on a silver substrate to be analysed. Again diamond contribution was shown by SERS measurements and the SEM images show a rather uniform distribution of carbon particles on the silver as shown in figure 6.1.

While the process appears to effectively select the ND phase, no photo-luminescence contributions were observed.
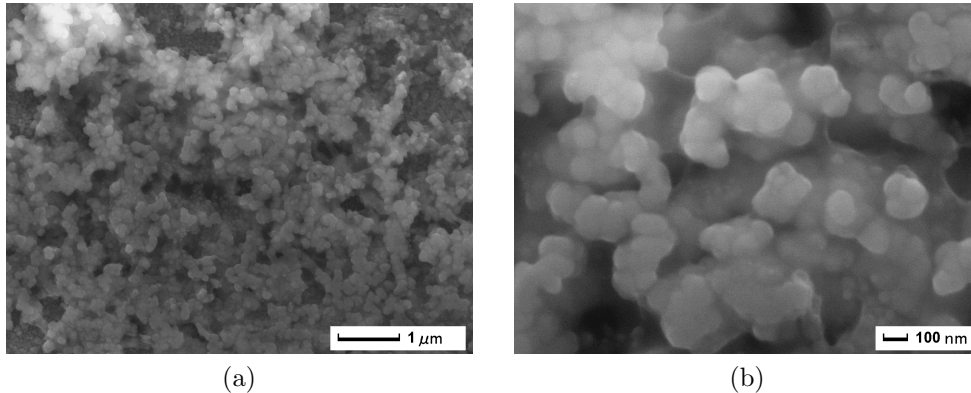

Figure 6.1: SEM micrographs of the ammonia separated fraction from sample 1%

Observing fig. 6.1 we see that the nanoparticles appear still in large conglomerates. Some remaining SiC and isolated graphite sheets appear also in this last sample, yet the procedure can be considered successful.

A possible technique for breaking apart the single conglomerates has been identified in the so called Salt Assisted Ultrasonic Deagglomeration (SAUD)[3, 4]. Here the nanoparticles are dispersed in a supersaturated aqueous slurry of NaCl and subjected to vigorous ultrasound treatment. The salt crystals then work as a milling agent for the conglomerates, while being easily removed by washing analogously to those employed in the post processing chemical purification procedure described in chapter 4. The technique was tried for different applications on carbon black nanoparticles, but the low amount of remaining nanodiamonds made it impossible to work on the ND dispersion.

6.2 Precursors from Sub-Micrometer Carbon Spheres

Another avenue that was explored was the production of precursors using nanomaterials as the initial components.

In literature one can fine different examples of production of graphitic rods from the sintering of carbon mesospheres, generally found in heavy hydrocarbons. A possible alternative to such components is given by carbon micro spheres produced by hydrothermal carbonization (HTC) of glucose[5]. These powders were produced in the department of environmental engineering (DICAM) of the University of Trento.
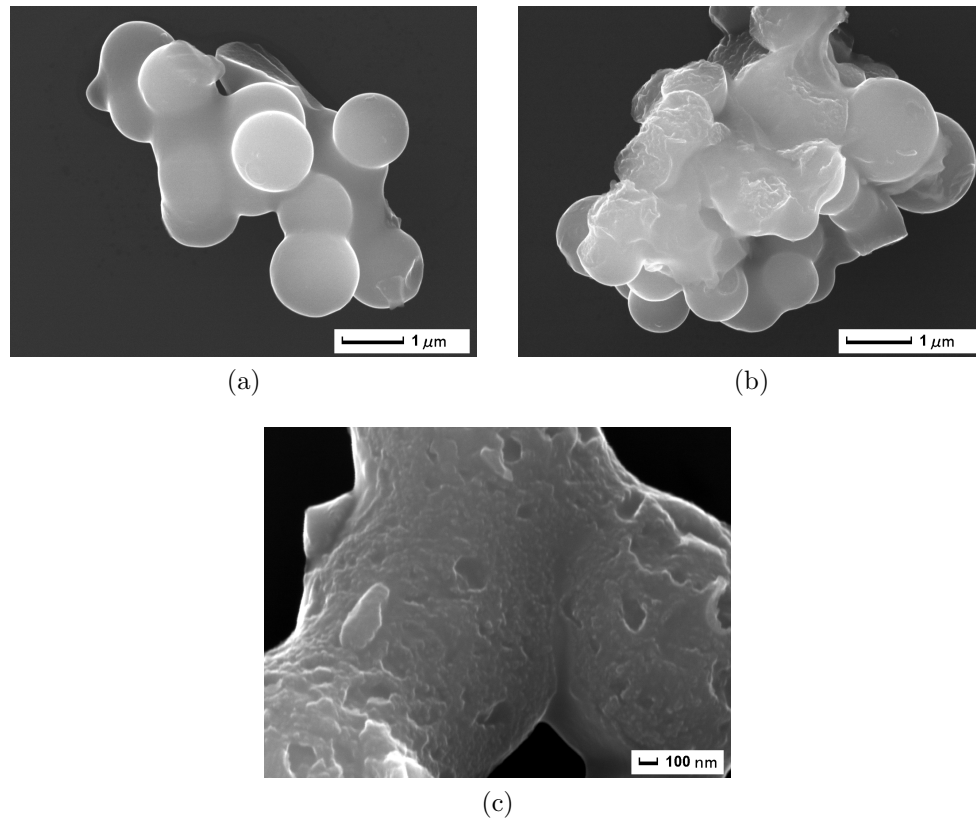

(a)

(b)

(c)

Figure 6.2: SEM micrographs of the particulate recovered from the ablation of the sintered HTC microspheres.

The project was two-fold:

- Producing a pure graphite precursor from the HTC microspheres and subsequently prepare another by sintering the microspheres together with silicon/silica nanoparticles.

- Using HTC to produce particles with already the desired proportion of Si to be used in the precursor preparation.

As written in Chapter 5, this preparation procedure for the precursors, using nanomaterials, would allow to produce precursors with a much more uniform microscopic structure, which in turn gives finer control of the concentration of Si at the nanoscale, without the presence of extreme gradients over a scale of the micrometer.

Under EDXS observation the microsphere appear to contain a large concentration of oxygen, therefore for the first step it was decided to produce a preliminary pellet without the addition of silicon to see if the oxygen could hinder sinterisation.

The powders were pressed in a steel die for 20 minutes under $\sim 120 MPa$ of pressure. The green pellet was the pyrolysed in an oven at $1100°C$ for 5 h under nitrogen flux.

The resulting pellet appears brittle but strong enough to survive PLAL, this test run was the last PLAL experiment that could be performed.

The raw powder obtained by PLAL shows that the particles have fused together during the sintering process, as shown in figure 6.2

In panels (a,b) one can see well fused together particles with clear edges where the particles fragmented during ablation. Panel (c) is a detail of one of the edges corresponding to broken spheres.

Since the available furnace could not reach temperatures employed in the production of the precursors described in Chapter 5, other procedures were taken into account, in particular ultrafast high-temperature sintering (UHS) as described by Wang et al. in [6].

6.3 NDs from UV-C photoelectric absorption

The HTC microsphere were employed again as possible precursors for the production of nanodiamonds by photoelectric absorption.

It has been observed by Gómez de Castro et al. in [7] that UV irradiation can induce the growth of nanodiamonds on graphite. In their work they suggest that the transition between graphite and diamond is caused by the removal of electrons by photoelectric absorption of UV photons. The UV photons with wavelength $< 281nm$ can remove electrons form the bonding π orbitals, creating instabilities in the crystalline lattice of graphite. The electrons removed from the first layers of the graphite by UV photon absorption

have enough energy to move to the inter-layer band, promoting the formation of bonds outside the graphene planes.

The main driver of this experiment was to reproduce the experimental results of [7] using a starting nanoscale substrate.

For this procedure two diluted dispersions were prepared, one with the HTC microspheres and one with carbon black nanoparticles.

The dispersion were deposited on one of the remaining silver substrates and left to dry. The dried dispersions were then put inside a custom built vacuum chamber were they were subjected to UV-C irradiation using two OSRAM OSLON® UV 6060 SU CZHEF1.VC AlGaN LEDs, with peak emission at $\lambda = 260nm$. The choice of the LEDs was driven by the possibility of avoiding the absorption of UV photons by the forming diamond phase. Due to the low radiant flux of the UV source the experiments were performed on time scales of several days.

A first run performed for 5 days of continuous operation showed no modification to the material. A second run was performed over ~ 30 of operation.

Here the carbon black particles appeared to be unmodified, while the HTC microspheres showed evident surface modification.

In figure two representative SEM micrographs of the modified particles over the silver substrate.

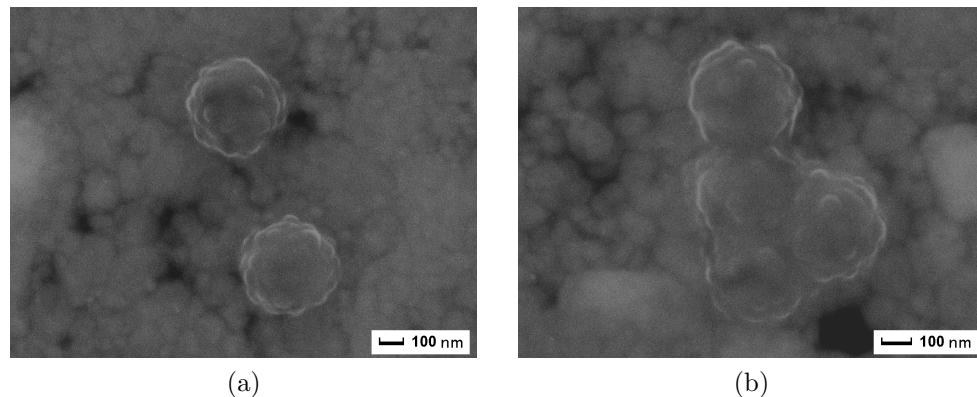(a)   (b)

Figure 6.3: SEM micrographs of the UV-modified HTC carbon nanospheres.

The surface of the particles appears significantly modified with bumps in the order of the tens of nanometers.

Raman observations of the modified samples did not show the presence of the diamond peak. This could be related to the extremely low amount

of material present on the substrate or the formation of different structures, possibly due to the large oxygen content of the particles.

A more powerful UV source could be employed to make this experiments much shorter, allowing for the preparation of larger quantities of material, making characterisation much more reliable.

6.4 Final Remarks

The experiments showed in this last chapter are all potential ways to expand the research in the field of fluorescent ND synthesis.

The separation technique described in the first section, is dependent on the functionalisation of the surface of the nanodiamonds.

This could also be used for separation of differently functionalised nanodiamonds in more refined procedures.

The precursor production experimented in the second section is probably the most promising possibility for future studies. The use of nanomaterials can give fine control on the composition of the precursors, moreover the preparation of the nanopowders by HTC could in principle allow to introduce the desired dopants directly into the micro spheres or equivalent nano/micro structures by addition of adequate substances in the HTC mixture.

This opens also the possibility of using organic material from biological sources (for example a possible silicon source could be rice husk ash, a waste byproduct of rice [8]) as an initial HTC material/additive, adding value to the procedure as a much greener alternative to other techniques with potential for waste valorisation.

Lastly, while not being directly related to the PLAL technique, the production of nanodiamonds by UVC irradiation is still an interesting avenue of research, potentially allowing to fine tune the geometry of the desired structures before the .

Bibliography

[1] Gary R Huss and Roy S Lewis. Presolar diamond, sic, and graphite in primitive chondrites: Abundances as a function of meteorite class and petrologic type. *Geochimica et Cosmochimica Acta*, 59(1):115–160, 1995.

[2] Gary R Huss, Alex P Meshik, Julie B Smith, and CM Hohenberg. Presolar diamond, silicon carbide, and graphite in carbonaceous chondrites: Implications for thermal processing in the solar nebula. *Geochimica et Cosmochimica Acta*, 67(24):4823–4848, 2003.

[3] Stepan Stehlik, Jiri Henych, Pavla Stenclova, Robert Kral, Petra Zemenova, Jiri Pangrac, Ondrej Vanek, Alexander Kromka, and Bohuslav Rezek. Size and nitrogen inhomogeneity in detonation and laser synthesized primary nanodiamond particles revealed via salt-assisted deaggregation. *Carbon*, 171:230–239, 2021.

[4] Kostiantyn Turcheniuk, C Trecazzi, C Deeleepojananan, and VN Mochalin. Salt-assisted ultrasonic deaggregation of nanodiamond. *ACS applied materials & interfaces*, 8(38):25461–25468, 2016.

[5] G Ischia, M Cutillo, G Guella, N Bazzanella, M Cazzanelli, M Orlandi, A Miotello, and L Fiori. Hydrothermal carbonization of glucose: Secondary char properties, reaction pathways, and kinetics. *Chemical Engineering Journal*, 449:137827, 2022.

[6] Chengwei Wang, Weiwei Ping, Qiang Bai, Huachen Cui, Ryan Hensleigh, Ruiliu Wang, Alexandra H Brozena, Zhenpeng Xu, Jiaqi Dai, Yong Pei, et al. A general method to synthesize and sinter bulk ceramics in seconds. *Science*, 368(6490):521–526, 2020.

[7] Ana I Gómez de Castro, Maikel Rheinstädter, Patrick Clancy, Maribel Castilla, Federico de Isidro, Juan I Larruquert, Tomas de Lis-Sánchez, James Britten, Mariona Cabero Piris, and Federico P de Isidro-Gómez. Graphite to diamond transition induced by photoelectric absorption of ultraviolet photons. *Scientific Reports*, 11(1):2492, 2021.

[8] D Kalderis, MS Kotti, A Méndez, and G Gascó. Characterization of hydrochars produced by hydrothermal carbonization of rice husk. *Solid Earth*, 5(1):477–483, 2014.

Conclusions

This thesis presents an extensive exploration of the production of fluorescent nanodiamonds through Pulsed Laser Ablation in Liquid (PLAL). The experimental results showcase its versatility in generating diverse color centers within diamond nanoparticles through a single-step procedure.

Chapter 1 shows a general overview of the properties of nanodiamonds starting with a brief discussion of the bulk phase properties, followed by the properties of the nanoparticles, with particular focus on the optical properties and the different possible color centers of diamond. The Chapter is then closed with a brief review of the possible applications of these nanodiamonds and the relevant techniques employed for their synthesis. These applications, particularly for the quantum sensing field, are the main driver for the work of this PhD project.

A theoretical overview of the processes involved in the formation of nanodiamonds by PLAL is provided in Chapter 2. This more thorough description of the process starts with a description of the energy deposition mechanism in the laser processing of materials, with focus on the materials employed and the relevant timescales of the processes carried out during the experimental works. A description of the Phase Explosion process and of the effects of confinement given by the liquid environment allow to describe the thermodynamics of the formation of nanodiamonds in the conditions obtained during ablation.

The last theoretical chapter covers the properties of the two color centers studied in this work: the nitrogen vacancy center and the silicon vacancy center. Chapter 3 covers the properties of the two centers starting with the structural configurations of these impurities, which are then related to the optical and electronic properties of the centers. Particular care is dedicated to the description of the Hamiltonians of both centers, in particular to the terms related to the effect of quantities like the temperature of the system or

interactions with external fields (e.g. electric or magnetic fields) as these represent the main features that allow the use of the fluorescent nanodiamonds as quantum probes in quantum sensing experiments.

Chapter 4 describes the results obtained for the ablation of graphite in liquid nitrogen. The apparatus constructed for the procedure allows the production of relatively large quantities of material, which allow for the application of scalable and dependable purification techniques. The optical characteristics of the produced nanoparticles are assessed, confirming the typical behaviour of NV centers of diamond.

In Chapter 5 I show the results of an extensive work on the production of fluorescent nanodiamonds containing silicon vacancy centers produced from composite graphite-ceramic precursors. Here the ceramic component is silicon carbide, which is the source of silicon for the production of the fluorescent centers. Morphological and compositional characterisation of the nanopowders allowed to define the different structures formed in the samples at varying concentrations of silicon in the original precursor. The optical characterisation of the powders focuses on the emission in the SiV related region of the spectrum and allows to define an ideal concentration of silicon in the precursor for the formation of fluorescent nanodiamonds. This result is also confronted with literature values for chemical vapour deposition techniques which are more established for the production of this kind of fluorescent nanodiamonds. An unpredicted result was the discovery of photoluminescence from SiC nanoparticles, suggesting an ideal concentration for the formation of defective silicon carbide nanoparticles with potential for quantum optical applications provided refinement of the technique.

Lastly Chapter 6 contains a brief overview of possible next steps that can be applied to further the research in the synthesis of SiV bearing nanodiamonds both in terms of experimentation with different precursors and the development of a more complete post-processing technique allowing for the production of materials of higher purity.

Experimental results of the works shown in this thesis show the versatility of the PLAL technique while being an easily scalable, low cost alternative to more established techniques.

The work on the silicon vacancy center shows that the chosen precursors for the experiments drastically influence the resulting material, with the possibility of producing different color centers and potentially more complex

structures.

This can in principle be applied for all the group IV color centers of diamond, which are an interesting field of research in which to expand experimentation.

Another relevant future perspective is the use of carbon rich precursors derived by the carbonisation of organic materials like the ones briefly observed in Chapter 6.